ESTIMATING AND MODELLING THE COMPOSITIONS OF CRYSTALLIZING TRIACYLGLYCEROL BINARY MIXTURES USING X-RAY DIFFRACTION

by

Pavan Karthik Batchu

Submitted in partial fulfilment of the requirements
for the degree of Master of Science

at

Dalhousie University
Halifax, Nova Scotia
August 2014

I dedicate this Thesis to my late dear mother Mrs. Lakshmi Kumari Batchu of whom her limitless support, love, care and inspiration made me the person I am.

TABLE OF CONTENTS

LIST OF TABLES

LIST OF FIGURES

ABSTRACT

It is necessary to predict the composition, polymorphic form and distribution of the crystalline phases formed from a liquid mixture of fats at any temperature as these attributes affect the physical properties of fat based foods like melting point, spreadability etc. This study aims at testing the linear kinetic segregation (LKS) model (Los and Flöter, 1999) to predict experimental phase behaviour. Time resolved small and wide angle x-ray diffraction (XRD) patterns were obtained from crystallizing binary mixtures of trilaurin and trimyristin at different temperatures. Two β' phases were formed simultaneously in most cases. The composition and amount of these crystalline phases were estimated using an empirical model developed based on XRD measurements. The (LKS) model was partially successful in describing the formation of one of the crystalline phases in all experiments but failed at describing the simultaneous formation of both crystalline phases, thereby highlighting a need for improved models.

LIST OF ABBREVIATIONS AND SYMBOLS USED

BCF	Burton Cabrera and Frank theory
Cryo-TEM	cryogenic transmission electron microscopy
DCL	double chain length structure
FAME	fatty acid methyl esters
FWHM	full width at half maximum
GC	gas chromatography
GUI	graphical user interface
keV	Kiloelectronvolt
LKS	linear kinetic segregation model
LLL	trilaurin
MMM	trimyristin
NSLS	National Synchrotron Light Source
PID	proportional, integral and derivative control
SAXD	small angle x-ray diffraction
TAG	triacylglycerol
TCL	triple chain length structure
WAXD	wide angle x-ray diffraction
XRD	x-ray diffraction
XAS	x-ray absorption spectroscopy
XANES	x-ray absorption near edge structure
A_j	diffraction/scatter area of a phase *j*
d	distance between two layers in a crystal (d-spacing) (nm)
$K_{i,j}$	thermal factor of component i in crystalline phase j to describe equilibrium
k, n	Avrami constant and exponent.
q	scattering vector ($Å^{-1}$)
R	universal gas constant, (J/(K·mol))
S_j	mass fraction of crystalline phase j
SF_t	solid fraction of the crystallizing system at any time t
SF_{max}	maximum solid fraction of the system that could be crystallized

$\overline{T}$	average melting points of trilaurin and trimyristin in the polymorphic form of interest (K)
T	temperature of crystallization (K)
$x_{j,t,inst}$	instantaneous composition of solid material deposited on an existing crystal at any point of time
z	Average composition of trilaurin in the whole system
ΔG	change in Gibbs energy (J)
ΔH	enthalpy change in a crystalline system at a constant temperature and pressure (J)
ΔS	entropy change at a constant pressure and temperature (J/K)
$\gamma_{i,j}$	Activity coefficient of component *i* in crystalline phase *j* for a particular polymorph
σ_i	Area fraction of i^{th} phase in the system
μ_i^l	chemical potential of component *i* in liquid (J/mol)
μ_i^{sj}	chemical potential of component *i* in j^{th} solid phase (J/mol)
ϕ_{ij}	excess energy interaction parameter between components i and j
θ	incident angle of x-rays
ε	kinetic separation parameter
$\kappa_{LM,0}$	kinetic constants ratio of trilaurin with trimyristin
μ	mean value or expected value
$x_{L,j}$	mole fraction of trilaurin in the crystalline phase j
ψ_j	proportionality factor between the normalized area of a crystalline phase j and its mass
ξ	thickness of crystal domain (nm)
λ	wavelength of x-rays (Å)
3L7M	30% trilaurin- 70% trimyristin by weight
5L5M	50% trilaurin- 50% trimyristin by weight
7L3M	70% trilaurin- 30% trimyristin by weight

ACKNOWLEDGEMENTS

First of all, I would like to sincerely thank Dr. Gianfranco Mazzanti whom I always look up to for not only being my supervisor, but for also being my mentor who taught me many things beyond science. For the trust and support he has put into me through these years and for the impact he has created on me; this Thesis would have been impossible otherwise. To my examination committee members Dr. Allan Paulson and Dr. Andrew MacIntosh for their inputs and taking time in reading my Thesis and conducting my oral defence. To Dr. Peter Wentzell for his excellent teachings and inputs regarding statistical work related to the development of models involved in this Thesis. To Dr. Suzanne Budge to let me use her lab space and also gas chromatography equipment to test the purity of samples used for experimentation in this Thesis, also to Anne, Carrie and Chris in the marine lipids laboratory for running my samples in GC and their assistance in the analysis during various occasions.

To my colleagues in the Mazzanti research group, particularly Amro Alkhudair, Omar Alqatami, Pranav Arora, Mohit Kalaria and Rong Liu for their continuous support and discussions, sharing thoughts and ideas and for being there whenever I needed them to share happiness, sadness and joy. To the previous members of the group Mengyu Li and Mette Regitze Von Barner for their help in XRD data analysis and contribution to the development of empirical model presented in this Thesis. To Emmanuel Anom whose work acted as a great precursor for this Thesis.

I would like to thank Dr. Chris Watts and Mrs. Marny Watts for their care and continuous support during hard times. To my friends here and in India, Sandeep, Veer, Praneeth, Mythili, Vijay, Chaitanya, Prasad and Ravi for being there whenever I needed them. To my aunt and uncle, Mr. and Mrs. Prasad Nuli, my cousins Bhaskar and Sravan for their trust and encouragement during hard times.

To my father; Mr. Raja Prasad Batchu who is always there for me and always pushed himself beyond his capabilities for me. For the priceless teachings and values he imparts on me and for being that person who has always stood by me whatever the circumstances may be.

Finally I would like to thank the Faculty of Graduate Studies (FGS) for the scholarship, and to Natural Sciences and Engineering Research Council of Canada (NSERC) for funding this work.

Chapter 1 INTRODUCTION

Fat based foods have a long history of thousands of years being served as delicacies. Evidence of cocoa based drinks in Aztec culture exists dating back to 1900 BC (PadIey, 1997). The most important fat based foods by value are chocolate, ice-cream, vegetable oils, margarines, baking shortenings, and butter. Apart from market value fats are the most concentrated caloric source in nature (Marangoni & Wesdorp, 2012). Yet to date we cannot quantitatively model the behavior of these fat based foods under different conditions.

Triacylglycerols (TAG) make up to 95 percent of consumed fats, yet so far no research is successful in answering a rather simple question, "is it possible to predict the composition and amount of the crystalline phase(s) that will be formed from a liquid binary mixture of TAGs when it is cooled down to a particular temperature?" Understanding thermodynamic equilibrium (or a metastable equilibrium state as in the case of this Thesis) would help in understanding the general tendency for the formation of a crystalline phase if TAGs have regular behaviour. Several theoretical methods to predict their crystallization behaviour have been proposed, exploring different combinations of solid phases with different compositions and minimizing Gibbs energy (Wesdorp, 1990). But due to their medium size, TAGs do not crystallize when they reach an equilibrium condition but need a high degree of undercooling.

TAG molecules are esters of fatty acids with a glycerol backbone, as shown in Figure 1-1. Common minor components present in fats are phospholipids as well as mono and di-glycerides.

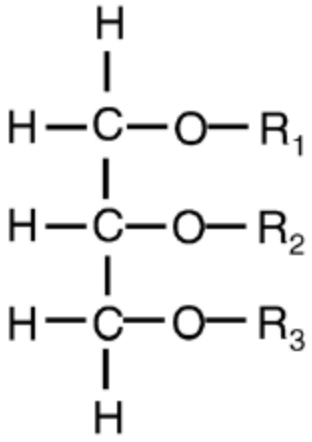

Figure 1-1. A simple representation of a TAG molecule showing the glycerol backbone, R_1, R_2 and R_3 are individual fatty acid moieties (Himawan et al., 2006). (Permission has been obtained from Elsevier scientific publishing co.,)

Fats can form multiple crystalline phases with different compositions when their liquid is cooled down. The composition, proportion and polymorphic form (internal arrangement of molecules) of the crystalline phases depends on the composition of the initial liquid, temperature of crystallization, cooling rate, agitation and many more factors. The formation of these phases is also affected by intrinsic properties of each component.

Many sensory attributes of foods depend on the properties of a crystal network of solid fats (Marangoni & Hartel, 1998; Mazzanti et al., 2004a; Narine & Marangoni, 1999).

As an initial step towards the understanding a multi-component system, a two component system is studied in this Thesis.

The linear kinetic segregation (LKS) model is a theoretical construct that predicts the composition of the solid phase that will crystallize out of a liquid of a known composition and at a particular temperature, away from equilibrium (Los & Flöter, 1999). This model states that the composition a solid phase(s) that is formed at a temperature below the equilibrium is controlled by the relative supersaturation of each component present in the system. This is the best theoretical model available so far to predict the

solid phase composition, yet, no experimental evidence exists so far to verify this model. The main aim of this Thesis is to investigate if this theoretical model describes correctly crystallization in an undercooled TAG binary system.

There is no experimental way to measure directly the solid phase composition(s) and solid phase fraction(s) of crystalline TAGs. However, x-ray diffraction (XRD) of the crystallizing mixtures offers an indirect way to estimate these parameters. This study presents a method developed to estimate the composition(s) and phase fraction(s) from XRD data.

The formation and distribution of crystalline phases is of great importance in many other fields like materials science, metallurgy, mineralogy, geology and deep marine sciences. It is very important to understand the effect of temperature and the composition of liquid on the formation of crystalline phases, domains, and their composition etc., all the physical properties like the strength, malleability, conductivity and many more depend on the above mentioned factors.

In the field of mineralogy crystallization is understood to explain the formation of different rocks and sediments from the same magma. This understanding is further applied to understand the occurrence and to predict the presence of different minerals.

Techniques like x-ray absorption spectroscopy (XAS) and its types like x-ray absorption near edge structure (XANES) etc., which exploit the differences in the electronic configuration of various elements (Bunker, 2010) are used to efficiently calculate the composition and distribution of crystalline domains in the case of metals and minerals. Unfortunately this technique of XAS and XANES cannot be used in the case of a TAG system as all the components in the mixture are chemically made up of the same elements(C, H and O), i.e., they have the same electron shell make up.

1.1 Objectives

The main objective of this Thesis is:

1) To compare the measured isothermal crystallization history of binary mixtures of TAGs with the predictions of the linear kinetic segregation (LKS) model.

In order to compare the experimental crystallization with theoretical predictions, an experimental method to measure the composition and amount of crystalline phases needs to be developed. Thus, the second objective is:

2) To improve the understanding of the crystallization of TAG binary mixtures by providing a method to estimate the phase composition and distribution.

The main research questions are:

- For a phase with a given d-spacing, can the composition be estimated?
- For a phase with a given area fraction and composition, can the mass fraction be calculated?
- Can the correlation developed between d-spacing and composition, area fraction and mass fraction of a phase be used to follow the crystallization procedure to calculate the amount of crystalline phase being formed at a particular time t?
- For a given binary mixture of known composition z crystallized isothermally at a temperature T, can the composition and mass fraction, polymorphic form of the phases formed be predicted using the LKS model?
- Do the theoretical predictions from the LKS model agree with the actual experimental results?

Chapter 2 LITERATURE REVIEW

Lipids are defined as "fatty acids and their derivatives, and molecules that are related biosynthetically or functionally to these compounds"(Christie, 2010).

At the macroscopic level Fats are comprised of a hierarchical arrangement with different levels of organization. The organization of fat molecules at different levels is affected by the processing conditions which impacts the physical properties of fat based foods (Marangoni & Wesdorp, 2012). The different levels that lead to the formation of macroscopic fats are shown in figure 2.1.

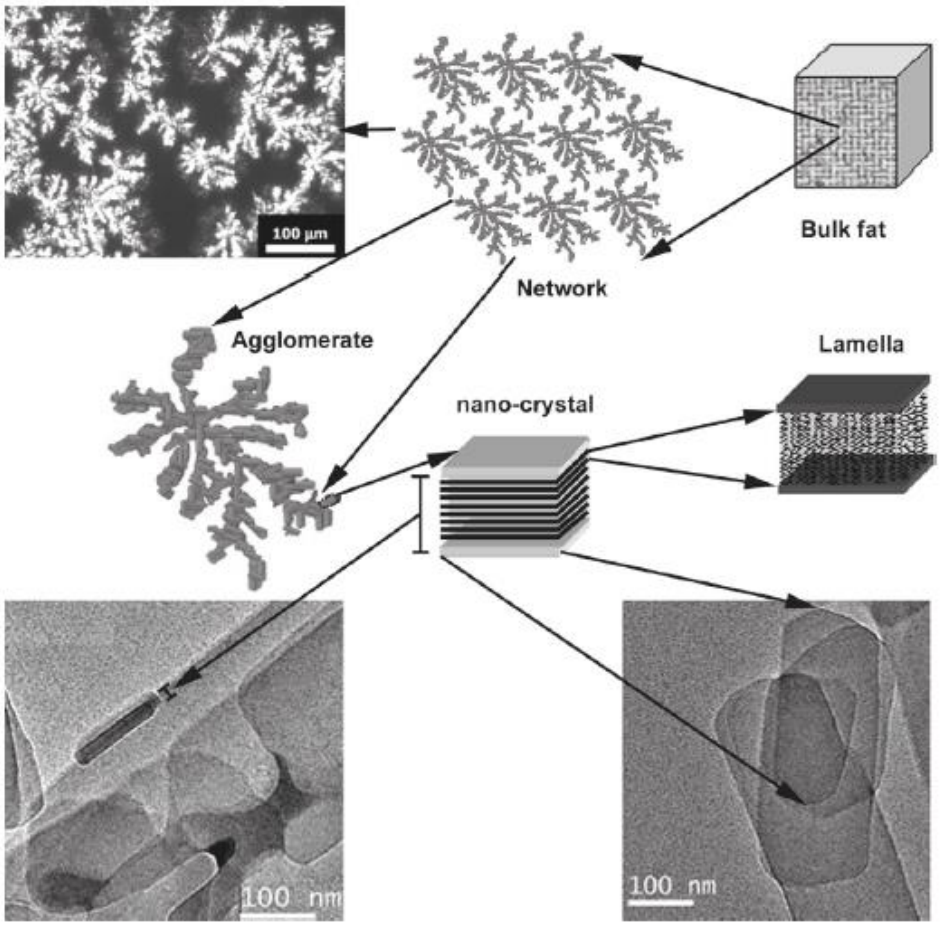

Figure 2-1. The organization of TAG molecules at different levels giving rise to the macroscopic structure of solid fat. Adapted with permission from (Acevedo & Marangoni, 2010). Copyright (2010) American Chemical society.

2.1 Crystallization

Crystallization involves the formation and growth of a solid phase, with a single order of molecules, from a supersaturated liquid. The arrangement of molecules in which the TAGs crystallize greatly affects the physical properties of foods in terms of melting point, elasticity, texture and other properties (Marangoni & Wesdorp, 2012).

2.1.1 Nucleation

Nuclei are the smallest stable crystals that form when a liquid is supersaturated. A solution is supersaturated when the activity (These terms 'activity' and 'supersaturation' were better explained in detail in the latter sections of this Thesis) of a component is higher than its activity in a saturated solution (Kloek et al., 2000). For TAGs, a nucleus starts to form at measurable rates when the temperature of the melt is 5-10 °C below the melting point of a component (Marangoni & Wesdorp, 2012). The degree of undercooling for a component in the melt is the difference between the saturation temperature and the actual temperature of the liquid. The higher the degree of undercooling, the higher the tendency to form a nucleus. At lower degrees of undercooling, the nuclei that are formed, called embryos, continuously break due to the bombardment by liquid molecules of higher energy. Only those nuclei which have managed to attain the critical nucleus size (R_c) can then grow into a crystal.

There are two types of nucleation processes, primary nucleation and secondary nucleation (Garside, 1987; Mullin, 2001).

2.1.1.1 Primary nucleation

Primary nucleation is also divided into two sub types: homogeneous nucleation and heterogeneous nucleation (Garside, 1987; Mullin, 2001).

During primary homogeneous nucleation, molecules aggregate until they reach critical size and start to grow. Primary homogeneous nucleation occurs rarely and always requires a high degree of undercooling. Heterogeneous nucleation occurs in the presence of foreign materials like dirt, rough surfaces or kinks in the system. Liquid molecules attach themselves to these surfaces and start growing into a crystal. The presence of these

foreign materials greatly reduces the Gibbs energy of nucleation (Garside, 1987; Mullin, 2001).

2.1.1.2 Secondary nucleation

Secondary nucleation occurs when molecules attach to an existing crystal and start growing as a new crystal. Secondary nucleation is also influenced by many factors like degree of undercooling, impurities in the crystallizing system, size and number of existing crystallites and also the degree of roughness of the existing crystals. In an agitated system, existing clusters of nanoplatelets crack or often break apart, opening new sites for secondary nucleation (Mullin, 2001).

2.1.2 Polymorphism

Polymorphism is the ability of materials to exist in different crystalline forms. Polymorphic forms differ from each other by the arrangement/packing of the molecules in their solid state. Research on pure TAGs has been done to understand the formation and physical properties of different polymorphic forms (Garti & Sato, 1988; Hagemann & Rothfus, 1983; Kellens et al., 1991; Kellens et al., 1990; Kobayashi, 1988; Lutton & Fehl, 1970). For a particular composition of a solid, the physical properties like the melting point and the macroscopic properties such as mechanical strength, greatly depend on the polymorphic form. The major polymorphic forms of TAGs observed are called α, β and β'. Commercially, β is the sought after polymorphic form of cocoa butter (chocolate), β' is required in the processing of margarines whereas α is observed in chilled milk fats (Lopez et al., 2000). The classification of these polymorphic forms is based on the lateral arrangement of molecules or the sub-cellular packing. The hydrocarbon chains of TAG molecules arrange in a zig-zag fashion during crystallization. The sub-cellular packing in the case of TAG crystals represents the arrangement between these zig-zag hydrocarbon chains as shown in Figure 2-2.

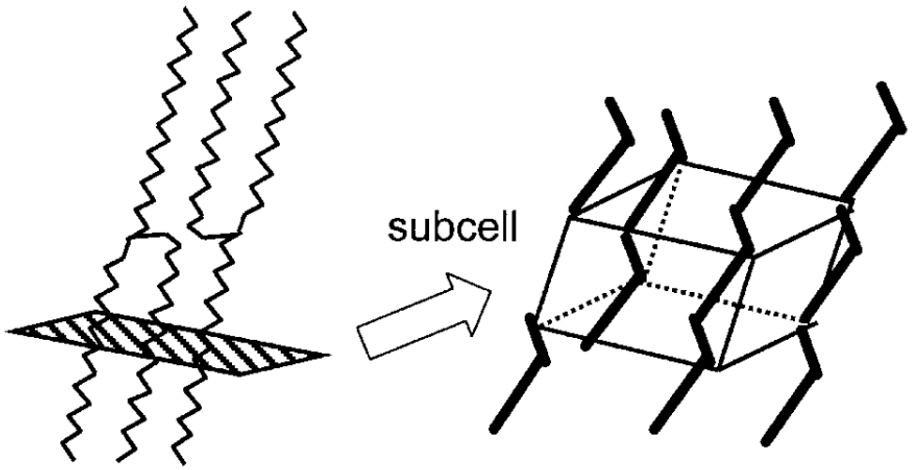

Figure 2-2. Sub-cell structures of TAGs (Bailey, 1964). (Permission has been obtained from John Wiley and Sons)

The polymorphic form α has a hexagonal sub-cell packing, β' has an orthorhombic perpendicular packing, and β has triclinic parallel packing (Hoerr, 1964; Larsson, 1966; Lutton, 1945). A schematic representation of the three sub-cell packings is shown in Figure 2-3.

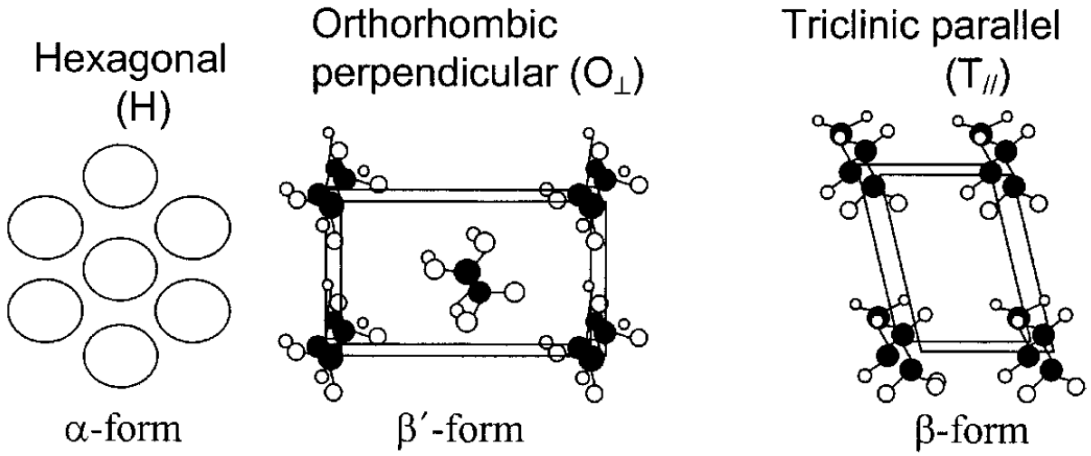

Figure 2-3. The sub-cell packings of the three major polymorphic forms of TAGs. α, β' and β (Bailey, 1964). (Permission has been obtained from John Wiley and Sons)

The sub-cell classification of a polymorphic form gives information about the lateral arrangement or the arrangement of hydrocarbon chains with respect to one another in a crystal. In the longitudinal direction, TAG molecules in a crystal appear to have a 'chair'

conformation. A certain tilt or angle exists between the stacked TAG molecules, particular to each polymorphic form. Different stacking arrangements were observed in the lateral direction in the previous studies conducted (Marangoni & Wesdorp, 2012; Widlak et al., 2001). Double chain lengths (DCL) are the most common arrangement of lamellar packing in the case of TAGs. Triple chain length structures (TCL) were also observed. The occurrence of these structures is due to chain sorting and are confirmed in the single crystal analysis of 1,2-dipalmitoyl-3-acetyl-sn-glycerol in its β form (Goto et al., 1992). The TCL structures have also been observed in one of the β forms of cocoa butter (Mazzanti, 2004; Schenk & Peschar, 2004). Other arrangements like quatro and hexa as shown in Figure 2-4 have been observed in rare circumstances (Widlak et al., 2001).

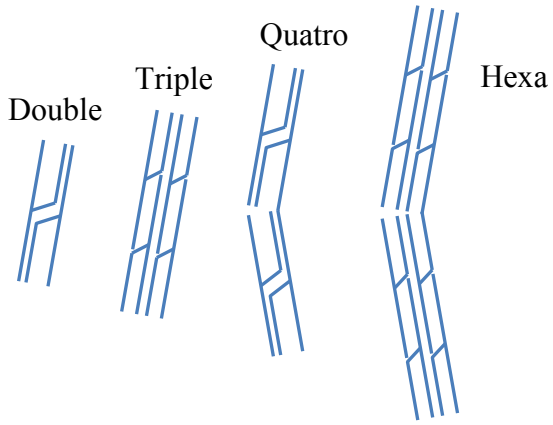

Figure 2-4. Different lamellar packings observed in TAGs

Apart from the three major sub-cell configurations, about 10 different types of sub-cellular arrangements have been reported. In one of the studies conducted on tripalmitin (a TAG made up of glycerol esterified to completely saturated 16 carbon numbered fatty acid chains), sub-polymorphic forms of β' and β have been observed (Kellens et al., 1991; Kellens et al., 1990).

The order of polymorphic forms in terms of increasing melting point, enthalpy, and density is α → β'→ β. The distance between molecules in these polymorphic forms increases in the opposite direction. Higher density of a polymorphic form corresponds to tighter packing of molecules, hence corresponding to better stability and lower Gibbs energy.

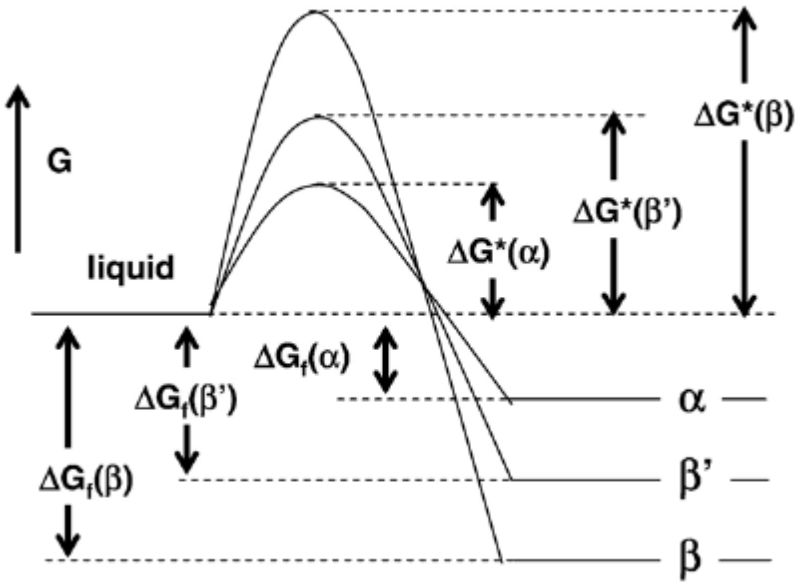

Figure 2-5. A rough sketch showing the differences in the activation energies of formation for the three polymorphic forms (Himawan et al., 2006). $\Delta G^{*}(k)$ and $\Delta G_f(k)$ represent the activation energy and the Gibbs energy of formation of a polymorphic form 'k' from ground state (Permission has been obtained from Elsevier)

Binary mixtures of trilaurin and trimyristin are used in this study. The physical properties of the different polymorphic forms of these TAGs including their melting points, enthalpies of crystallization, are shown in Table 2-1 and Table 2-2.

Table 2-1. The melting point and enthalpy of crystallization of pure trilaurin and pure trimyristin

Triglyceride	Polymorphic form											
	Melting point (˚C)									Heat of fusion (kJ/mol)		
	α			β'			B			α	β'	β
	x	y	z	x	y	z	x	y	z	x	x	x
Trilaurin	14	15.2	15	30, 34, 40	34	35	46	46.5	46.5	72	86	116
Trimyristin	31	32.8	33	54, 56	50.1	47	58	56.2	57	97.1	109	144

[x] (Lutton & Fehl, 1970), [y] (Hagemann & Rothfus, 1983) [z] (Takeuchi et al., 2003)

(Table compiled by Emmanuel Anom)

A comparison of data on short and long spacings of pure trilaurin and trimyristin from studies by (Lutton & Fehl, 1970; Takeuchi et al., 2003) is presented below:

Table 2-2. Short and long spacings of pure trilaurin and pure trimyristin measured using x-ray diffraction of all the three polymorphic forms from two different studies

Triglyceride	Polymorphic form								
	Lamellar distance , LD (nm)						Short spacing SS (nm)		
	α		β'		B		α	β'	β
	x	z	x	Z	x	Z	z	z	z
Trilaurin	3.55	3.5	3.29	3.2	3.12	3.1	0.42	0.42, 0.38	0.46, 0.39, 0.38
Trimyristin	4.03	4.1	3.67	3.7		3.6	0.42	0.42, 0.38	0.46, 0.39, 0.38

[x] (Lutton & Fehl, 1970), [z] (Takeuchi et al., 2003)

(Table compiled by Emmanuel Anom)

The identification of the polymorphic form of a crystalline phase is done by comparing the WAXD spacings with the characteristic spacings shown in Table 2-2.

2.1.2.1 Polymorphic phase transitions

As the polymorphic form β is the most stable (see Figure 2-5), all other forms tend to transform into β over time. These polymorphic transformations have been studied on pure TAGs, TAG mixtures and natural fats like cocoa butter, palm oil, or milk fat, over the years (Garti & Sato, 1988; Kellens et al., 1991; Kellens et al., 1990; Rousset & Rappaz, 1997; Rousset et al., 1998; Sato, 1999; van Malssen et al., 1999).

The Gibbs energy of a state for a particular system gives an estimate of its stability if compared to a standard state. For a process/transformation to be spontaneous, ΔG should be negative. The lower the value of ΔG_f, the more spontaneous a process is. Figure 2-5, shows a comparison of the Gibbs energy of formation of all the three major polymorphic forms. In Figure 2-5 a lower value of ΔG_f also corresponds to a much higher ΔG^*(Gibbs energy barrier of formation). Thus, a higher degree of undercooling (driving force) below the melting point is required to make a more stable polymorphic form like β, while for the formation of a metastable form like α, a lower degree of undercooling would suffice. Therefore, as soon as a melt reaches a temperature below the melting point

of α, the crystallization will be dominated by its formation even though the degree of undercooling is appreciable in terms of the polymorphic form β (Sato, 1999).

Ostwald's step rule describes the formation of a less stable polymorph being formed and eventually transforming into a more stable form. If a less stable form is heated just above its melting point, it readily transforms into a more stable form due to the presence of nuclei that belong to the more stable form. This process is exploited in the tempering of chocolate. The reason that more than one polymorphic form co-exist for a long time at a particular temperature is due to the rate of transformation which is much slower than the rate of crystallization. Steric hindrances play a very important role in slow polymorphic transformations in a completely crystalline system (Sato, 1993).

The mechanisms identified for the phase transitions are, melt mediated transformation and solution mediated transformation.

2.1.2.2 Melt mediated transformation

When the temperature of a system having a less stable or metastable polymorphic form is increased above its melting point, it readily transforms into a more stable form. This transformation could be from α → β' → β or could be directly α → β. This accelerated rate of crystallization/ phase transformation is believed to be due to the presence of many embryos of more stable forms that are formed by solid-state transformation (Sato, 1993). Sato (1993) observed that β formed after an induction time of 6 minutes when a melt was cooled down to 52 °C. The formation of the same polymorphic form took 30 seconds when the system was heated up to the same temperature from a crystallized α form (Sato & Kuroda, 1987). This process of melt mediated transformation is often exploited in many applications like tempering of chocolate to obtain the required polymorphic form more efficiently. A new method to obtain high quality chocolate by adding seed crystals of required polymorphic form was also developed (Schenk & Peschar, 2004) through the understanding of this melt mediated transformation process.

2.1.2.3 Solution mediated transformation

Sato (1993) reports that in solution mediated transformation, the solubility of a particular polymorphic form in a solvent controls the transformation process. Parameters like temperature, type of solvent, crystal size, viscosity of solution, stirring rate, impurities etc., affect this kind of transformation. Two different kinds of regimes are described in this kind of transformation process. The first regime is a dissolution limited region and the second is a growth limiting region. A rapid fall in supersaturation of a component occurs in a growth limiting region while the change in supersaturation is much slower in a dissolution limiting regime (Cisneros et al., 2006; Sato, 1993)

2.1.3 Crystal growth

Once a nucleus reaches critical radius, it starts to grow by incorporating liquid molecules into it. The critical radius depends on the properties of the components present in the liquid and also on the difference between the chemical potential of liquid and solid phase (Marangoni & Wesdorp, 2012). The rate at which the growth of a crystal takes place is simply controlled by the difference in the attachment and detachment flux of molecules. The difference depends on many conditions like temperature, degree of supersaturation, rate of molecular diffusion onto the crystal's surface and also the properties of solid liquid-interface and the structure of the crystal surface (Garside, 1987; Kurz & Fisher, 1986).

2.1.3.1 The mechanism of growth at a molecular level

A theory to explain the formation of a nucleus from a supersaturated vapor/liquid system, growth of a nucleus into a crystal and conditions both thermodynamic and physical effecting the crystal growth etc., was developed by W.K Burton, N. Cabrera and F.C. Frank in 1951 (Burton et al., 1951) often abbreviated as BCF.

One of the main ideas of this theory is that growth takes place by the formation of steps or kinks on the surface of an existing crystal. As described earlier, a crystal is just an ordered stacking of molecules one over the other in a repeatable fashion. The creation of a kink takes place when a single molecule attaches to the surface of a crystal. Creation of steps takes place when molecules continue to attach along these kinks. These steps are

nothing but uncompleted layers on the crystal surface. These kinks reduce the free energy of crystallization causing more molecules to attach. The attachment of molecules leads to the formation of more steps and this phenomenon continues until a complete layer is formed.

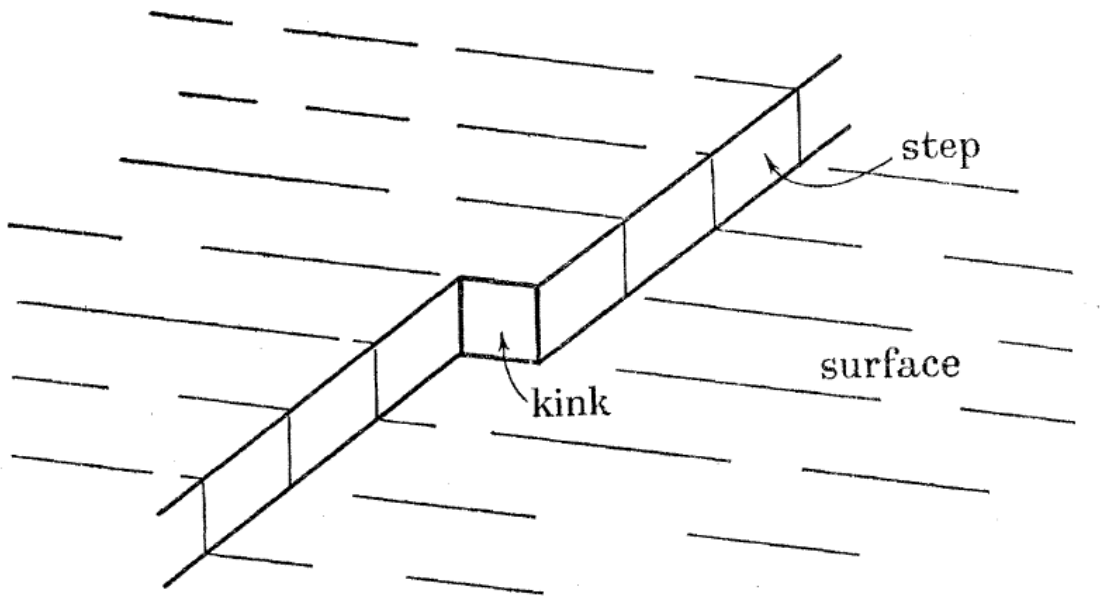

Figure 2-6. Formation of kinks leading to the formation of steps on a crystal surface during the growth of a crystal (Burton et al., 1951). (Permisson has been obtained from the journal "Philosophical Transactions of the Royal Society A – Mathematical, Physical and Engineering Sciences")

BCF theory also states that the formation of these steps takes place only at a higher degree of supersaturation. In a lower degree of supersaturation, which generally is the case in most crystallization processes, the imperfections like dislocations etc., make the attachment sites for crystal growth. In the case of TAGs, there seems to be a limit in the maximum size of a crystallite that can grow at any set of conditions (Acevedo & Marangoni, 2010). For the first time Acevedo and Marangoni (2010) were successful in measuring the dimensions of an individual crystallite using cryogenic transmission electron microscopy (Cryo-TEM). They found that TAG crystals grow as platelets and the dimensions of these platelets vary between 150 × 60 × 30 nm to 370 × 160 × 40 nm depending on conditions of supersaturation.

2.1.3.2 Crystallization from a thermodynamics perspective

Many successful theoretical models like JMAEK (Avrami model) (Avrami, 1939, 1940, 1941; Erofe'ev, 1946; Johnson & Mehl, 1939; Kolmogorov, 1937), Foubert model (Foubert et al., 2002) and $\sqrt{t}$ model (Mazzanti et al., 2008) have been developed to predict the growth rate of solid material from a multi-component TAG system at any set of conditions. The basic functionality of these models is to reliably predict the solid content in a crystallizing TAG mixture at any set of conditions. Solid content curves (SF curves) have been developed through experimentation for many natural fats like cocoa butter (Foubert et al., 2002), milk fat (Foubert et al., 2002; Mazzanti et al., 2008) etc. Growth parameters were obtained by fitting these theoretical models into experimental data. For a particular set of processing conditions (cooling rate, shear rate etc.,) the solid content at any point during crystallization is a direct measure of the bulk physical properties like texture, spreadability, melting point etc.

However, due to their semi-empirical nature, these models can be considered as local models and they are generally confined to a particular system and cannot be generalized to all possible mixtures of TAGs. Thus, a detailed understanding of processes taking place at molecular level relating the properties of single components and their interactions is required to explain the behaviour of a multicomponent blend at bulk level. These interactions could be better understood through the thermodynamics of crystallization (Wesdorp, 1990), adopted from (Marangoni & Wesdorp, 2012).

The first step is to understand equilibrium and then use it to understand the process at non-equilibrium conditions (Los & Flöter, 1999; Los et al., 2002).

Two phases which are in contact with each other are said to be at equilibrium when there is no resultant mass or energy transfer between these two phases. As the minimization of Gibbs energy is the natural driving force for any system, thermodynamically, equilibrium between phases is the point at which the chemical potential with respect to all the components in the phases becomes equal. (See section 2.1.3.2.2).

Crystallization of TAGs often takes place at a very high degree of supersaturation (at conditions below equilibrium) due to the relatively large size of these molecules. As a

result, the composition of a solid phase that will be formed at these conditions skews far from equilibrium concentrations, due to the difference in attachments and detachments of each component at a higher degree of undercooling (Los & Flöter, 1999; Los et al., 2002).

Also due to negligible diffusion in solid state and the fast deposition of solid material from the liquid phase, the formation of a non-homogeneous solid phase easily occurs. Therefore, to study the kinetics of fat crystallization, it is important to estimate the composition and the amount of solid that is being crystallized at any particular instance (Los & Flöter, 1999). The following sections first describe the equilibrium condition between solid and liquid fats and Wesdorp's approach (1990) to model equilibrium followed by the development of the LKS model proposed by Los and Flöter (1999) to explain the phase formation at non-equilibrium conditions.

2.1.3.2.1 Equilibrium and kinetic phase diagrams

A phase diagram predicts the composition of solid phase(s) from a liquid at a particular set of conditions (temperature, pressure). The amount of a particular phase can then be calculated from a phase diagram using a mass balance. These phase diagrams are constructed based on an understanding of thermodynamic equilibrium between a liquid of known composition and its corresponding solid phase(s) (see section 2.1.3.2.2). As the formation of a solid phase occurs at conditions below equilibrium, the composition of a crystalline phase depends on the relative supersaturation of each component in the liquid phase. Phase diagrams used to predict the formation of a crystalline phase at these non-equilibrium conditions that are constructed by considering the kinetic factors on phase formation are called kinetic phase diagrams (see 2.1.3.2.4 for details).

2.1.3.2.2 The equilibrium condition

At equilibrium, the chemical potential of any component in a liquid should be equal to the chemical potential of that component in all solid phases.

$$\mu_i^l = \mu_i^{sj} \tag{2-1}$$

Here, μ_i^l is the chemical potential of component i in liquid

μ_i^{sj} is the chemical potential of component i in j^{th} solid phase.

In the case of a multi component system, the chemical potential of any component *i* in a phase *P* can be expressed as:

$$\mu_i^P = \mu_{i,0}^P + RT\ln(\gamma_i^P \cdot x_i^P) \tag{2-2}$$

Here, μ_i^P is the chemical potential of component *i* in a mixed phase *P*

$\mu_{i,0}^P$ is the chemical potential of component i in a pure phase P for a particular reference state/polymorphic form.

γ_i^P is the activity coefficient of component i in mixed phase P

x_i^P is the mole fraction of component i in phase P

The molar Gibbs energy of formation for phase P made up of two components A and B is given by:

$$g^P = g_{A,0}^P \cdot x_A^P + g_{B,0}^P \cdot x_B^P + g_{m,ideal}^P + g_{m,exc}^P \tag{2-3}$$

Here, $g_{A,0}^P$, $g_{B,0}^P$ are the molar Gibbs energy of pure components A and B,

$g_{m,ideal}^P$, $g_{m,exc}^P$ are the ideal and excess molar Gibbs energies of mixing.

Ideal Gibbs energy of mixing is given by:

$$g_{m,ideal}^P = -RT(x_A^P \cdot \ln(x_A^P) + x_B^P \cdot \ln(x_B^P)) \tag{2-4}$$

The excess energies of mixing can be neglected in the liquid state and in the polymorphic form α. The polymorphic forms β' and β have non-zero excess energies of mixing (Takeuchi et al., 2003; Wesdorp, 1990), Adopted from Marangoni & Wesdorp (2012).

The total Gibbs energy of mixing is related to the molar Gibbs energy of mixing by:

$$G_{m,exc}^S = n \cdot g_{m,exc}^S \tag{2-5}$$

n is the total number of moles of solid phase S. i.e., $n = n_A^S + n_B^S$

The activity coefficient (γ) and the excess Gibbs energy of mixing are related as:

$$RT\ln(\gamma_i^S) = \frac{\partial G_{m,exc}^S}{\partial n_i^S} \tag{2-6}$$

Where n_i^S is the number of moles of component *i* in the solid phase *S* and *i* could be either *A* or *B*

A three-suffix Margules activity model is used to estimate the excess free energy of mixing (Margules, 1895).

$$g^{s}_{m,exc} = \left(\Phi^{exc}_{BA} \cdot x^{s}_{A} + \Phi^{exc}_{AB} \cdot x^{s}_{B}\right) \cdot x^{s}_{A} \cdot x^{s}_{B} \tag{2-7}$$

Here, $\Phi_{BA}{}^{exc}$ and $\Phi_{AB}{}^{exc}$ are the interaction parameters of component B with a pool of pure solid made up of *A* and component *A* with a pool of pure solid made up of *B*. Activity coefficient of component *i* in solid phase s (γ_i^s) is calculated from equation (2-7)

Simplifying equations (2-7) and (2-5) and (2-6)

γ_i^s can be estimated as

$$\gamma^{s}_{i} = \exp\left[(x^{s}_{j})^{2} \left(\frac{\overline{T}}{T} \phi^{exc}_{ij} + 2\frac{\overline{T}}{T}\left(\phi^{exc}_{ji} - \phi^{exc}_{ij}\right) x^{s}_{i} \right) \right] \tag{2-8}$$

Going back to equations (2-1) and (2-2) at equilibrium,

$$\mu^{l}_{i,0} + RT\ln(\gamma^{l}_{i,eq} \cdot x^{l}_{i,eq}) = \mu^{s}_{i,0} + RT\ln(\gamma^{s}_{i} \cdot x^{s}_{i}) \tag{2-9}$$

Rearranging this equation,

$$\ln\left(\frac{\gamma^{sj}_{i} \cdot x^{sj}_{i}}{\gamma^{l}_{i,eq} \cdot x^{l}_{i,eq}}\right) = \frac{\mu^{l}_{i,0} - \mu^{sj}_{i,0}}{RT} \tag{2-10}$$

Equation (2-10) can be developed into:

$$\ln\left(\frac{\gamma^{sj}_{i} x^{sj}_{i}}{\gamma^{l}_{i,eq} x^{l}_{i,eq}}\right) = \frac{\Delta H_{i,o}\Delta T}{RT_{m}T} - \frac{\Delta c_{p,i}\Delta T}{RT} + \frac{\Delta c_{p,i}}{R}\ln\left(\frac{T_{m}}{T}\right) \tag{2-11}$$

Here, T_m and $\Delta H_{i,0}$ are the melting point and melting enthalpy of pure component *i* in the reference state. $\Delta T = T_m - T$, $\Delta c_{p,i}$ is the difference in the specific heats of liquid and solid pure component *i*. In the case of a system having a $\Delta T<10$ K, the contributions from the change in specific heats are very small and they can be neglected. Assuming the mixing in the liquid state is ideal (Wesdorp, 1990), adopted from (Marangoni & Wesdorp, 2012), the value of $\gamma^{l}_{i,eq} \approx 1$. Rearranging equation (2-11) leads to

$$x^{l}_{i,eq} = x^{s}_{i}\gamma^{s}_{i} \exp\left(-\frac{\Delta H_{i,o}\Delta T}{RT_{m}T}\right) \tag{2-12}$$

T is the absolute temperature in K of the crystallizing system. $\overline{T}$ is the average melting point of pure components i and j in the reference state of this study. And ϕ_{ij}^{exc} and ϕ_{ji}^{exc} are the modified interaction parameters of the components I and j. They are defined as:

$$\phi_{ij}^{exc} = \frac{\Phi_{ij}^{exc}}{R\overline{T}} \tag{2-13}$$

If the activity coefficient (γ_i^s) could be determined, the expression above could be used to calculate the composition of a solid phase that would be crystallized out of a liquid at a particular temperature.

2.1.3.2.3 Wesdorp's approach to model solid-liquid equilibrium for fats

Wesdorp's approach puts a lot of emphasis on equilibrium rather than kinetics. Kinetics refers to the formation of a solid phase from a liquid at conditions away from equilibrium where factors like attachments/detachments liquid molecules to the surface of an existing solid and many other factors like the shape/geometry are the major driving force of crystallization. Knowledge of phase equilibrium serves as an initial step in better understanding the crystallization process. Wesdorp attempted to provide a solution for a multi-component system by using the physical properties of each component in its pure form. These properties include melting points and enthalpies of crystallization. Mathematical methods to predict the equilibrium phase behavior of a multi-component system were described. The major idea behind this approach is to propose a reliable method to perform solid-liquid flash calculations by means of simultaneously solving complex sets of non-linear equations to predict the amount and composition of each solid phase crystallizing from a liquid of known composition at a particular temperature. The approach is not presented here in detail as the main emphasis of this study is to understand the effect of kinetics on crystallization.

2.1.3.2.4 Linear kinetic segregation (LKS) model

As described in the beginning of this section (2.1.5.3), knowledge of equilibrium alone is insufficient to estimate the composition of solid phase crystallizing from a liquid.

Due to the very low diffusion in crystalline TAGs, it is safe to assume adsorption and desorption of molecules on the surface play an important role in affecting the composition of the phases at any point during crystallization. The flux of molecules of the component *A* being adsorbed on the crystal surface could be assumed to be directly proportional to the concentration of these molecules in the liquid at the interface.

$$J_A^+ = N_P \cdot \tilde{k}_A^+ \cdot x_A^l \tag{2-14}$$

N_P is the number of sites on the crystal surface where attachment of component *A* could happen. $\tilde{k}_A^+$ is the average attachment probability of molecules of component *A* on the crystal surface. According to the principle of microscopic reversibility (Tolman, 1925), the ratio of the rate of attachment and detachment of molecules on a kinetically or thermally roughened surface is given as:

$$\frac{J_A^+}{J_A^-} = \exp\left(\frac{\Delta\mu_A}{RT}\right) \tag{2-15}$$

Where, $\Delta\mu_A$ is the difference in the chemical potential of component *A* between the bulk liquid and component *A* that is crystallized in solids. This difference in chemical potential can be calculated from (2-2). R_A is defined as the net flux of molecules of component *A* being adsorbed and desorbed over the crystal surface.

$$R_A = J_A^+ - J_A^- \tag{2-16}$$

Using equation (2-15) in (2-16),

$$R_A = N_p \cdot \tilde{k}_A^+ \cdot (x_A^l - x_A^{l,eq}) \tag{2-17}$$

The kinetic composition of the growing solid could be obtained by the ratio of net flux of components '*A*' and '*B*' being attached to the crystal surface.

$$\frac{x_A^S}{x_B^s} = \kappa_{AB} \frac{x_A^l - x_{A,eq}^l}{x_B^l - x_{B,eq}^l} \tag{2-18}$$

This kinetic constants ratio κ_{AB} is defined as

$$\kappa_{AB} = \frac{\widetilde{k}_A^+}{\widetilde{k}_B^+} \tag{2-19}$$

$\widetilde{k}_A^+$ and $\widetilde{k}_B^+$ are the average attachment probability of molecules of component '*A*' and '*B*' to the crystal surface. If these molecules are similar to each other, the average attachment probabilities of both the molecules will be very close to 0.5. This again means that if the excess mixing free energies of both components are small, the kinetic constants ratio $\kappa_{AB} \approx 1$. An additional kinetic separation parameter ε is defined to include the effect of activity of each component on the activation free energies of attachment/detachment of molecules on a crystal surface.

$$\kappa_{AB} = \kappa_{AB,0}\left(\frac{\gamma_B^s}{\gamma_A^s}\right)^{\varepsilon} \tag{2-20}$$

The value of ε is between 0 and 1, a value of 0 indicates the independence of attachment/detachment fluxes from the activity of each component, while a value of 1 indicates the ratio of attachment/detachment of molecules, similar to an ideal case. A starting value of 0.5 can be assumed and can be adjusted as such. Equation (2-18) could be used to construct kinetic phase diagrams to predict the phase composition of a solid crystallizing out of a liquid at a given set of conditions if reliable values of the parameters like interaction parameters, kinetic constant ratio etc., could be established. Thus, an effective phase diagram that can describe the formation of crystalline phase(s) at the conditions of supersaturation is essentially a distorted equilibrium diagram. For a binary system, continuous solid and eutectic phase diagrams are the most common. A general appearance of these diagrams are shown in Figure 2-7.

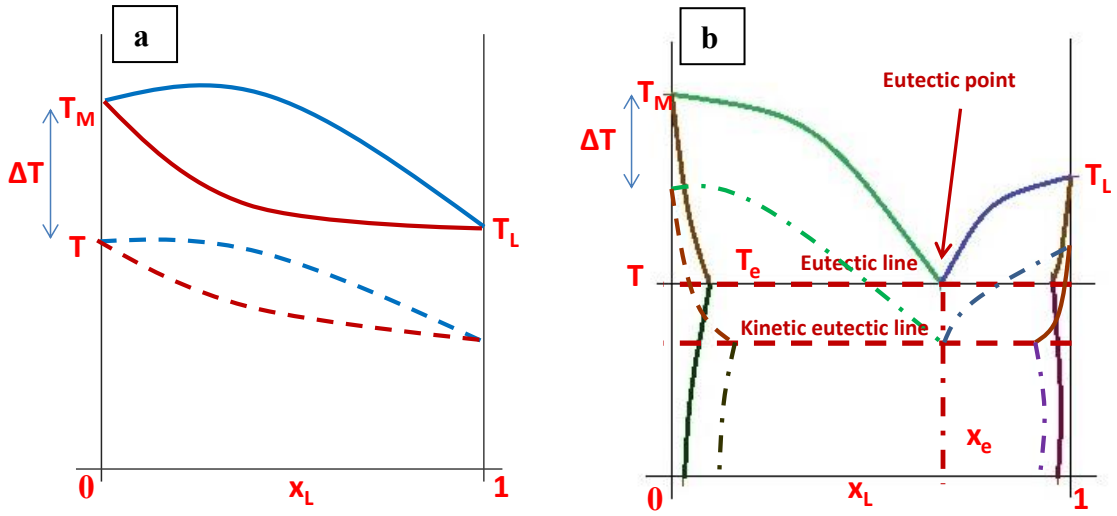

Figure 2-7. Equilibrium and kinetic two component phase diagrams. (a.) Continuous solid and (b.) Eutectic phase diagrams. Solid curves represent the equilibrium liquidus and solidus lines while the dotted lines represent the distorted kinetic liquidus and solidus. x_L is the trilaurin composition in a phase, T is the temperature of the system, T_L, T_M are the melting points of pure trilaurin and trimyristin crystallized in the polymorphic form of interest, ΔT is the degree of undercooling, T_e , x_e are the temperature and trilaurin composition at the eutectic point.

Wesdorp (1990) plotted theoretical binary phase diagrams of many monoacid and mixed acid TAGs using their pure component properties. He stated that phase diagrams predicting the formation of more than one crystalline phase can only be obtained if the interaction parameters (ϕ_{ij} and ϕ_{ji}) are fairly different from one another. One of the major challenges in modelling crystallization is polymorphic phase transitions as the enthalpies of crystallization and melting points largely depend on the polymorphic form. It is therefore important to make sure that there are no polymorphic transitions in the region where this LKS model is being applied.

2.2 Experimental methods to investigate crystallization

2.2.1 X-ray diffraction

X-ray diffraction (XRD) is the most extensively used technique to study crystallization of any class of materials. In the field of fat crystallization, XRD is extensively used to study the polymorphic form, polymorphic transformations and to

model kinetics of crystal growth (Clarkson & Malkin, 1934; Higami et al., 2003; Jensen & Mabis, 1966; Kellens et al., 1991; Kellens et al., 1990; Kellens & Reynaers, 1992; Kloek et al., 2000; Lopez et al., 2001; Lutton, 1945; Martini & Herrera, 2002; Mazzanti et al., 2003; Minato et al., 1996; Rousset & Rappaz, 1997; Sato, 1999; Sonoda et al., 2004; Takeuchi et al., 2003; Ueno et al., 1997; Zhang et al., 2007).

Different kinds of XRD techniques are available such as powder XRD and single crystal XRD each of which serve as a specific tool to study the arrangement of molecules for different systems. For fats the most commonly used is powder XRD, since the liquid crystallizes into billions of nanocrystallites collectively forming a powder-like distribution.

2.2.2 Principles of x-ray diffraction

2.2.2.1 Bragg's Law

When monochromatic x-rays interact with crystalline materials, they produce patterns which are related to the arrangement of layers of atoms/molecules in the crystal. In the case of TAGs, a crystal is made up of molecules that are arranged periodically with characteristic distances between consecutive layers, called d-spacings. When x-rays of wavelength λ are projected onto this crystal, at an incident angle (θ) called the Bragg's angle, x-rays elastically scattering from two different layers separated by a distance 'd' interfere constructively to produce a "bright spot" on a detector. The x-rays scattering at an angle different from Bragg's angle, essentially cancel each other by destructive interference. A pictorial representation is shown in Figure 2-8.

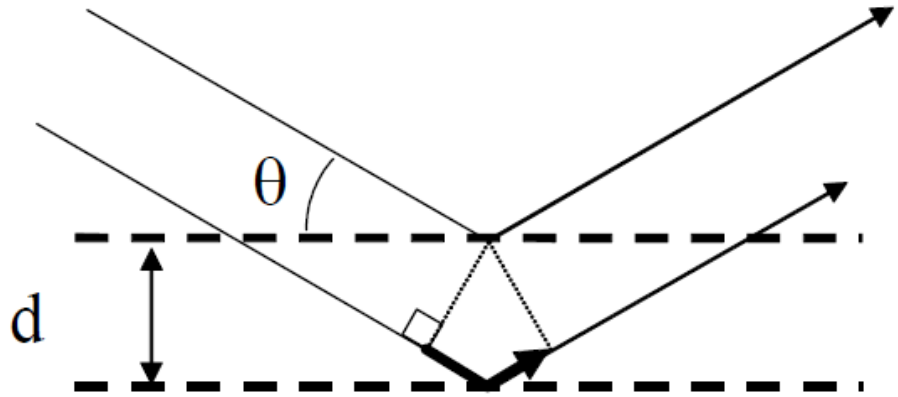

Figure 2-8. The dotted lines represent molecules in two consecutive layers separated by a distance 'd', x-rays having a wavelength λ are projected at an angle 'θ' bounce off from these two consecutive layers (Mazzanti, 2004).

Bragg's law laid the foundation of x-ray crystallography:

$$n\lambda = 2 \cdot d \cdot \sin\theta \tag{2-21}$$

Where *n* could be any natural number.

To permit universal comparison between diffraction patterns a scattering vector 'q' is defined as

$$q = \frac{4\pi \sin\theta}{n\lambda} \tag{2-22}$$

Substituting equation (2-20) and (2-21) in (2-22) yields,

$$q = \frac{2\pi}{d} \tag{2-23}$$

In reality, the x-rays which have an incident angle slightly different from Bragg's angle 'θ' do not completely cancel each other (Cullity, 1957). As a result diffraction patterns obtained are not sharp δ distribution functions but rather broad distribution functions either of a single kind or a convolution of more than one type of distribution functions. Two of the reasons for the broadening in diffraction patterns are:

- Imperfections in the angular resolution of x-ray beam. i.e., all the x-rays are not perfectly parallel to each other and have a finite distribution of incident angles.

- The number of layers in a crystal domain is not large enough to cancel all the x-rays bouncing off at angles slightly different from Bragg's angle.

Gaussian, Lorentzian or Voigt functions (a convolution of Gaussian and Lorentzian) are used to describe the experimental diffraction peaks.

2.2.2.2 Formation of Debye rings

Because the x-rays illuminate billions of crystallites that are randomly oriented, diffraction patterns produced by crystalline TAGs are rings instead of a single bright spot. These rings are called 'Debye Rings'. The radius ('Z') of these diffraction rings is related to the Bragg's angle 'θ' and thereby related to the scattering vector 'q' as shown in (2-24). This relationship is simply obtained by the definition of '*tanθ*' and (2-21) and (2-23) (See Figure 2-9).

$$q = \frac{4 \cdot \pi . \sin\left(\frac{1}{2} a \tan\left(\frac{Z}{X}\right)\right)}{n \cdot \lambda} \qquad (2\text{-}24)$$

Here,

Z is the radius of a Debye ring and *X* is the distance between the sample and the detector.

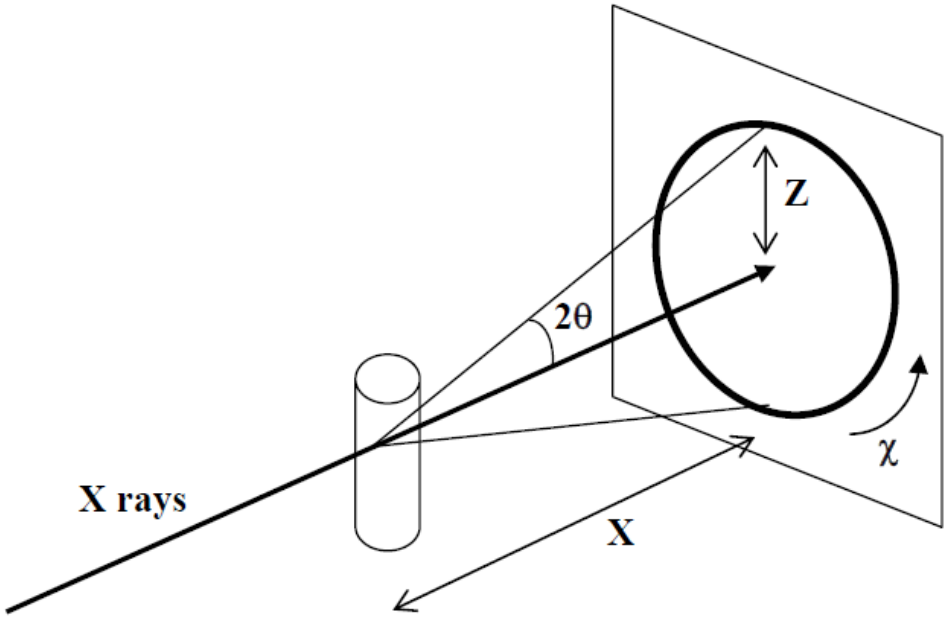

Figure 2-9. A sketch showing the formation of Debye rings from the diffracted x-ray beams of powder samples (Mazzanti, 2004).

The Debye rings are converted into radial plots like the one in Figure 2-10. Apart from the number of phases formed in a crystalline system, analysis of x-ray diffraction patterns gives three important pieces of information related to each crystalline phase, 1) Peak position, 2) Full width at half maximum (FWHM), and 3) Area of a peak.

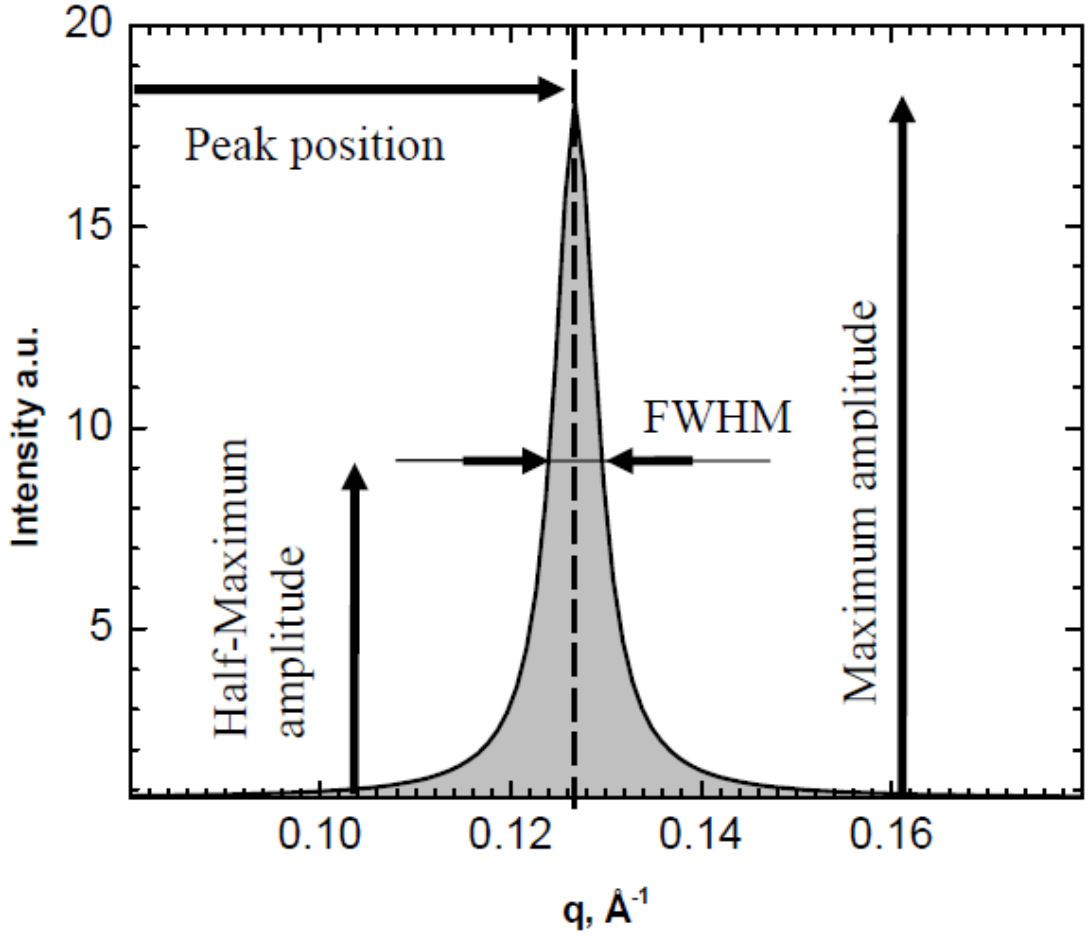

Figure 2-10. An example of a standard distribution functions used to describe x-ray diffraction peaks showing the three parameters peak position, FWHM and the region shaded in gray called peak area (Mazzanti, 2004).

The broadening of a diffraction pattern increases with the decrease in thickness of a crystal domain. If a crystalline phase has a large number of imperfections, the FWHM would not serve as a measure of crystal thickness, but is the effective length of the scattering domain called as the coherence length or correlation length (ξ) (Cullity, 1957).

The Debye-Scherrer approximation that is used to determine the thickness of a crystal domain is:

$$\xi = \frac{0.9\lambda}{\Delta d \cos\theta} \tag{2-25}$$

For small diffraction angles, the thickness of a crystal domain(ξ) can be approximated as:

$$\xi = \frac{2\pi}{\Delta q} \tag{2-26}$$

Δq is the FWHM of the diffraction peak in the units of scattering vector q.

2.3 Correlation between the results from the analysis of XRD experiments and the composition of a phase

All the methods explained in section 2.1.5.3 to describe and predict solid-liquid phase equilibrium are still theoretical and have not being tested experimentally. The first challenge to test the applicability of these models is to estimate the composition of the crystalline phase(s) growing from a liquid at a particular temperature. There are no methods available in the literature to experimentally estimate the phase composition so far.

A first attempt was made by (Anom, 2009) in his Thesis entitled "Comparison of the theoretical and experimental composition of crystallizing lipid mixtures". Binary mixtures of trilaurin and trimyristin of known composition were crystallized at different cooling rates and an empirical model was developed to relate the composition and d-spacing of a crystalline phase. The development of this model was performed using mass balance. (Anom, 2009)

The mass of a crystalline phase is related to the area under its diffraction peak through a proportionality factor(ψ) (Mazzanti & Mudge, 2009).

$$m = \psi \cdot A \tag{2-27}$$

In Anom's work, a linear relationship between the proportionality factor (ψ) and the composition of trimyristin (x_M) in the crystalline phase was assumed.

$$\psi_1 = k_0 + k_1 \cdot x_{M1} \tag{2-28}$$

A cubic relationship was assumed between the trimyristin (MMM) composition of phase and its d-spacing.

$$x_{M_1} = a_3 \cdot d_1^3 + a_2 \cdot d_2^2 + a_1 \cdot d + a_0 \tag{2-29}$$

The sum of trimyristin fraction in each phase should be equal to trimyristin composition in the liquid.

$$z_1 = \sum_{j=1}^{n} x_{M_j}^s \cdot \psi_j^s \cdot A_j^s \tag{2-30}$$

Where, z_1 is the average composition of trimyristin in the whole sample.

Initial guess values of parameters in equations (2-28) and (2-29) were made and an excel solver method was used to reduce the difference between the actual composition of liquid and estimated composition of liquid from the equation (2-30) by changing the initial guess values. A wide range of basic models like cubic, exponential, etc., have been tried in order to describe the best relationship between proportionality factor (ψ) and composition (x_M) and also the relationship between d-spacing (d) and composition(x_M). The results of this work were used as a starting point towards optimizing the relationship between d-spacing and composition in this Thesis.

2.4 Instantaneous phase composition

As described earlier, due to negligible diffusion in the solid phase, the composition of crystalline solid is not homogenous, i.e. if a spherical crystal is considered for convenience, the concentration of a particular component varies along the radius of the crystal. From the analysis of x-ray diffraction patterns, d-spacing and the diffraction area of a phase at any particular instance could be obtained. The calculated composition from this d-spacing will yield an average composition of the whole crystalline phase ($\bar{x}_j$). If a good set of proportionality factors between the area of a phase and its mass could be established, the change of composition with respect to the mass of a phase could be established. Using these two calculated values and by a simple conservation of mass, the

instantaneous composition($\bar{x}_{tj}$) of that particular phase can be calculated at any time *t* as shown in (2-31) (Mazzanti, 2004). The derivation for this expression is presented in section 6.4.

$$x_{tj} = \bar{x}_j + \frac{\partial \bar{x}_j}{\partial S_j} S_j \tag{2-31}$$

Chapter 3 EXPERIMENTAL METHODS

3.1 Materials

Crystallization experiments were conducted on different mixtures of trilaurin with trimyristin. Trilaurin and trimyristin are both fully saturated mono acid TAGs. Fatty acid chains of trilaurin have 12 carbon atoms while chains of trimyristin have 14 carbon atoms. There are many reasons for choosing these two compounds as model materials:

a. Considerable research has been carried out on these components in their pure state, which gives considerable information in terms of their physical properties and crystallization behavior.
b. The chain lengths of 12 and 14 carbons are closer to the chain lengths of triglycerides in natural fats and as a result, they can be used to describe natural fats and also at the same time can be easily handled in terms of melting and crystallization.
c. Due to a very small chain length difference of 2 carbons, these compnents are known to form solid solutions in all the polymorphic forms and have a very minute chance of forming crystalline phase(s) made up of a single component. Studying the formation of solid solutions is one of the main aims of this study as almost all of the naturally occurring fats form solid solutions.

Once a better understanding of the crystallization of binary mixtures of trilaurin-trimyristin mixtures is obtained, this knowledge can be extended to multi-component systems and further extended to mixed acid unsaturated TAG mixtures.

3.2 Sample preparation

Pure trilaurin (LLL) and trimyristin (MMM) were purchased from Sigma-Aldrich Chemical Co., Saint Louis, MO, United states with a reported purity of > 99%. Three binary mixtures of trilaurin with trimyristin on a weight basis were made without further purification. The LLL: MMM ratio in these three binary mixtures is 30:70, 50:50 and 70:30 and are termed as 3L7M, 5L5M and 7L3M. Thin wall glass capillaries of diameter 1.5 mm were bought from ‘Charles Supper Company’ and were used to hold the TAG

mixtures. The three binary mixtures of TAGs were melted on a heating plate and were stored at about 80°C for a few minutes to eliminate concentration gradients in the liquid and make a homogenous mixture. About 20 μL of these binary liquid mixtures were measured by glass pipets manufactured by 'Drummond Scientific Company' called 'Wiretrol II'. Two sets of capillaries for each binary mixture were made. The capillaries were flame sealed.

3.3 Testing the actual composition of binary mixtures

The development of a correlation between the d-spacing and composition of a crystalline phase is done through mass balances, so, it is important to accurately know the composition of the liquid from which the system is crystallizing.

The fatty acid profiles of these binary mixtures were estimated using gas Chromatography (GC). As these binary mixtures were made up of pure TAGs, it is fair to assume that the fatty acid composition would be the same as the TAG composition. The binary mixtures were converted into more volatile fatty acid methyl esters (FAME) by using an acid catalyzed transesterification procedure described in 'Appendix A'.

The actual composition of the binary mixtures was determined from a GC. The transesterification procedure and GC procedure are described in 'Appendix A'. Table 3-1shows the actual composition of each sample used in this Thesis as determined by GC. Multiple runs to quantify the variability in the composition of each sample were not possible due to limited availability of the sample.

Table 3-1. Mass fraction and mole fraction of trilaurin in both sets of samples used to perform XRD experiments, measured using a GC

Sample Name	Synchrotron		In-house	
	Mass fraction	Mole fraction	Mass fraction	Mole fraction
3L7M	0.2244	0.2466	0.3077	0.3346
5L5M	0.4603	0.4911	0.5288	0.5595
7L3M	0.7276	0.7514	0.7301	0.7537

3.4 X-ray diffraction experiments

Regular lab scale XRD systems equipped with molybdenum source or copper source produce a very low flux of x-rays. A very long exposure time is required to produce a diffraction pattern with a good resolution. These lab scale set ups are of use in studying equilibrium conditions or very slow transformation processes. The crystallization of TAGs is considered a rather fast process. As a result, studying the kinetics of a crystallization process is not possible with a lab scale x-ray diffraction system. Thus, diffraction experiments have been performed using a very high flux of x-rays such as those produced from a synchrotron source. This high flux of x-rays allowed the capture of large number of diffraction patterns in shorter time intervals. This allowed the study of the kinetics of fat crystallization under isothermal conditions. Another advantage of using synchrotron sources is their ability to adjust the wavelength of x-rays being emitted. The wavelength of x-rays produced from a molybdenum source is about 0.71 Å. These high energy x-rays have high penetration power and thereby interact less with materials being studied, while x-rays produced by a copper source have a higher wavelength (1.54 Å). Radiation having a longer wavelength of this order has the disadvantage of higher absorbance with experimental containers and thereby reducing the number of x-rays producing a diffraction pattern. So, from the experience of previous studies, a wavelength of about 1.1 Å is found out to be in a region which is a good compromise between high penetration and high absorbance and hence producing diffraction patterns of superior quality (Cisneros et al., 2006; Mazzanti et al., 2004a, 2004b).

3.4.1 Synchrotron radiation x-ray diffraction (SR-XRD)

SR-XRD experiments were performed on the binary mixtures of TAGs at beamline X10A of National Synchrotron Light Source (NSLS) at the Brookhaven National Laboratory (BNL) situated in Upton, New York. (Figure 3-1 and ‘Appendix B’)

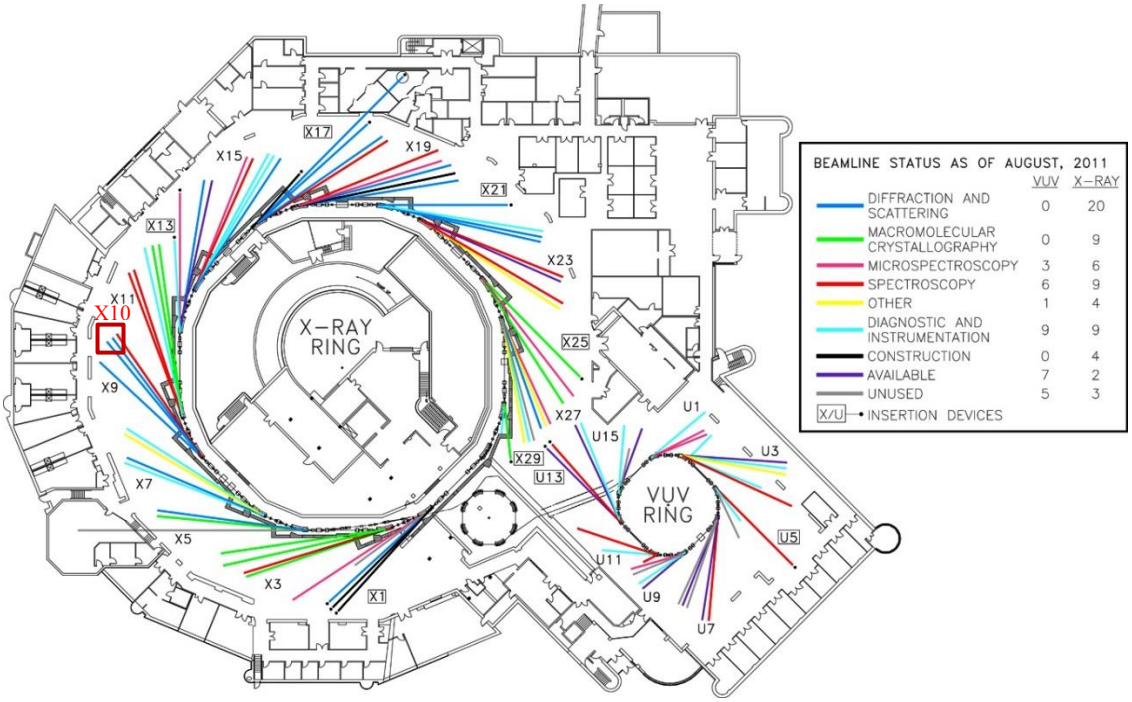

Figure 3-1. Floor plan of the National Synchrotron Light source at BNL showing storage rings and beam lines. X-rays originating from bending magnet X10 are further split into three beam lines X10A, X10B and X10 C ("Brookhaven National Laboratory,").

3.4.2 Experimental procedure and setup

The energy of x-rays entering the beamline hutch of X10A can be adjusted between 8-17 keV which corresponds to a wavelength range of 1.5498 Å to 0.72932 Å. A monochromator is used to adjust the wavelength of the incoming radiation to a certain value. As discussed earlier, the wavelength of the x-rays is adjusted to be around 1.1 Å. This incoming beam is then focused using mirrors. Adjustable slits are used to define the dimensions of the beam at the sample. The beam was 0.5 mm x 0.5 mm. The wavelength was measured to be 1.09484 Å by analyzing x-rays scattered from aluminum oxide (Al_2O_3). Figure 3-2 shows a schematic of the setup.

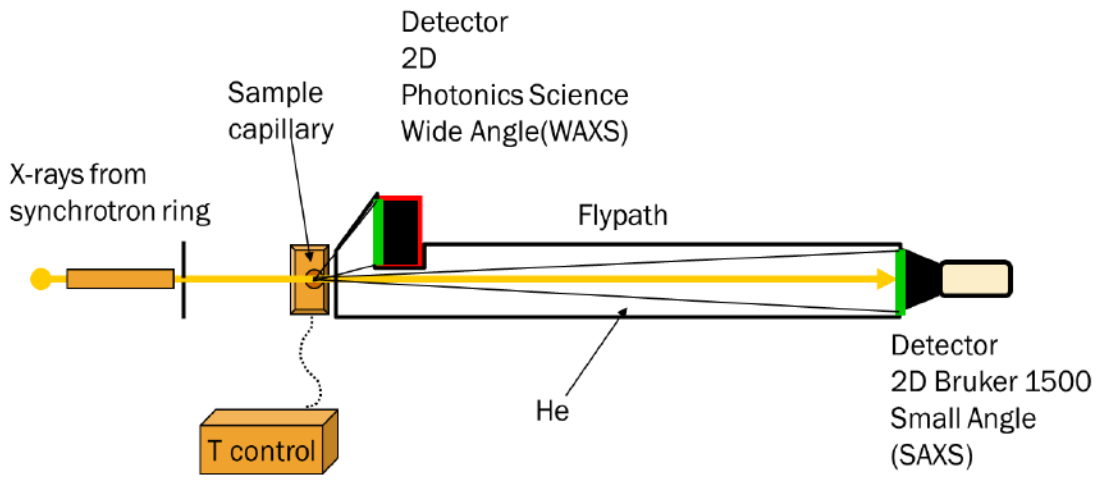

Figure 3-2. Setup for x-ray diffraction experiments performed at National Synchrotron Light Source (drawing by Dr. Gianfranco Mazzanti).

The components are:

a. Sample capillary holder

This is an aluminium holder mounted on a goniometer. It has a set of Peltier elements to control the temperature of the sample, monitored by a thermistor (15 kOhm, TS-67, Oven Industries Inc, Mechanicsburg, PA, US., reproducible to ± 0.01 °C) placed next to the capillary. It has a window for x-rays.

b. Temperature controller and PID algorithm

The temperature is controlled through the voltage applied across the Peltiers. A Labview program (described in the next sub-section) provides a set point from a pre-defined temperature profile. The voltage applied across the Peltiers is computed by a PID (Proportional, Integral Derivative) algorithm.

c. Labview program

The program was jointly developed by Dr. Gianfranco Mazzanti and Dr. Stefan Idziak, and improved by the author, in a National Instruments LabView environment to control the temperature of the capillary cell and also to log the temperature and other operating parameters. It was further modified by the author. This program has a graphical user interface (GUI) which enables the user to input a temperature profile. This Labview

program has several loops running in parallel in which set point temperature is dynamically calculated in accordance with the stage in the temperature profile and time. This set point temperature is then transferred to the temperature controller. The other main functions of this program are to create a log file for each temperature cycle and record the time, actual temperature and set point temperature of the capillary cell. It also sends the temperature of the capillary cell to another program which captures and saves the diffraction patterns from one of the detectors.

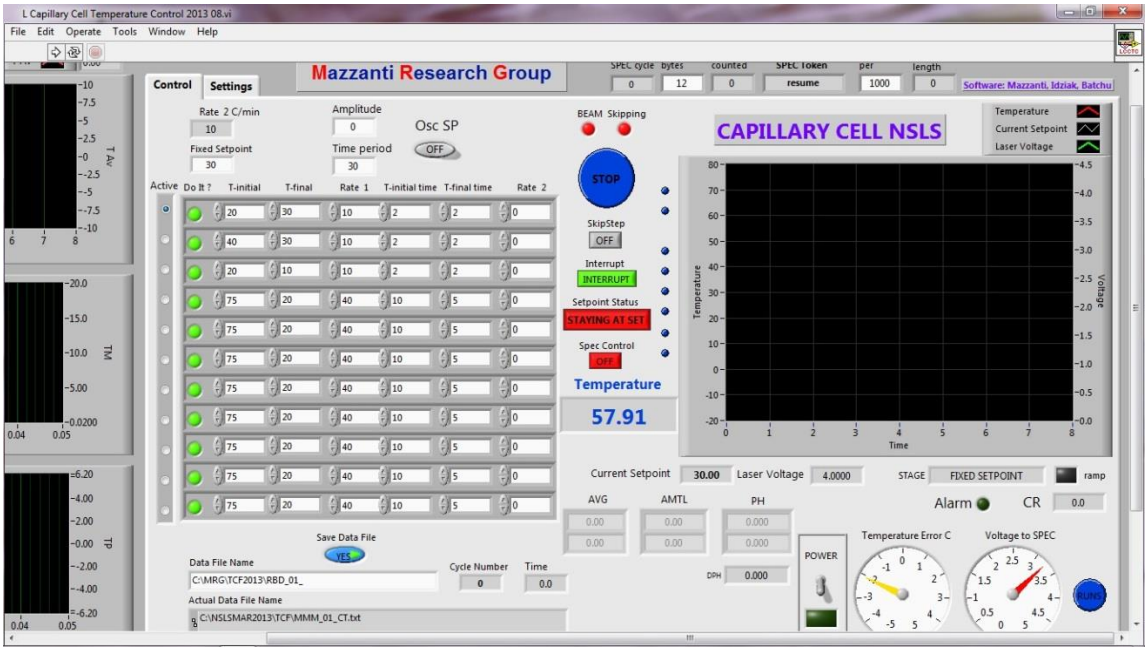

Figure 3-3. A screenshot of the capillary cell temperature control program's GUI showing different functionalities of the program

d. Detector to collect small angle diffraction patterns

A Bruker 1500 2D detector captures the diffraction patterns in the small angle region. This detector has a pixel size of 0.2004 mm. The pixels on the camera are binned to a resolution of 512 x 512. This detector is placed at a distance of 1059.47 mm from the sample holder. The precise distance between the capillary cell and the detector is found out by analyzing the diffraction patterns of a Silver behenate standard. The acquisition of images using this detector is controlled by a program called 'Bruker Smart'. The acquisition of the diffraction patterns is automated by a program called 'SPEC' which communicates with Bruker Smart to acquire images for a particular time length and save

them. The diffraction patterns are saved after subtracting the 'Dark field image' from the acquired image.

e. Detector to collect wide angle diffraction patterns

A Laue camera manufactured by Photonic Science, Robertsbridge, East Sussex, UK, is also a 2D x-ray detector available in the beamline hutch. It is a special camera generally used for x-ray backscatter experiments. In our experimental setup, this camera is utilized for simultaneous capture of wide angle diffraction patterns with small angle diffraction patterns. The pixel size of this camera is 0.3387 mm and it is placed at a distance of 341.09 mm from the sample. This precise distance between the sample and the detector is found by analyzing the diffraction patterns of different orders obtained from an aluminum oxide sample (Al_2O_3). A custom plug-in for the ImagePro software runs independently of the other systems and is used to capture WAXD patterns at constant time intervals as defined by the user.

f. SPEC control

This is a UNIX based software developed by 'Certified Scientific Software', Cambridge, MA., and is specifically designed for control and data acquisition of XRD systems. This program acts as the centralized control for almost all the equipment assembled in the beamline hutch. This program is used to control different parts of the experimental set up like moving the position of the detector, sample post, etc. This program is also used to control the beam size by opening and closing slits, attenuate the x-ray beam to a required intensity, etc. One of the most important features is the ability to automate the capture and saving of XRD patterns at constant time intervals by communicating with the software 'Bruker Smart'.

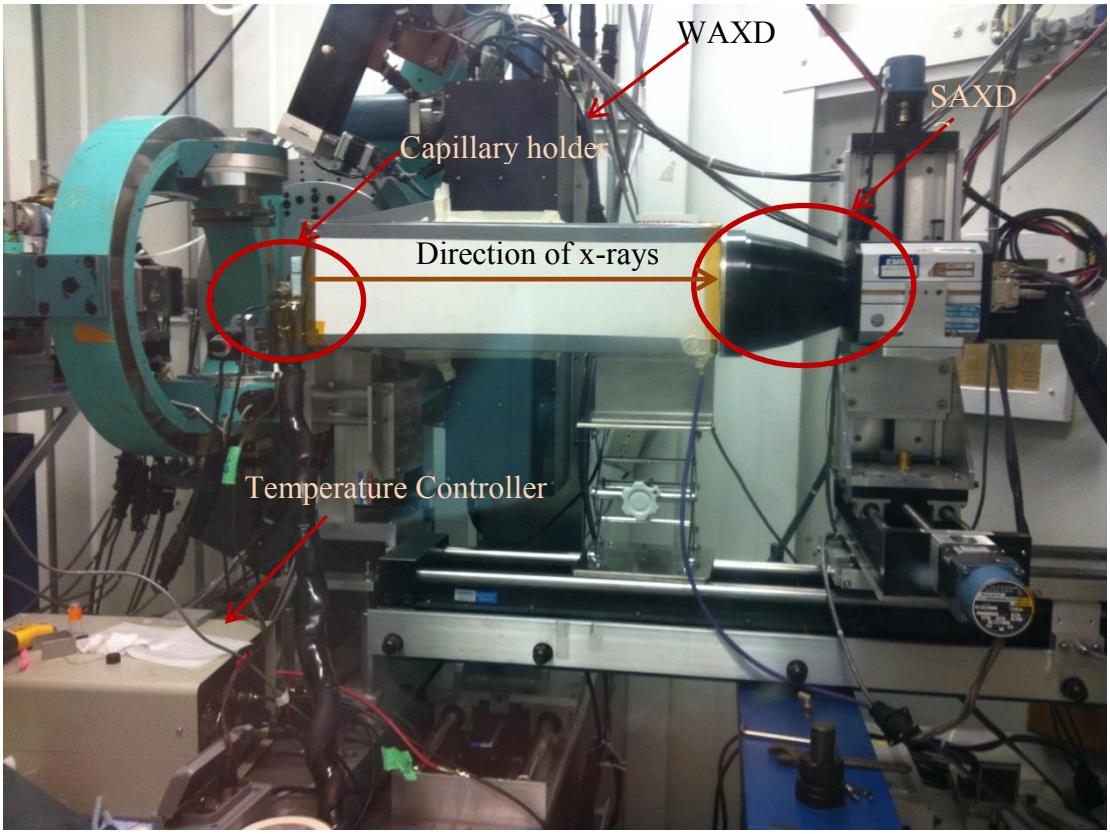

Figure 3-4. A photograph of the experimental setup at Beamline X10A of NSLS showing the key components

3.4.3 Temperature profiles

A temperature profile has three parts, melting temperature, cooling rate and final temperature, and the corresponding holding times at each temperature. All the three binary mixtures were initially melted at 75°C for 10 min to make a homogeneous liquid mixture. This liquid at 75°C is cooled down at a cooling rate of 50°C/min to a particular temperature where the crystallization takes place. These holding temperatures were chosen based on the composition of the binary mixture. After crystallization, these samples were heated back to 75°C. The time at which the set point changes to 75°C is considered the start of a single experiment. Figure 3-5 shows an example of a typical temperature profile.

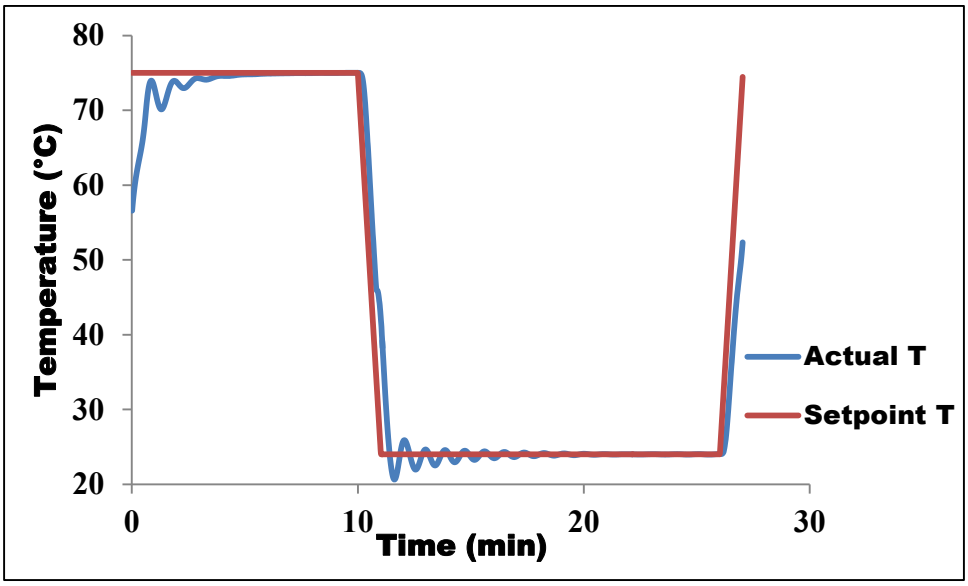

Figure 3-5. A typical temperature profile showing the change of the set point temperature and the corresponding actual temperature with time - This profile corresponds to the binary mixture 5L5M crystallized at 24 °C.

Isothermal crystallization has been studied at every 1 °C between a chosen temperature range for each sample. The temperature range that is chosen for each mixture is shown in Table 3-2. These temperatures were chosen based on the composition of the mixture and the melting point of pure components. Each experiment was conducted in duplicate.

Table 3-2.Holding temperatures at which crystallization was studied for the three binary mixtures of trilaurin and trimyristin

Mixture	Temperatures (°C)
3L7M	24°C to 33°C
5L5M	22°C to 31°C
7L3M	16°C to 26°C

3.4.4 Acquisition times of diffraction patterns

The exposure time of each small angle diffraction pattern (SAXD) was set to 20 seconds. The system takes about 3 seconds to save each image and hence the time

difference between two successive small angle images was 23 seconds. The exposure time of a wide angle diffraction pattern was set to be 2.5 minutes.

3.5 In-house x-ray diffraction experiments

As described in Chapter 1, one of the core objectives of this study is to develop a correlation between the d-spacing of a crystalline phase and its composition. The development of this correlation relies on mass balance. It is necessary to make sure that the experiments attain complete crystallization. Due to the time limitation, each crystallization experiment was not run for very long at the synchrotron. The analysis of data obtained from the synchrotron showed that many experiments done with the samples 3L7M and 5L5M did not attain complete crystallization. It was thus difficult to develop a reliable correlation with limited data points. Therefore, SAXD experiments were done with an in-house x-ray source, using much longer times at the holding temperature. These XRD patterns were used in the development of a correlation between d-spacing and the fat composition.

3.5.1 Experimental set up

3.5.1.1 x-ray generation and path

A commercially available GeniX x-ray source (Xenocs Corporation Sassenage, France) is used as the x-ray source in our in-house x-ray diffraction experimental setup. This source has a molybdenum anode producing K_α radiation of wavelength 0.7093 Å. X-rays produced are focused using a toroidal mirror into a fly-path and are projected with an approximate size of 0.4 x 0.4 mm onto the sample. The sample holder described in section 3.4.2 was used in the in-house XRD experiments as well. A flypath with a partial vacuum between the sample and the detector reduces the scattering of x-rays by air. An interlocked enclosure around the system isolates it from the surroundings and reduces the risk of human exposure to x-rays.

3.5.1.2 Acquisition of images

A 2D x-ray detector called XRI-UNO/Si manufactured by Xray-imatek, situated at Barcelona, Spain is used in the in-house XRD setup. It has an active area of 14 mm x

14 mm built with an array of silicon sensors. It has a pixel size of 0.055 mm x 0.055 mm. The acquisition of images is carried out by software also called 'XRI-UNO' which runs in parallel with the SPEC software controlling the shutters of the x-ray generator and the movement of the motors in the system.

Crystallization experiments were performed to determine the d-spacings and area fractions of the phases formed once the crystallization was completed. The completion of crystallization was verified by looking at the trend of the integrated intensity of each of the crystalline phases obtained from the analysis of experiments performed at the synchrotron. The point at which the integrated intensities (areas) stop changing and attain a plateau can be considered as an indication of the completion of crystallization.

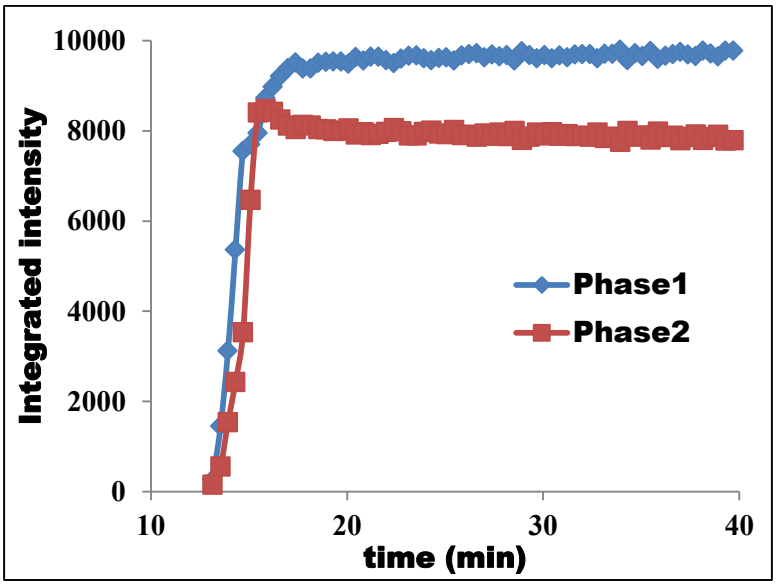

Figure 3-6. Integrated intensity changing with time for each crystalline phase obtained from the sample 7L3M crystallized at a temperature of 21°C. The point at which these integrated intensities reach a maximum is considered as the completion of crystallization

Two capillaries were made for each binary mixture. Each experiment was run twice on the same capillary and once on the second capillary to test for repeatability and reproducibility. Table 3-3 describes the name of the sample and the corresponding holding temperatures at which crystallization experiments have been performed.

Table 3-3. Temperatures that were chosen to study crystallization for the three binary mixtures of trilaurin and trimyristin with In-house XRD setup. Temperatures are selected at an increment of every 1°C between the temperatures mentioned.

Mixture	Temperatures(°C)
3L7M	20°C to 30°C
5L5M	20°C to 30°C
7L3M	16°C to 28°C

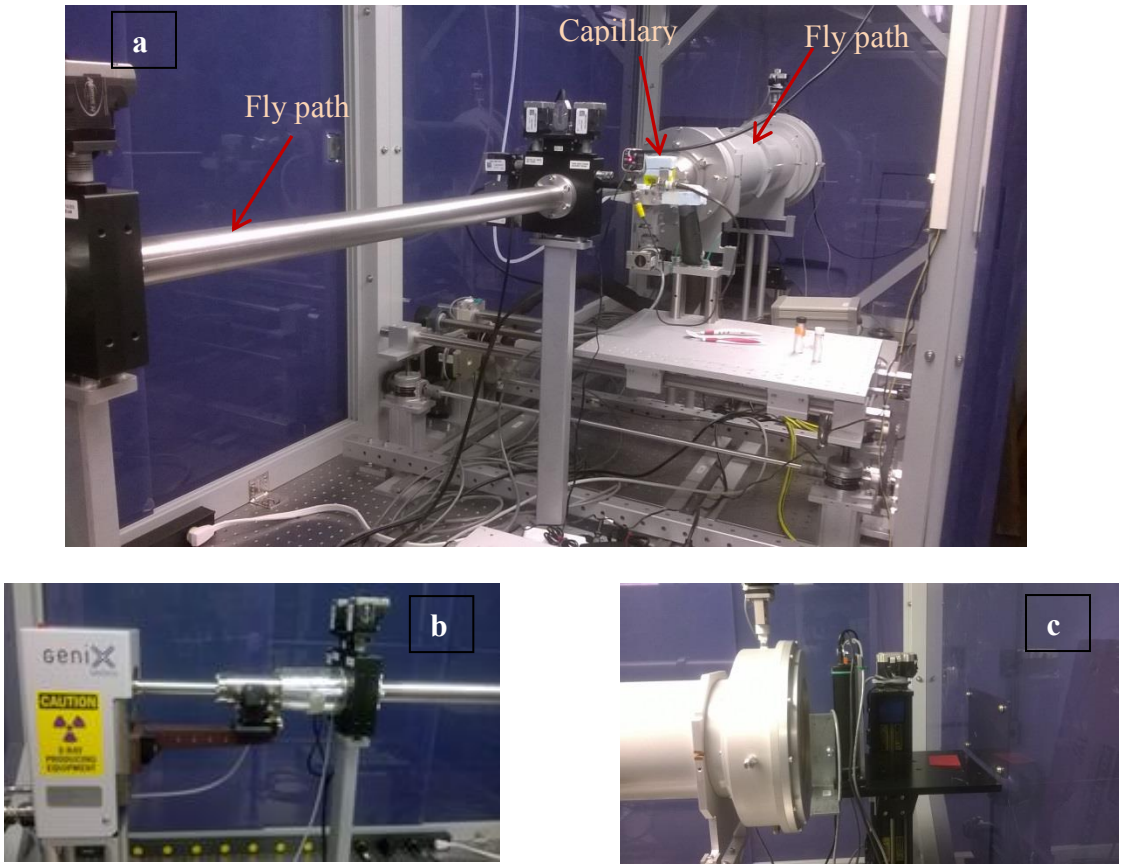

Figure 3-7. In-house experimental setup for x-ray diffraction experiments. (a) Picture showing the position of the capillary holder and flew paths. (b) x-ray generator and (c) 2D detector for capturing diffraction patterns

3.5.1.3 Temperature profiles and acquisition times

The temperature profiles used in the in-house XRD experiments were similar to those at the synchrotron, the only difference was the time at the holding temperature. Due to the low intensity of the x-ray beam in lab scale XRD equipment, a longer exposure

time is needed to obtain diffraction patterns with good resolution. Experiments done at relatively lower temperatures (< 28°C) were held for 150 minutes. As the onset of crystallization is delayed and the rate of crystallization is slower at relatively higher temperatures, a longer holding time of 250 minutes was used at temperatures of 28°C and above.

Images were taken every minute. After the experiment was complete, the mean intensity of each image against the image number was plotted. This plot reached a plateau once the crystallization was complete. All the images taken after experiment completion were added together to form a single image that was then analyzed.

3.6 Processing acquired data

The diffraction patterns undergo the following steps to produce the radial plots (details in in 'Appendix C':

a. Unwarping: Unwarping is performed to remove the distortions caused in a diffraction pattern due to the transfer of an image from the CCD detector to a chip through a bundle of tapered optical fibers (only for patterns captured at Synchrotron).
b. Filtering: This step is performed to remove the discrepencies caused by defective points on the CCD surface and also zingers caused by cosmic radiation that account for noise in a diffraction pattern (only for patterns captured at Synchrotron).
c. Creation of radial plots: Each Debye ring is converted into radial plots that are average radial intensities as a function of scattering vector 'q' for further analysis. Prior to this step a very precise center of each Debye ring is needed.
d. A normalization procedure is performed on all the radial plots together to make the comparison possible.

3.7 Analysis of diffraction patterns using Igorpro 6

The 'Igorpro 6' software developed by Wavemetrics Inc, Portland, OR, US., was used to resolve each diffraction pattern into background and diffraction peaks. The peak fitting starts with initial guess values given manually. Then Igorpro uses a Levenberg-

Marquardt algorithm to find the set of parameter values for each fitted distribution funtion at which the sum of squared errors between experimental and calculated patterns becomes minimum. The calculated pattern is simply a summation of the fitted statistical distribution functions and the background.

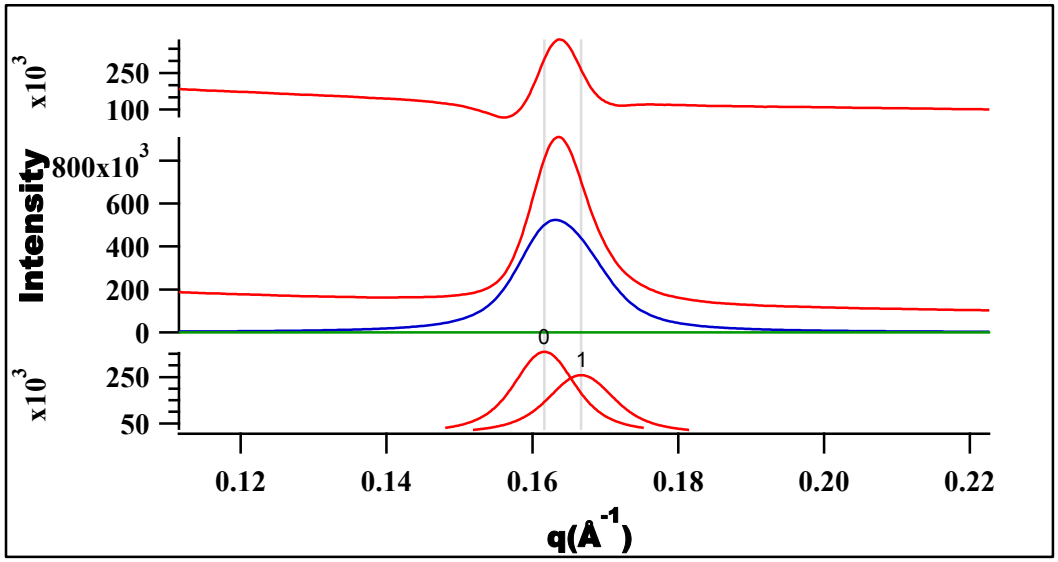

Figure 3-8. A sample diffraction pattern with two guess 'Voigt' peaks on a quadratic background in Igorpro

In Figure 3-8, the top part represents the residuals between the experimental and calculated patterns, the red curve in the center part is the actual experimental diffraction pattern and the blue curve is calculated pattern using the baseline function and the two guess distribution functions. The green line/curve represents the baseline function. The bottom part of the figure describes each of the individual distribution functions guessed.

The resultant peak fit is shown in Figure 3-9.

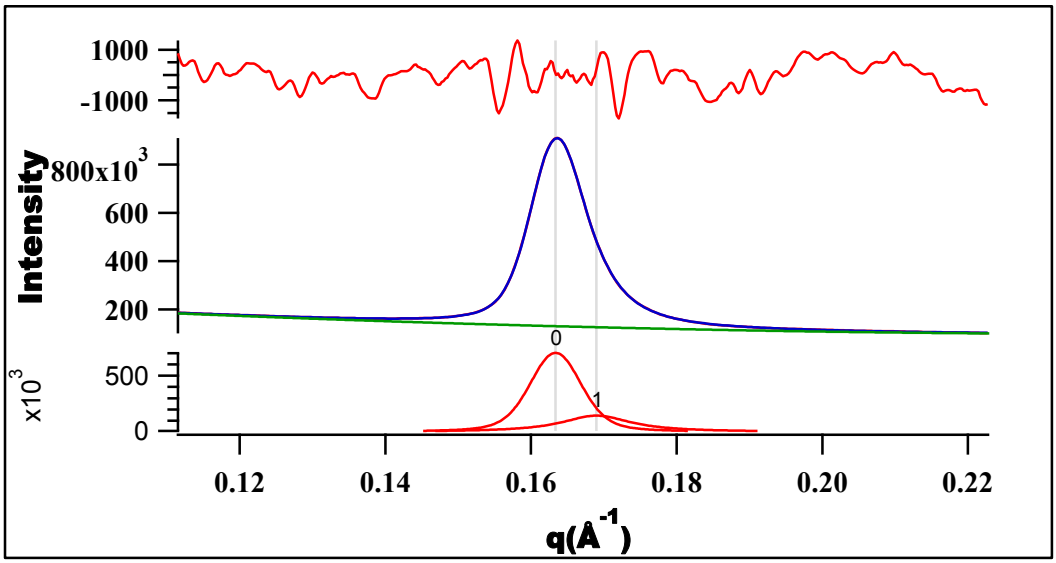

Figure 3-9. End result of the peak fitting procedure produced by Igorpro showing the distribution functions with optimal parameters

The center part of Figure 3-9 shows an overlap between the actual and calculated diffraction patterns. This is an indication that the combination of these fitted functions after the minimization of error is in good agreement with the experimental diffraction pattern.

3.7.1 Types of statistical distribution functions used in peak fitting

IgorPro uses a rearranged version of a Gaussian function in its peak fitting procedure:

$$p_G = y_0 + A \cdot \exp\left[-\left(\frac{x-\mu}{width}\right)^2\right] \tag{3-1}$$

In equation (3-1),

p_G refers to peak Gaussian

μ is the peak position or the value at which the function has the maximum amplitude,

width is the full width at half maximum of the function which is $\sqrt{2}\cdot\sigma$

'A' is a function of the amplitude

The Lorentzian function used by Igorpro is:

$$p_L = y_0 + \frac{A}{(x-\mu)^2 + B} \tag{3-2}$$

Where,

p_L refersto peak Lorentzian

Y_0 sets the offset of the distribution function

'A' is the amplitude of the function

μ is the peak position or the value at which the function has the maximum amplitude

'B' is the width and the amplitude of the function

Sometimes these distribution functions are not good enough to describe the peaks. A Voigt function, which is a convolution of 'Gaussian' and 'Lorentzian' functions, is then used. A 'Voigt' distribution function is described by four parameters which are:

Position

Width

Height and

Shape

The fourth parameter shape is the ratio of widths Lorentzian over Gaussian, and thus can vary from 0 to ∞. A value of 0 represents a pure Gaussian distribution and ∞ represents a pure Lorentzian distribution function.

3.8 Monte Carlo method

A Monte Carlo method was used to estimate the confidence intervals for the parameters of the correlation that describe the relationship between d-spacing and composition of a crystalline phase. The development of this model is described in detail in Chapter 5. Utilizing the standard deviation in the measurement of experimental data points, a random data set was generated that contained 1000 points for each experimental data point. The parameters of the correlation were fitted for each of the randomly generated datasets and a 95% confidence interval was estimated using these fitted parameters.

3.8.1 Determination of dependency between experimental variables

If the error in the measurement of a particular experimental variable has a certain level of dependency on the error of other experimental variables that are simultaneously measured, it is necessary to retain this interdependency in random variables generated from the experimental data. The dependency of one variable upon another can be estimated by calculating an error covariance matrix and a correlation matrix. However, most methods used to generate correlated random variables assume a linear relationship between variables. It is very clear from the plot of variables (Figure 5-6) that their relationship, in this case, is not linear. A different approach was thus used to generate the random data sets. It is explained in Chapter 5 "Relationship between d-spacing and composition".

3.8.2 Generation of random datasets for performing the Monte Carlo analysis

A pooled standard deviation (σ_{pooled}) for the experimental variables d-spacing and area of each phase were estimated for the synchrotron data and in-house data separately. The software 'Igorpro' has a function ('gnoise') to generate a Gaussian noise with a specified standard deviation. Random datasets of 1000 data points were generated by adding noise for each of the original data points. A macro written in Igorpro (Appendix D) automated this process.

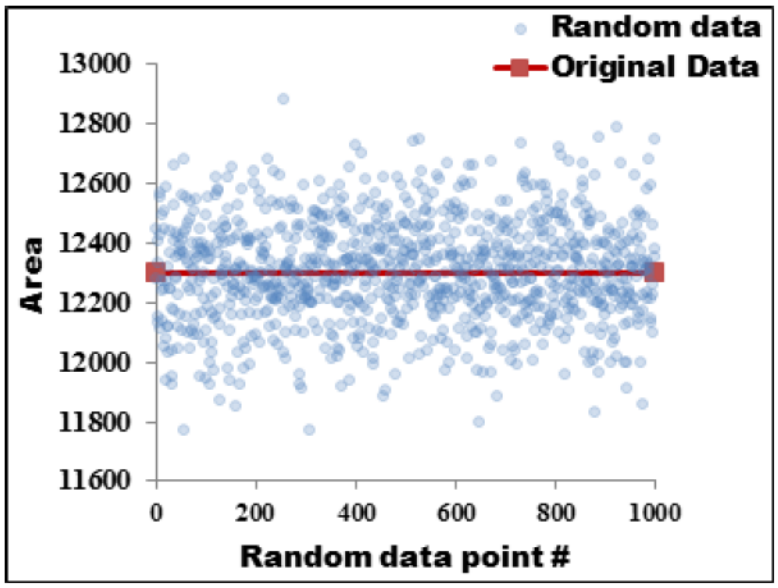

Figure 3-10.Distribution of the random areas generated by igorpro macro around the measured experimental value

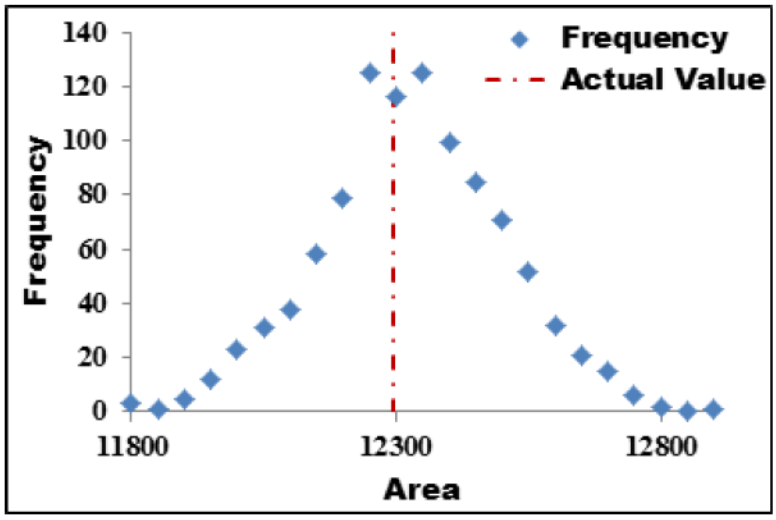

Figure 3-11.Plot showing the frequency count of the generated random data points showing a Gaussin like distribution with mean value around the actual experimental data point

3.8.3 Method to estimate the confidence intervals of fitted parameters

An Excel macro ('Appendix E') was created to find the set of parameters that fitted the correlation to each generated random data set. The macro thus produced 1000 sets of parameters. The mean value of each of the set of parameters was calculated and

the confidence interval of each fitted parameter was calculated from the 1000 sets of parameters produced.

Chapter 4 GENERAL TRENDS

This chapter illustrates the following trends of time-resolved small angle x-ray diffraction patterns for the three binary mixtures crystallized at different temperatures:

- The number of crystalline phases
- The d-spacings of the crystalline phases
- The diffraction area of each crystalline phase
- The thickness of the nanoplatelets of each crystalline phase

4.1 Number of crystalline phases and their d-spacings

Each experiment ends when the temperature begins to increase as shown in Figure 3-5. At the end, the three binary mixtures had formed two crystalline phases, regardless of the temperature. The d-spacings of these crystalline phases changed very little with temperature yet depended largely on the composition of the sample. In all the plots phase ending with '1' represents the first crystalline phase or the phase wih higher d-spacing and '2' represents the phase with smaller d-spacing obtained from a particular binary mixture

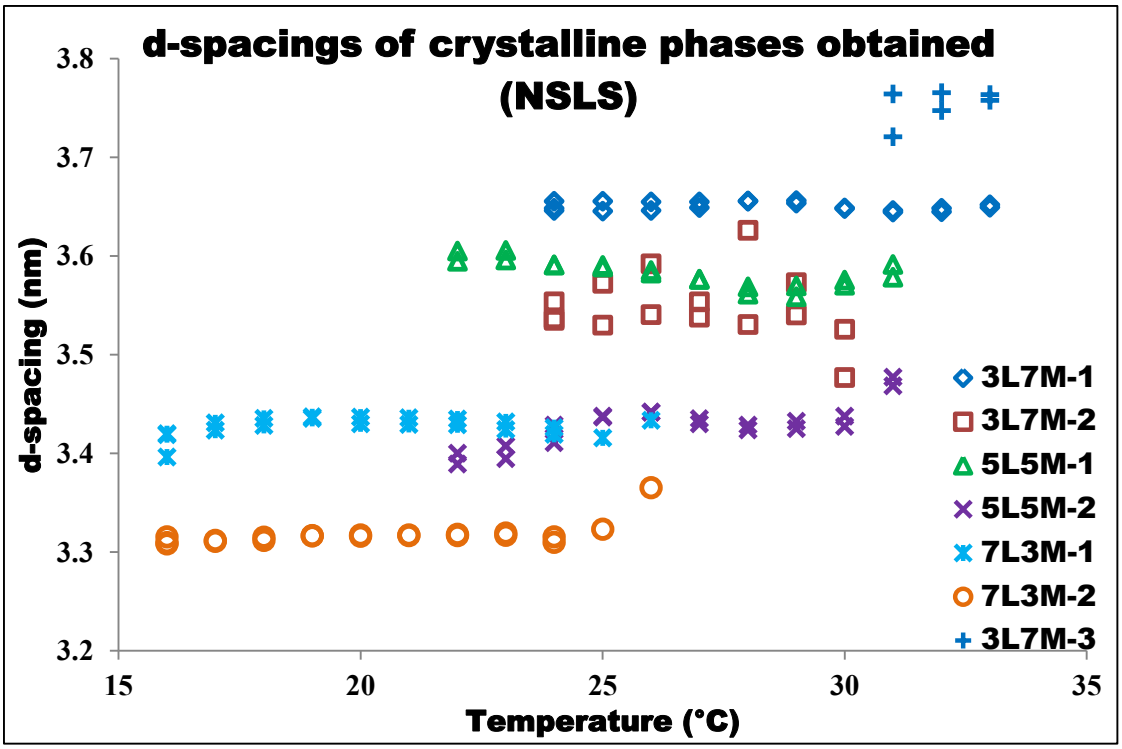

Figure 4-1. d-spacings of both the crystalline phases obtained at different holding temperatures for all the three binary mixtures of trilaurin with trimyristin at the end of an experiment (end of an experiment refers to the time just before the start of a heating ramp).

Figure 4-1 shows that the crystalline phases form in a preferential set of sequential pairs in most of the experiments conducted. The term 'sequential pair' corresponds to the trend that the second crystalline phase obtained upon the crystallization of the first binary mixture tend to have the same d-spacing as the first crystalline phase obtained from the second binary mixture. Thus, four preferential crystalline phases were observed in total. These groups of more stable preferential compositions did not appear under non-isothermal crystallization (Anom, 2009). A peculiar phase with higher d-spacing (depicted as 3L7M-3 in Figure 4-1) was observed in the case of 3L7M, at crystallization temperatures above 30 °C. The occurance of this phase might probably due to the temperature of crystallization being higher than the melting point of the regular phase (shown as 3L7M-2 in Figure 4-1) that was observed at other temperatures explored. The WAXD patterns, obtained simultaneously with the SAXD patterns, correspond to the β' polymorphic form for all the crystalline phases (See Chapter 7). The d-spacing of the

binary crystalline phases is related to their composition (Anom, 2009). Phases rich in trimyristin have higher d-spacing than phases rich in trilaurin. (See Chapter 5). Therefore, phases having higher d-spacing tend to have a higher melting point and vice versa. The large d-spacing of 3.75 nm for phase 3L7M-3 in Figure 4-1 corresponds to a phase that is very rich in trimyristin and can be solid at higher temperatures.

4.2 Change of d-spacings with time

The d-spacing of each crystalline phase is plotted as a function of time in the following figures. In all the plots 1- represents the first crystalline phase or the phase wih higher d-spacing and 2- represents the phase with smaller d-spacing obtained from a particular binary mixture.

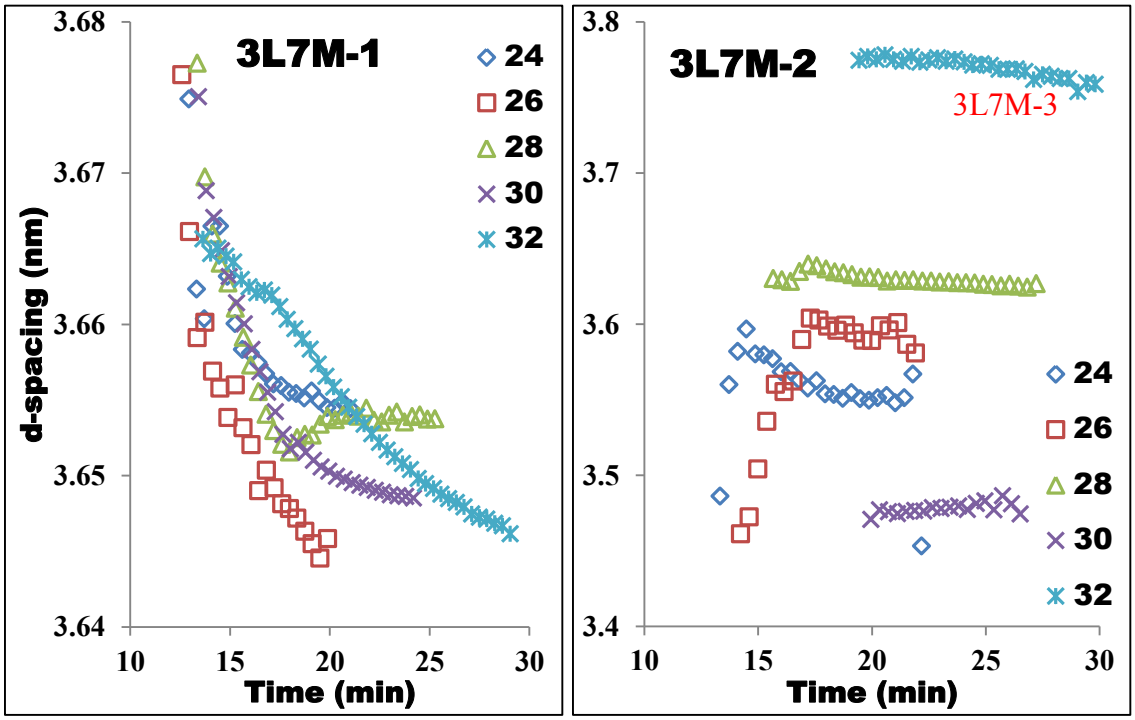

Figure 4-2. d-spacings of crystalline phases formed from 3L7M at selected temperatures as a function of time. The crystallization temperatures (°C) are shown in the legends.

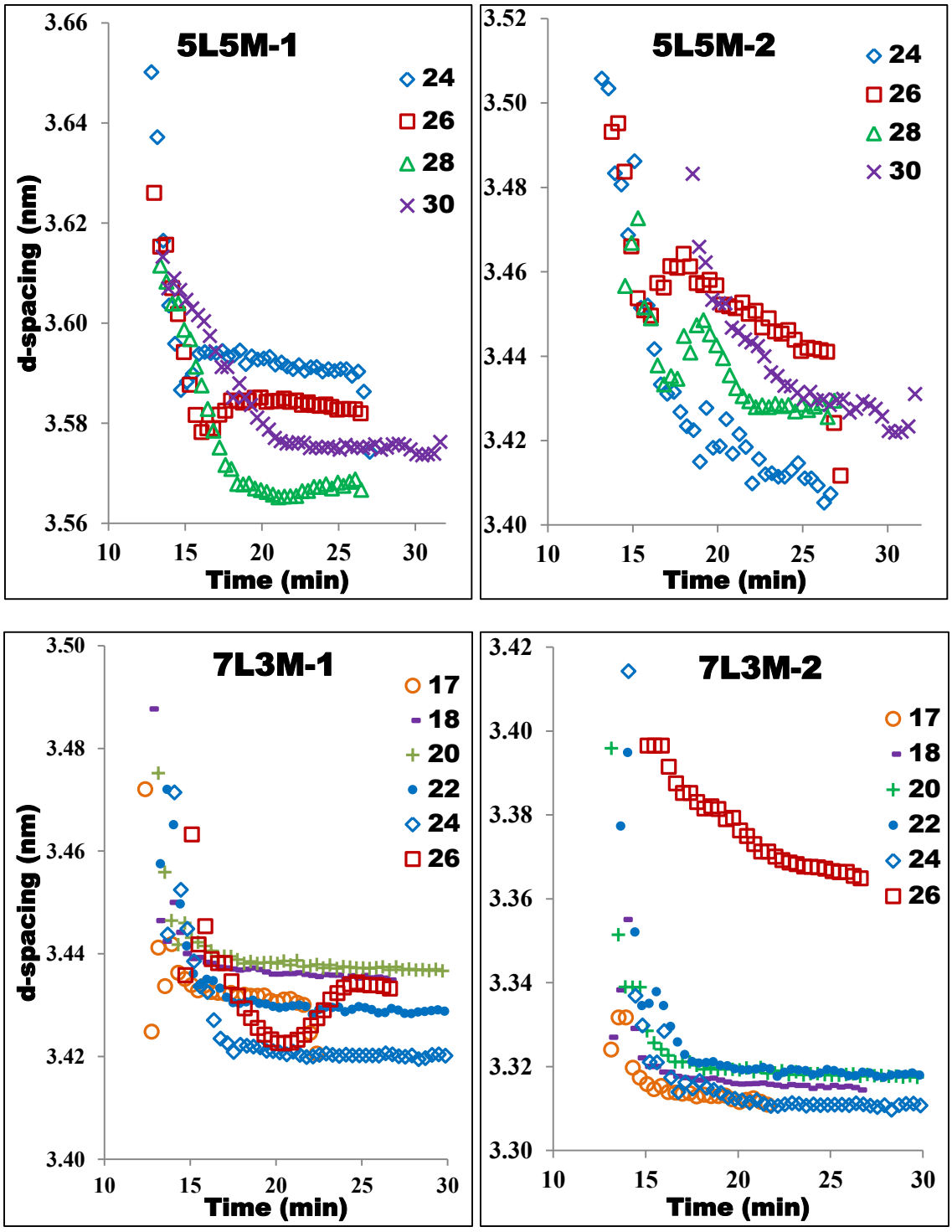

Figure 4-3. d-spacings of crystalline phases formed from 5L5m and 7L3M at selected temperatures as a function of time. The crystallization temperatures (°C) are shown in the legends.

The d-spacing decreased with time in almost all the crystalline phases. Thus, each crystalline phase starts with a low composition of trilaurin that increases as the crystallization progresses. The inverse is true for trimyristin. Therefore, the liquid becomes depleted of trimyristin as the crystallization progresses.

4.3 Change in diffraction area of crystalline phases with time

After normalization to the incident beam intensity, there were still differences in the total intensity of the diffracted x-rays for each experiment. These differences can be due to many factors, such as the actual diameter of the capillary or very small differences (> 100 μm) in the position of the capillary with respect to the beam. In order to eliminate these differences, the area fraction was used instead of the absolute area under the peak of a phase. Again, in the plots below, Area fraction -1 corresponds to the first phase or the phase with higher d-spacing and Area fraction -2 corresponds to the second phase or the phase with smaller d-spacing obtained from a binary liquid.

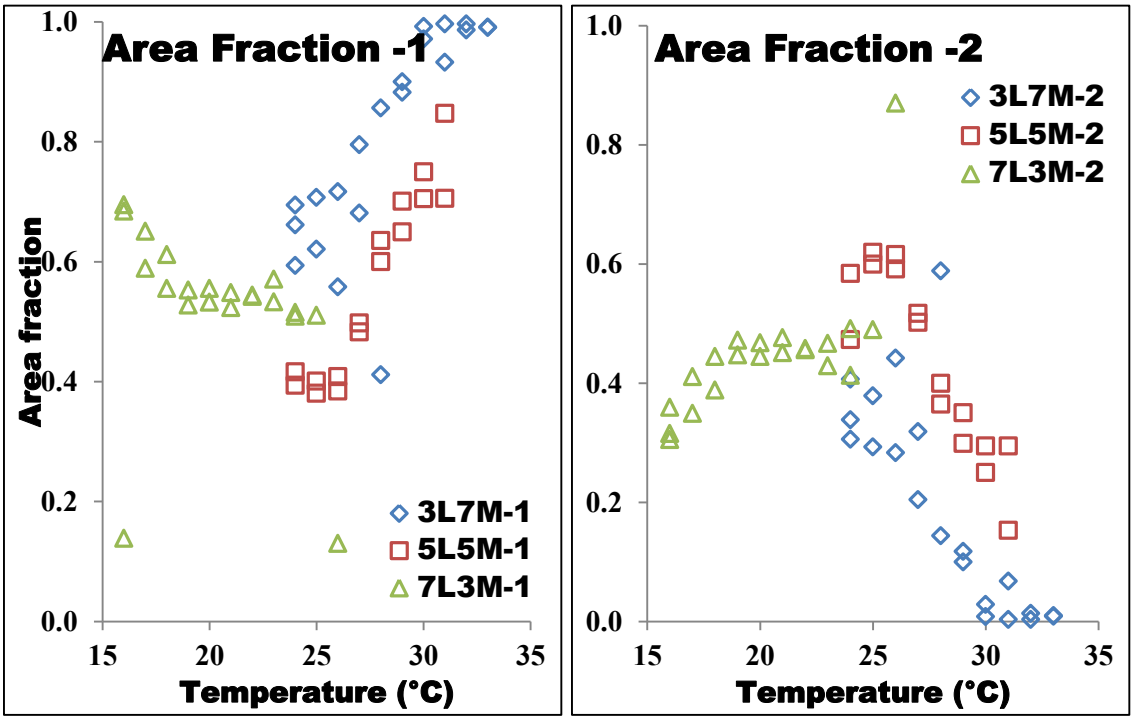

Figure 4-4. Area fraction of both crystalline phases at the end of an experiment plotted against crystallization temperature. The d-spacing of phase 1 is larger than the d-spacing of phase 2

Although the crystalline phases formed had very similar d-spacings at the end of crystallization, the area fraction of these crystalline phases changed with the crystallization temperature.

The crystalline phases formed do not have the same melting point due to the differences in their composition. Although the melting point depends on the composition of a phase, this relationship might not be monotonous (i.e either continously increasing ordecreasing with composition). The growth of both crystalline phases do not take place at equilibrium, rather they occur at a certain degree of undercooling. With undercooled conditions, the growth of a crystalline phase depends on the attachment/detachment tendencies of the two components in the system (Los & Flöter, 1999). The domination of a phase that has higher d-spacing (rich in trimyristin), consistently at higher temperatures (See Figure 4-5 and Figure 4-6) weakly points towards the increase in probability of attachment of trimyristin/trilaurin to a solid phase might not be linear with temperature.

Figure 4-5 and Figure 4-6 represents the area of each of the crystalline phase as a function of time.

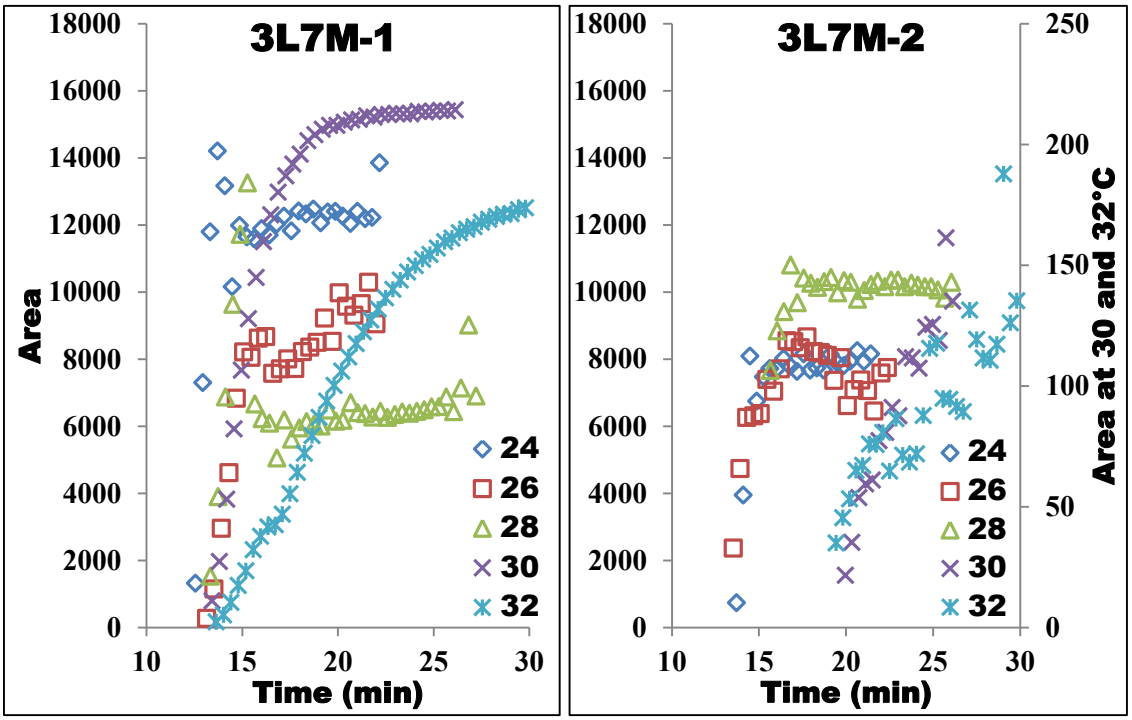

Figure 4-5. Area of crystalline phases formed from 3L7M as a function of time. The crystallization temperatures (°C) are shown in the legends.

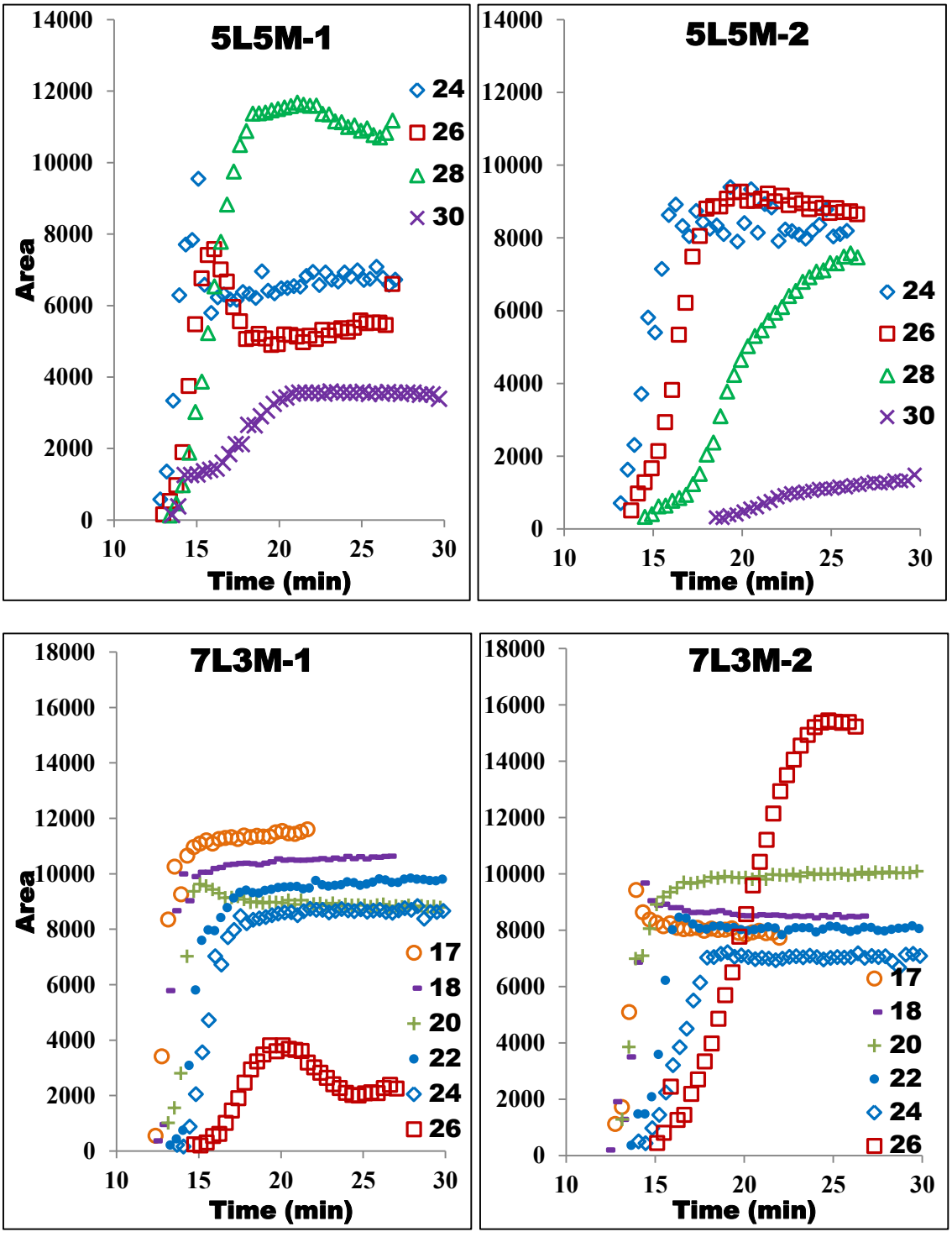

Figure 4-6. Area of crystalline phases formed from 5L5M and 7L3M as a function of time. The crystallization temperatures (°C) are shown in the legends.

The areas increase monotonously with time in many of the experiments, indicating a steady increase in the mass of a crystalline phase with time. However, in the case of 7L3M at 26°C, the trend in the areas of both the crystalline phases show a possible phase transformation. Sample 5L5M displayed a similar behavior at the lower crystallization temperatures. Phase-1 (higher d-spacing) had the largest area fraction at the beginning. After some time into the crystallization (about 2 minutes) phase-2 (smaller d-spacing) became larger, and part of phase-1 either melted or dissolved into existing liquid due to differences in supersaturation conditions. After that, phase-1 resumed growth as phase-2 decreased steadily. (For detailed explaination of this phenomenon see section 6.2).

4.4 Thickness of the crystalline nanoplatelets of the phases

The thickness of the crystalline nanoplatelets is calculated using Scherrer's approximation (Section 2.2.2.2). The thickness of each crystalline phase at the end of an experiment is plotted against the crystallization temperature for the three binary mixtures of trilaurin with trimyristin.

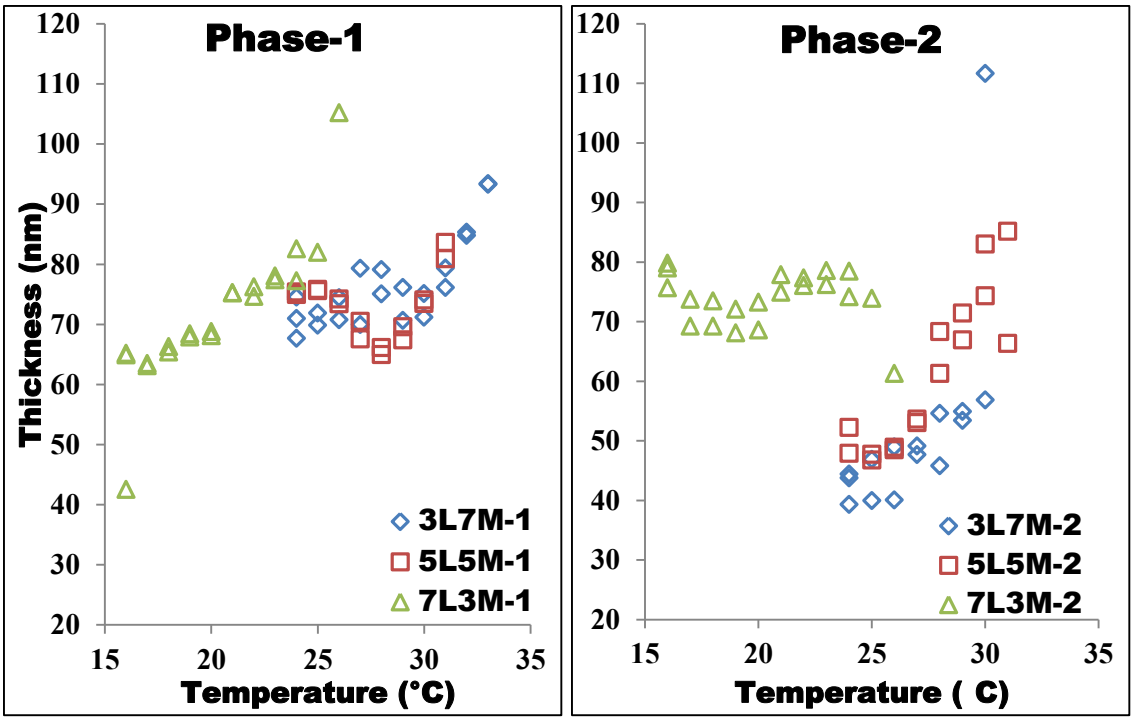

Figure 4-7. Thickness of the crystalline nanoplatelets that belong to both solid phases at the end of crystallization as a function of crystallization temperature for all three samples.

Figure 4-7 suggests the possibility of a physical limit beyond which TAG crystals tend not to grow. These observations match with the measured dimensions of individual crystals using Cryo-TEM by (Acevedo & Marangoni, 2010). Crystalline phases with higher thickness were obtained at relatively higher crystallization temperatures. This implies that phases with slower growth rate tend to grow to a higher thickness. This dependency of the thickness of a crystalline phase on the holding temperature might be due to the decrease in nucleation rates at lower degrees of undercooling, i.e at relatively higher holding temperatures (Marangoni & Wesdorp, 2012). In other words, at a lower degree of undercooling a crystalline phase grows at a much slower rate and at the same time evolves from a smaller number of nucleation sites.

The limit on the thickness of a crystalline phase suggest that the activation energy of attachment to a surface depends on the thickness of a the nanoplatelets i.e. forming a new growth surface becomes easier than attaching to an existing surface, as the thickness of the existing crystallite increases. BCF theory states that the defects on the surface of a crystal act as attachment sites at higher degree of undercooling (See section 2.1.3.1). As the defects in a crystal tend to increase with a decrease in the crystallization temperature

(see section 7.2), probably a higher number of attachment sites exist at lower temperatures, causing molecules to attach to these newer sites rather than existing surfaces. On the contary, at higher crystallization temperatures, the presence of lower nucleation sites as well as lower number of defects in the crystallites allows the liquid molecules to attach to an existing surface although it has a higher thickness.

Chapter 5 RELATIONSHIP BETWEEN THE D-SPACING AND COMPOSITION OF A CRYSTALLINE PHASE

The trilaurin-trimyristin crystalline phases occurred in pairs in most cases as seen in Figure 4-1. These nanocrystalline phases were uniformly mixed throughout the sample making it impossible to separate them from one another to measure their composition. This chapter describes a method to estimate the composition of these crystalline phases from their d-spacing.

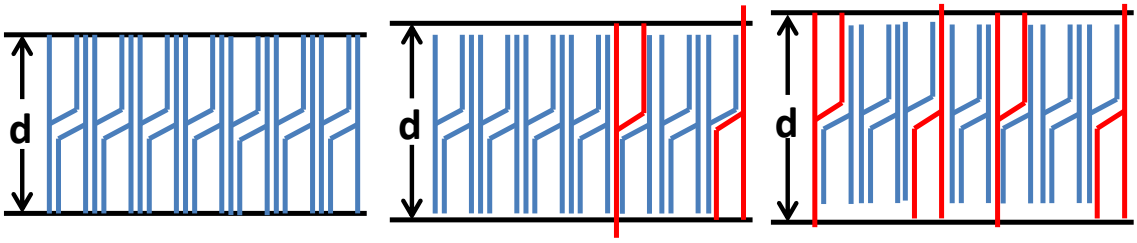

Figure 5-1.A schematic diagram showing an increase in the d-spacing due to the increase in concentration of a longer chain TAG in a two component crystalline phase

The d-spacing of a crystalline phase of a particular polymorph made up of two TAGs depends on its composition (Anom, 2009), though a clear mechanism for this dependency is not yet fully known. In our case, the polymorphic form of all the crystalline phases formed was β'.

Following the method by Anom (2009), an empirical relationship between the d-spacing and mass fraction of trilaurin in a phase was established through a mass balance. Experiments with completely crystalline solid were chosen to perform mass balance as the overall composition of the solids must be equal to that of the initial liquid material. The third crystalline phase that seldom occurred from the sample 3L7M at higher temperatures was not considered due to its very small mass compared to the other phase that is being formed.

5.1 Mass balance

A binary mixture that is completely crystallized into two crystalline phases must satisfy the mass balance:

$$m_s \cdot z = x_1 \cdot m_1 + x_2 \cdot m_2$$
$$m_s = m_1 + m_2 \quad (5\text{-}1)$$

Here,

m_s is mass of the sample

z is the overall mass fraction of trilaurin in the sample

x_1, x_2 are the mass fractions of trilaurin in the crystalline phases 1 and 2.

m_1, m_2 are the masses of each of the two crystalline phases formed.

The latter sections describe a way to express the composition of a phase in terms of its d-spacing and the mass of a phase in terms of its diffraction area.

5.1.1 The proportionality factor ψ

The ratio between the mass of a phase and the area under its XRD peak is a proportionality factor, expressed as:

$$\frac{m_1}{A_1} = \psi_1 \text{ and } \frac{m_2}{A_2} = \psi_2 \quad (5\text{-}2)$$

Here, A_1, A_2 are the areas under the XRD peaks of phases 1 and 2, and ψ_1, ψ_2 are the corresponding proportionality factors.

The method proposed by (Anom, 2009) used a linear relationship between the proportionality factor and the composition of a crystalline phase.

$$\psi = \delta \cdot x + c \quad (5\text{-}3)$$

For the relationship between the composition and d-spacing

$$x_L = f_1(d) \quad (5\text{-}4)$$

The proportionality factor (ψ) became,

$$\psi = f_2(f_1(d)) \quad (5\text{-}5)$$

Use of equation (5-5) in mass balance made computations quite unstable by forming a system of equationswith infinite solutions.

Thus, in this study, the proportionality factor (ψ) was instead expressed as a function of d-spacing.

For a particular polymorphic form,

$$\psi = f(d) \tag{5-6}$$

Since no information about this relationship is available, a quadratic relationship was chosen, to provide some flexibility to the relationship so that it can fit into a non-linear dataset.

$$\psi = a_2 \cdot d^2 + a_1 \cdot d + c \tag{5-7}$$

5.1.2 Use of mass fraction and area fraction for mass balance

The mass fraction of a phase was used instead of its mass, to eliminate the dependence on the amount of sample.

For a fully crystalline system with two crystalline phases (by neglecting the very minor third crystalline phase if present), the mass fractions of the phases are:

$$S_1 = \frac{m_1}{m_1 + m_2} \text{ and } S_2 = 1 - S_1 \tag{5-8}$$

Equation (5-1) can then be rewritten as:

$$\begin{aligned} z &= x_1 \cdot S_1 + x_2 \cdot S_2 \\ z &= x_1 \cdot S_1 + x_2 \cdot (1 - S_1) \end{aligned} \tag{5-9}$$

From (5-2)

$$S_1 = \frac{\psi_1 A_1}{\psi_1 A_1 + \psi_2 A_2} \tag{5-10}$$

Rearranging (5-10),

$$S_1 = \frac{1}{1 + \frac{\psi_2 A_2}{\psi_1 A_1}} \tag{5-11}$$

Reorganized to use the area fractions (5-11) becomes:

$$S_1 = \frac{1}{1 + \frac{\psi_2}{\psi_1} \cdot \frac{\sigma_2}{\sigma_1}} \text{ because } S_1 = \frac{1}{1 + \frac{\psi_2}{\psi_1} \cdot \frac{A_2 \big/ (A_1 + A_2)}{A_1 \big/ (A_1 + A_2)}} \tag{5-12}$$

External factors like the diameter of the capillary affect the amount of the sample exposed to the x-ray beam, thereby affecting the areas of the crystalline phases. Use of the area fraction of a phase (σ) instead cancels out the effect of external factors.

5.2 Relationship between d-spacing and composition

The relationship between the d-spacing and composition was expressed as:

$$x = x_d \cdot r_z \tag{5-13}$$

$$x_d = \frac{d_M - d}{d_M - d_L} \tag{5-14}$$

$$r_z = 1 + b_2(x_d - 1) + b_3(x_d^2 - 1) \tag{5-15}$$

Here,

x is the composition of trilaurin in the crystalline phase,

x_d is an ideal linear relationship between composition and d-spacing,

d is the d-spacing of a phase,

d_M and d_L are the extrapolated d-spacings of pure trilaurin and trimyristin phases,

r_Z is a correction factor for the deviation of the composition of a phase from linearity,

The form of r_z was chosen so that x_d would be anchored at 0 and 1 at $d = d_M$ and $d = d_L$, respectively.

5.2.1 Mass balance proportionality factor (ψ) and the modified proportionality factor (ψ')

The values of the parameters in equations (5-13), (5-14), and (5-15) estimated by (Anom, 2009) were used as initial guess values to calculate the compositions of crystalline phases in a completely crystalline system. A simple mass balance was performed using these compositions to calculate the mass fraction of each phase as shown in (5-16):

$$S_1 = \frac{z - x_2}{x_1 - x_2} \text{ and } S_2 = 1 - S_1 \tag{5-16}$$

A proportionality factor (ψ) for each phase was determined by dividing its phase fraction with the area of that phase at the corresponding time:

$$\psi_i = \frac{S_i}{A_i} \tag{5-17}$$

The proportionality factor (ψ) was normalized by dividing its equation over the constant term c. This modification does not affect the mass balance because "c" cancels out in the ratio of proportionality factors in equation (5-12)

$$\psi' = \frac{a_2}{c} d^2 + \frac{a_1}{c} d + 1 \tag{5-18}$$

$$S_1 = \frac{1}{1 + \frac{\psi'_2}{\psi'_1} \cdot \frac{\sigma_2}{\sigma_1}} \tag{5-19}$$

Initial guess values for the parameters in (5-18) were estimated by fitting a quadratic equation between mass balance proportionality factors and their corresponding d-spacings.

5.2.2 Estimating the parameters for the relationship between d-spacing and composition

For a completely crystalline system, the compositions and phase fractions of both the crystalline phases were calculated using as initial guess values of parameters estimated by (Anom, 2009) through equations (5-13), (5-14), (5-15) and the initial guess values of (5-18). The overall composition of trilaurin in the sample was calculated (z_{calc}) by the mass balance as shown in (5-9). To optimize the values of the parameters, sum of squares of the difference between the calculated overall composition of the sample and the actual overall composition was computed using (5-20):

$$\chi^2 = \sum_{k=1}^{n} [(z_{calc}) - (z)]^2 \tag{5-20}$$

Here, k represents the experiment number for which the sum of square of difference between the actual and calculated overall composition is estimated.

An Excel solver was set up using the GRG nonlinear method (Frontline Solvers, Incline Village, NV, US) to minimize χ^2 (5-20) by changing the six parameters of the equations (5-13), (5-14), (5-15) and (5-18). A convergence value of 0.00001 and a multi start method with a population size of 100 was used for the solver.

Constraints were applied to d_L and d_M based on practical limits, and to the compositions (0 to 1), to avoid unrealistic solutions.

Table 5-1. Parameters producing the minimum sum of squares of error value using 27 experiments.

Coefficient	Value
b_2	2.200
b_3	-1.611
d_L	3.067
d_M	3.810
a_2/c	0.08120
a_1/c	-0.56963

5.2.3 Incorporation of additional experimental data to support the developed correlation

Table 5-2 shows the number of experiments performed with each sample used in the estimation of parameters in Table 5-1.

Table 5-2. Number of completed experiments performed with each sample at the NSLS

Name of sample	# of experiments
3L7M	5
5L5M	6
7L3M	16

The small number of experiments with 3L7M and 5L5M biased the parameters in Table 5-1 towards the experiments with 7L3M. To improve the range of the data, an additional 68 SAXD experiments at various temperatures were then performed at our in-house XRD facility. The results were incorporated into the estimation of parameters listed in Table 5-1. At least two replicates of each crystallization experiment were performed. To ensure the absence of liquid, the analysis included only patterns acquired after the first 30 minutes. Experiments usually lasted two to three hours.

Table 5-3. SAXD experiments at the in-house XRD setup

Name of sample	**# of experiments**
3L7M	23
5L5M	25
7L3M	20

Some experiments with 3L7M at the in-house XRD setup showed three crystalline phases instead of the two crystalline phases as shown from their corresponding experiments conducted at NSLS. This phenomenon could be explained by partial phase transformation of one of the crystalline phases when kept for a longer time. Corresponding WAXD experiments could not be performed due to limitations in time and the experimental setup. The third phase obtained was also treated as a β' polymorph as its d-spacing is close to the d-spacing of one of the phases obtained from 5L5M.

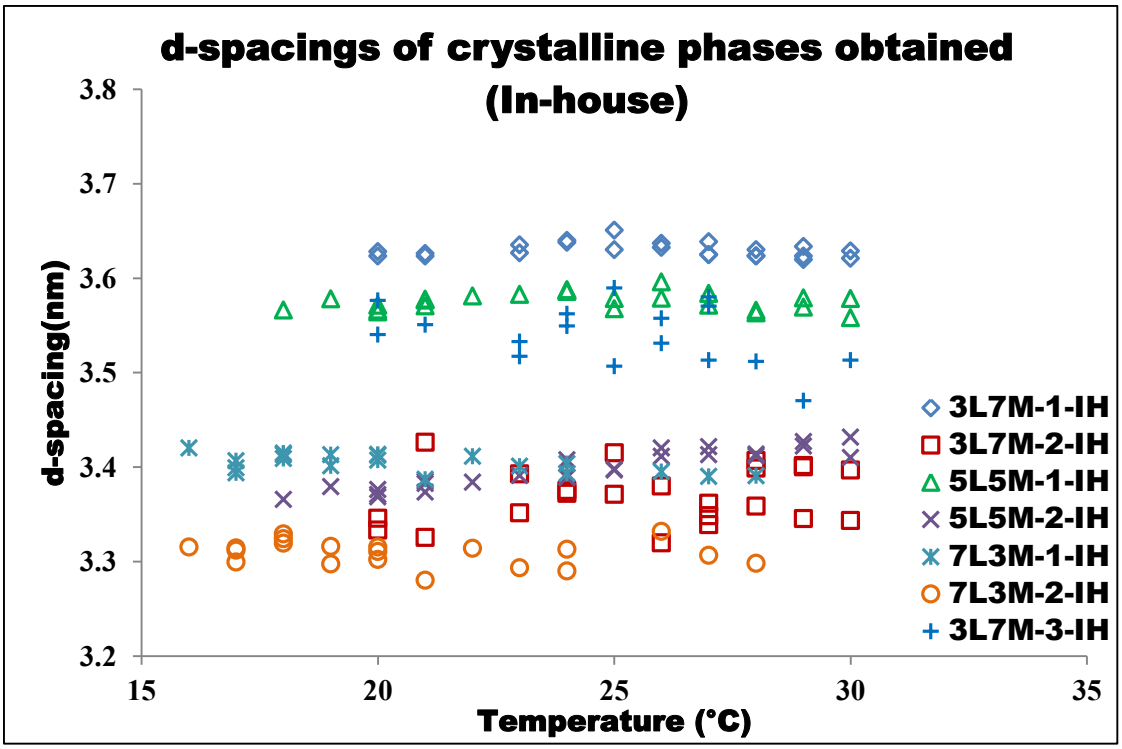

Figure 5-2. d-spacings of the crystalline phases formed at different temperatures during the experiments performed with in-house XRD setup.

For a system with two crystalline phases, the calculation of overall composition was performed in the same way as described in section 5.1. For a system with three crystalline phases,

$$m \cdot z = x_1 \cdot m_1 + x_2 \cdot m_2 + x_3 \cdot m_3 \tag{5-21}$$

A generalization of (5-10) for a system of n phases is:

$$S_i = \frac{A_i \cdot \psi_i}{\sum_{i=1}^{n} A_i \cdot \psi_i} \tag{5-22}$$

As described in section 5.1.2, A_i can be replaced by σ_i and ψ_i can be replaced by ψ_i',

And also $\sum_{i=1}^{n} A_i \cdot \psi_i = m$ (5-23)

As a result, the calculated ovearll composition of sample (z_{calc}) of three phase system can be expressed as:

$$z_{calc} = \frac{x_1 \cdot \psi'_1 \cdot \sigma_1 + x_2 \cdot \psi'_2 \cdot \sigma_2 + x_3 \cdot \psi'_3 \cdot \sigma_3}{\psi'_1 \cdot \sigma_1 + \psi'_2 \cdot \sigma_2 + \psi'_3 \cdot \sigma_3} \quad (5\text{-}24)$$

Equation (5-24) was used for the calculation of overall composition of the sample in the case of a system that is crystallized into three phases using the set of parameters shown in Table 5-1.

A new total sum of square of errors ($\chi 2$) between the actual and the calculated composition of liquid was estimated. Again, the Excel solver is initialized to reduce this $\chi 2$ by changing the set of six parameters shown in Table 5-1.

The quadratic relationship of ψ' is very sensitive to its parameters, change in its fifth decimal produces a curve between proportionality factor and d-spacing that is visually different causing differences in the phase fraction calculated, as a result more number of decimal places were reported.

Table 5-4. New parameter values after the incorporation of in-house experimental data

Coefficient	**Value**
b_2	2.200
b_3	-1.604
d_L	3.100
d_M	3.800
a2/c	0.08024
a1/c	-0.56624

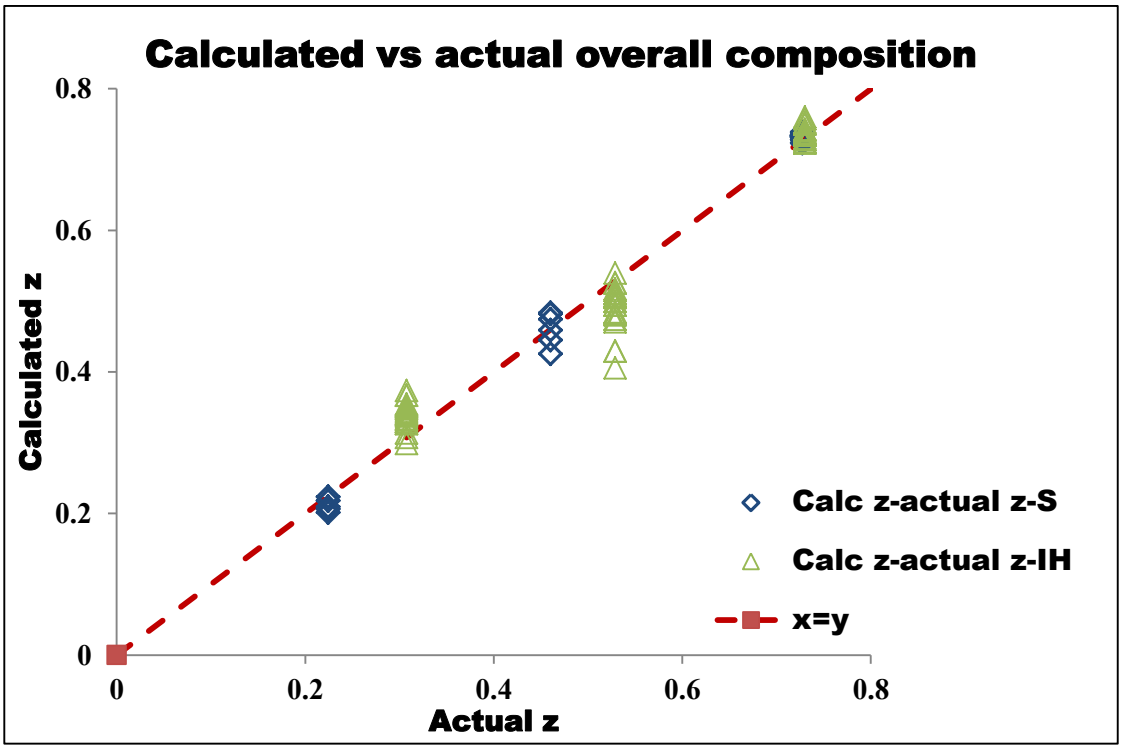

Figure 5-3. Calculated and actual overall trilaurin composition in the sample. The data series ending with an 'S' and 'IH' represent the data points obtained from the experiments performed at the synchrotron and at the in-house facility respectively.

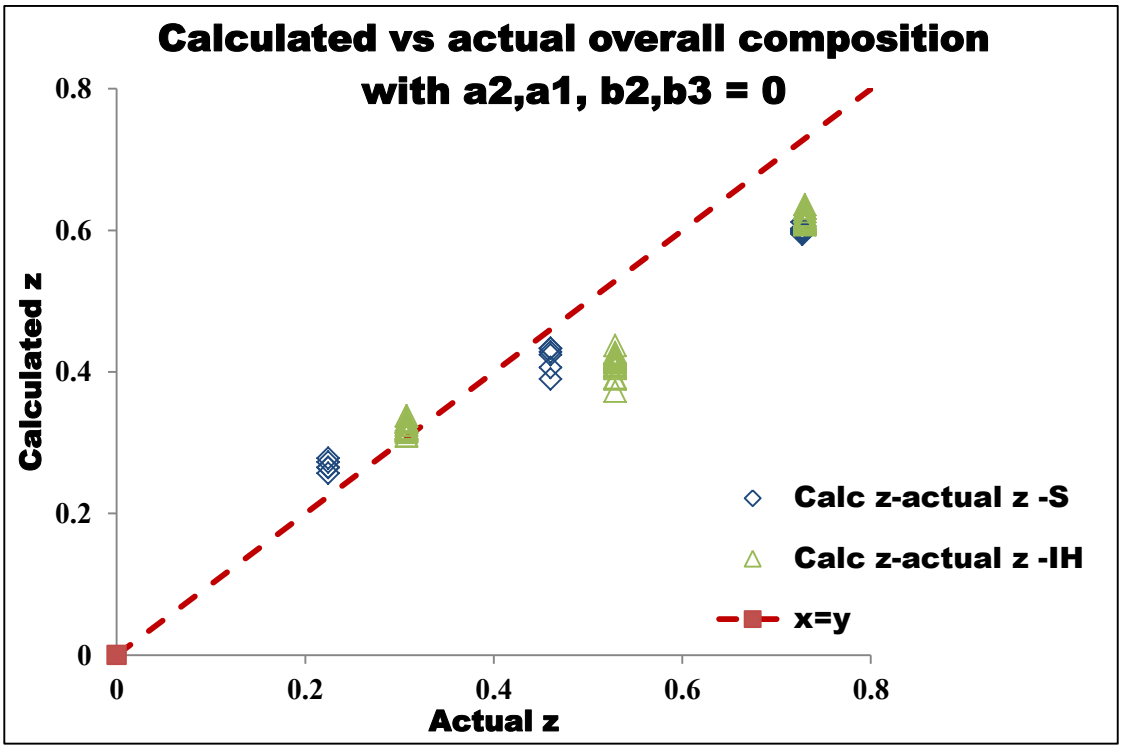

Figure 5-4. calculated and actual overall composition of trilaurin in the sample without using the correlation between d-spacing and composition and assuming no proportionality factor between area fraction and mass fraction of a crystalline phase

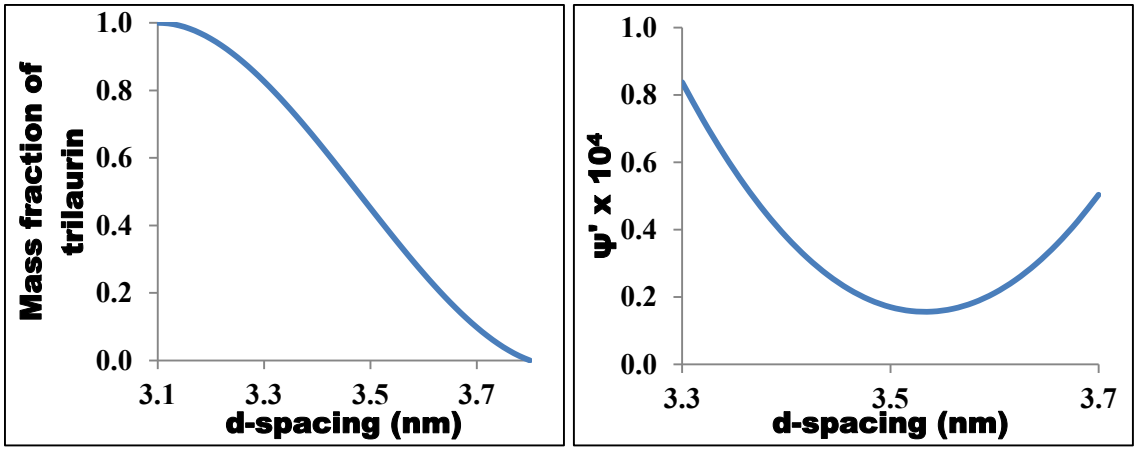

Figure 5-5. Relationship between the composition and d-spacing, modified proportionality factor(ψ') and d-spacing of a phase using the set of parameters described in Table 5-4

The non-linearity in the relationship between the d-spacing and the composition of a crystalline phase might be probably due to slight changes in their sub-cell packings (see Figure 7-2). Crystalline phases formed from liquid with higher composition of

trilaurin tend to have a better arrangement than crystalline phases rich in trimyristin (see Section 7.1.2). These differences might have an influence on the order of the molecules in the longitudinal direction, causing the relationship between d-spacing and composition to deviate from linearity.

The high curvature of the quadratic relationship between the proportionality factor and d-spacing of a phase is surprising. A crystalline phase that has a d-spacing of about 3.55 nm (phase with a composition of about 0.4 mass fraction of trilaurin) would diffract x-rays about 4 times when compared to a crystalline phase made up of a phase that has a d-spacing of 3.3 nm and has the same mass. The proportionality factor was not plotted for the whole range of d-spacings that correspond to pure tilaurin and pure trimyristin as the extrapolated correlation beyond the d-spacings of crystalline phases obtained experimentally will be prone to a high degree of uncertainity due to lack of data points. As diffraction patterns result from the constructive interference of elastic scattering of x-rays from the electron cloud of atoms/molecules arranged in a repetititive fashion, a smaller proportionality factor for mixed crystalline phases is an indication of the arrangement of molecules reenforcing constructive interference of x-rays projected into the crystalline phase. Speculations about this phenomenon cannot be made as the arrangement of molecules in mixed phases is still unclear.

Additionally, the temperature of the system affects the sub-cell packing in a crystalline phase (See 7.1). Although not pronounced, this can still cause differences in the packing of molecules in longitudinal direction.

The deviations in the calculated and actual overall composition of the material shown in Figure 5-3 could also be due to natural randomness in the system: differences in the distribution of crystal clusters in the capillary as well as variations in the growth of these crystalline phases.

5.3 Monte Carlo analysis to estimate the confidence intervals of the parameters

According to (Wentzell, 2014) uncertainties in experimental data in the case of systems like XRD measurements were mainly due to Background noise, Shot noise, proportional noise and drift nosie.

For multiple variables measured simultaneously, the measurement error in each variable is often related to the error in the other variables. Error covariance and correlation matrices quantify the relationship between the errors.

5.3.1 Estimation of an error covariance matrix:

The error covariance and correlation matrices between the two d-spacings and the area fraction (σ) of the first phase are shown in Table 5-5 and Table 5-6 for a system made up of two crystalline phases. Area fraction was used instead of the absolute area as they change by a common scaling factor for both phases.

Table 5-5. Error covariance matrix between the three experimental variables measured

	d1 (nm)	d2 (nm)	σ
d1 (nm)	9.62E-08	1.02E-07	5.50E-06
d2 (nm)	1.02E-07	2.12E-07	1.10E-05
σ	5.50E-06	1.10E-05	2.01E-03

Table 5-6. Error correlation matrix between the three experimental variables measured

	d1 (nm)	d2 (nm)	σ
d1 (nm)	1	0.710	0.396
d2 (nm)	0.710	1	0.532
σ	0.396	0.532	1

The parameters d1 and d2 in Table 5-5 and Table 5-6 correspond to the d-spacings of first and second crystalline phases and σ correspond to the area fraction of the first phase, for d1 > d2.

Table 5-6 demonstrates a strong dependency between the errors of both the d-spacings and a weak relationship between the errors of d-spacing and area fraction of the first crystalline phase. Most of the statistical procedures like that are usually followed for the generation of correlated random variables like Cholesky decomposition, Eigen vector

decomposition etc., rely on a linear correlation between experimental variables when an generated uncorrelated dataset was converted into a correlated dataset using covariance and correlation matrices shown in Table 5-5 and Table 5-6. The correlation between the experimental variables is highly non-linear, as a result these existing statistical methods cannot be used to generate a set of correlated random variables that are correlated in the same way as the experimental dataset. The following sections describe the correlation between these experimental variables and the method to generate a random set of correlated variables to perform a Monte Carlo analysis.

5.3.2 Correlation between experimental variables

5.3.2.1 Relationship between the d-spacings of the two crystalline phases

The d-spacings of the crystalline phases obtained in pairs bear a strong relationship, as seen in Figure 4.1 and Figure 5-2. The relationship can be loosely described by a cubic polynomial as shown in Figure 5-6. Despite being strongly correlated (also as shown in Table 5-6 a level of pure variability still exists in the second d-spacing irrespective of the first d-spacing. This pure variability is estimated by calculating a standard deviation between experimental, d-spacing of the second phase and a calculated d-spacing of second phase using the correlation in Figure 5-6. The standard deviation was found to be 0.024 nm.

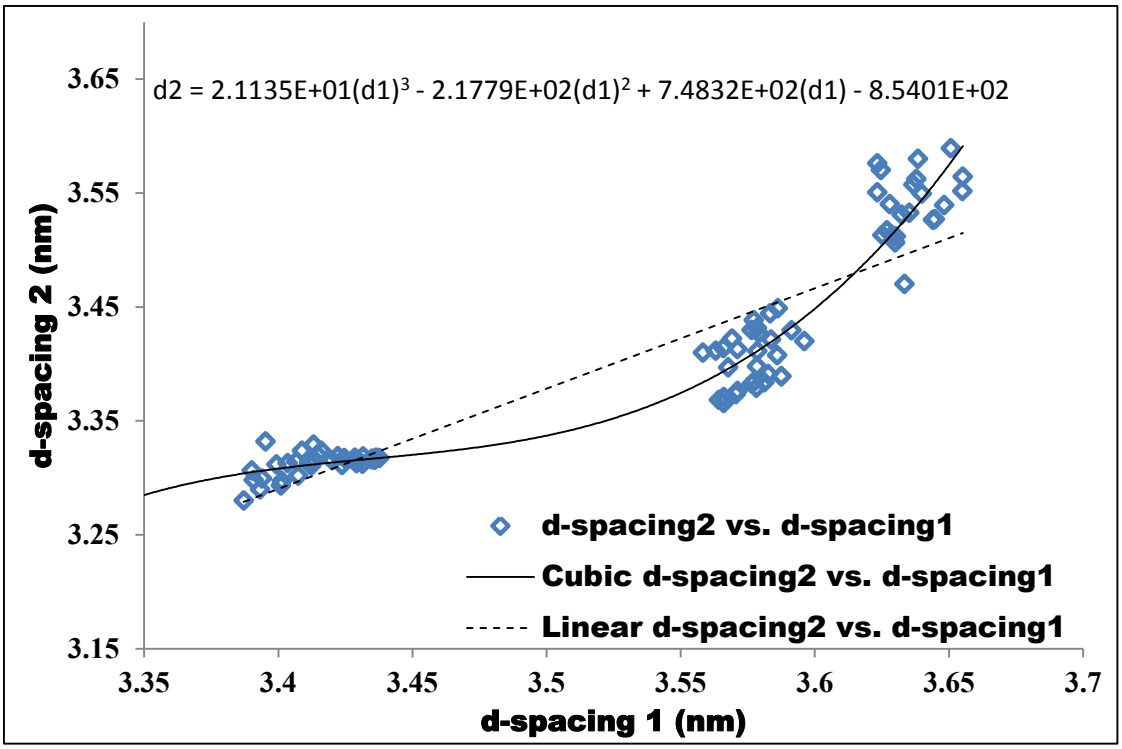

Figure 5-6. d-spacing2 as a function of d-spacing1

5.3.2.2 The relationship between the d-spacing and area fraction of the first phase

Figure 5-7 also shows no apparent relationship between the d-spacing of the first crystalline phase and its area fraction in agreement with Table 5-6.A theoretical value of area fraction 1($\sigma_{1,calc}$) is estimated using the d-spacing of first phase and calculated d-spacing of second phase as shown in equations (5-25) and (5-26). The corresponding compositions and proportionality factors for both these d-spacings were calculated using the set of parameters in Table 5-4.

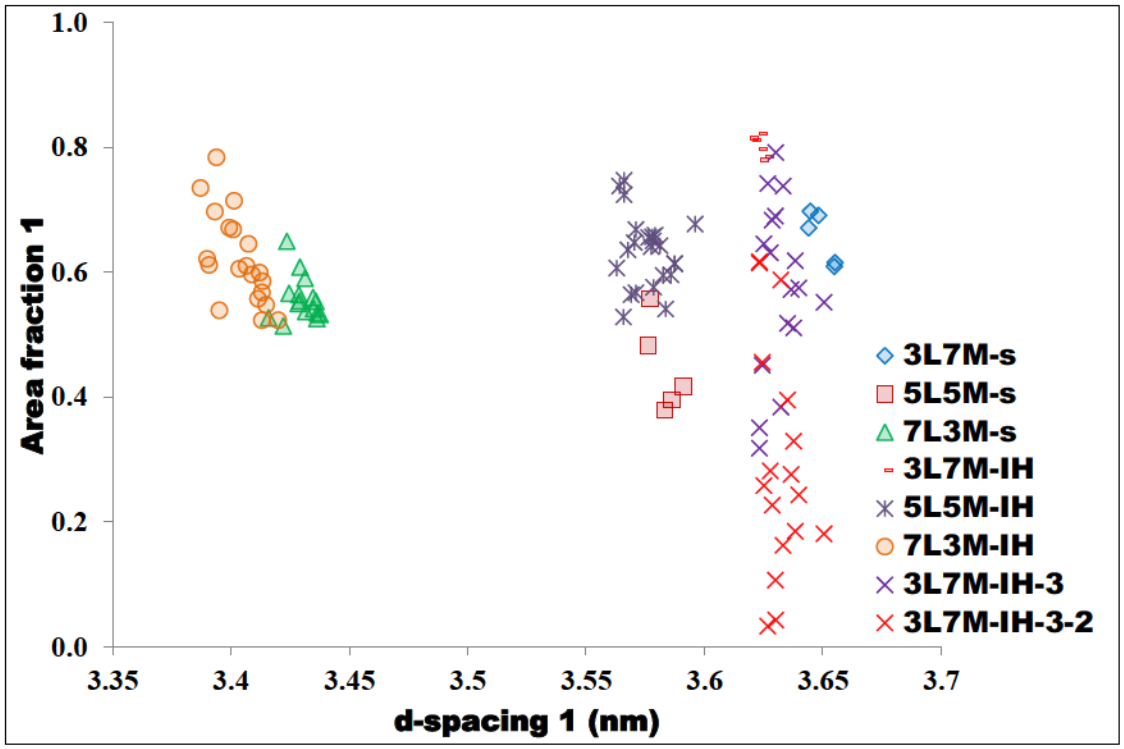

Figure 5-7.The area fraction of the first crystalline phase as a function of its d-spacing. The set of data series with a 's' at the end belong to the experiments conducted at the synchrotron and the data series ending with a 'IH' refer to the experiments conducted at the in-house XRD facility. The data series 3L7M-IH-3 and 3L7M-IH-3-2 refer to the area fraction of the first and second crystalline phases that belong to the set of experiments that had three crystalline phases

Calculating the area fraction (σ_1) of first phase:

(5-12) can be re-written as:

$$S_1 = \frac{1}{1 + \frac{(1-\sigma_1)}{\sigma_1}\frac{\psi_2}{\psi_1}} \tag{5-25}$$

Solving (5-25) and (5-16) for σ_1 yields:

$$\sigma_1 = \frac{1}{1 + \frac{\psi_1}{\psi_2}\left(\frac{z - x_1}{x_2 - z}\right)} \tag{5-26}$$

The calculated area fraction of phase 1 was plotted against the d-spacing of crystalline phase1 along with the actual area fractions that are obtained experimentally in Figure 5-8.

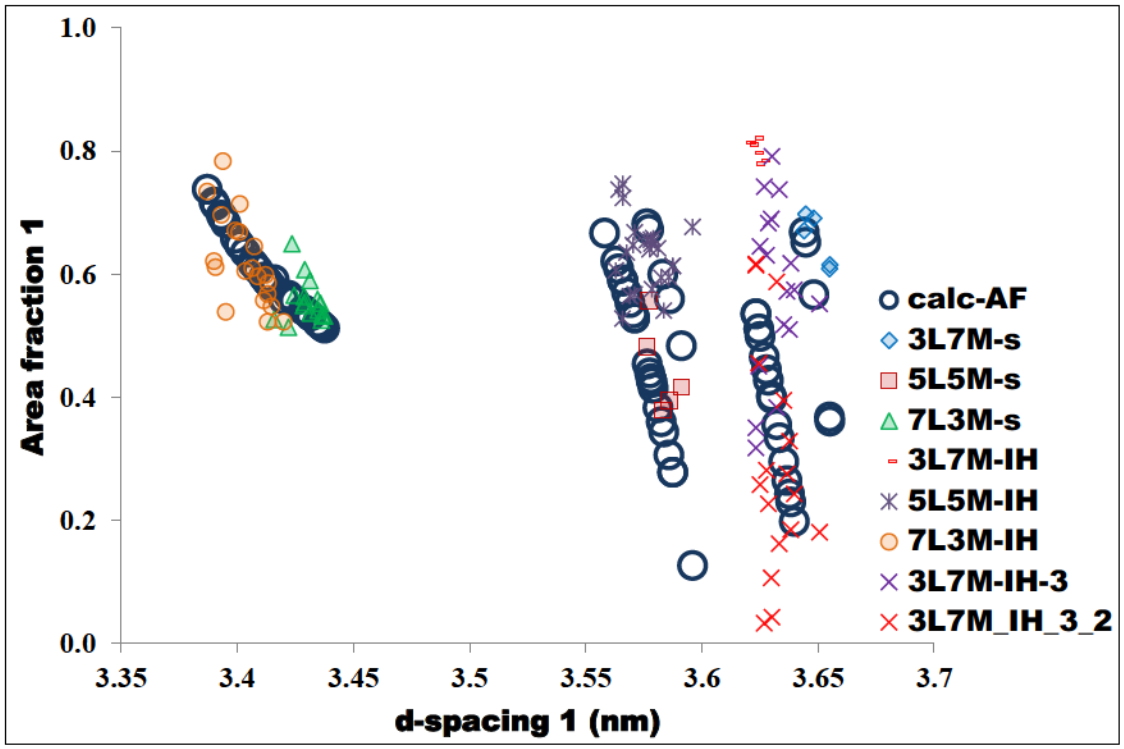

Figure 5-8. Experimental and calculated area fraction (calc-AF) of the first crystalline phase plotted as a function of its d-spacing.

Figure 5-8 indicates that the calculated area fraction of crystalline phase 1 is not very different from the experimental area fractions of phase 1. The standard deviation between the measured and calculated area fractions is found to be 0.177.

Table 5-7. Standard deviations between the calculated and experimental values

	Standard deviation(σ)
d-spacing-2 (nm)	0.024
Area fraction -1	0.177

5.3.3 Generation of correlated random variables to perform a Monte Carlo simulation

A set of d-spacings of the second phase were calculated from the first phase using the cubic relationship shown in Figure 5-6. A data set consisting of 1000 points for each calculated d-spacing of the second phase were generated using the standard deviation

between measured between the actual and calculated d-spacing of second crystalline phase as shown Table 5-7 by the procedure described in Section 3.8.2.

A binary liquid splitting into two crystalline phases should have one phase with a lesser concentration of a component and the other phase should have a higher concentration of this component compared to the concentration in liquid to satisfy mass balance. Thus, equivalent d-spacings of liquid composition were back calculated from the developed correlation between d-spacing and composition to be set as the upper limit for the generated d-spacings of the second phase.

Table 5-8. Measured liquid compositions and their equivalent d-spacings back calculated from the correlation between d-spacing and composition

	Sample ID	**z**	**Equivalent d-spacing (nm)**
Synchrotron	3L7M	0.2244	3.6261
	5L5M	0.4603	3.5000
	7L3M	0.7276	3.3601
In-house	3L7M	0.3077	3.5793
	5L5M	0.5288	3.4650
	7L3M	0.7301	3.3587

Area fractions of the first crystalline phase were calculated by using the experimental d-spacing of the first crystalline phase, the randomly generated d-spacing of the second crystalline phase and equation (5-26). These calculated area fractions were randomized within the standard deviation in Table 5-7.

5.3.4 Monte Carlo analysis to estimate the confidence intervals for the parameters

An Excel macro described in Appendix E was written to perform a Monte Carlo simulation using the random dataset generated. This Macro was programmed to perform 1000 iterations as the random dataset generated has 1000 data points for each original experimental variable. For each iteration, this Excel macro copied one set of the random data into the cells of their corresponding original data set, and used Excel solver to

calculate the parameters in Table 5-4. This Macro then saved the parameters into another tab and then moved to the next iteration. The confidence intervals of the six original parameters were calculated from the corresponding values of each parameter obtained as a result of analyzing each of the generated random datasets.

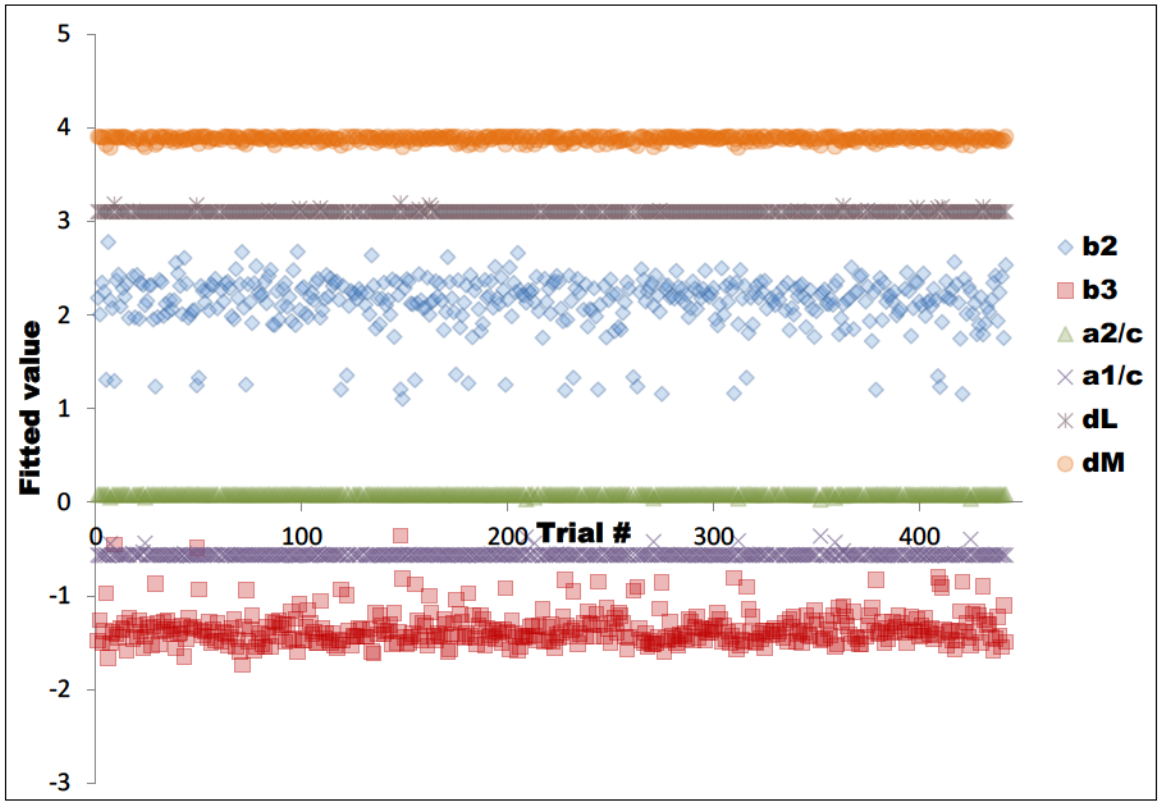

Figure 5-9. Values of the parameters obtained from each random data set.

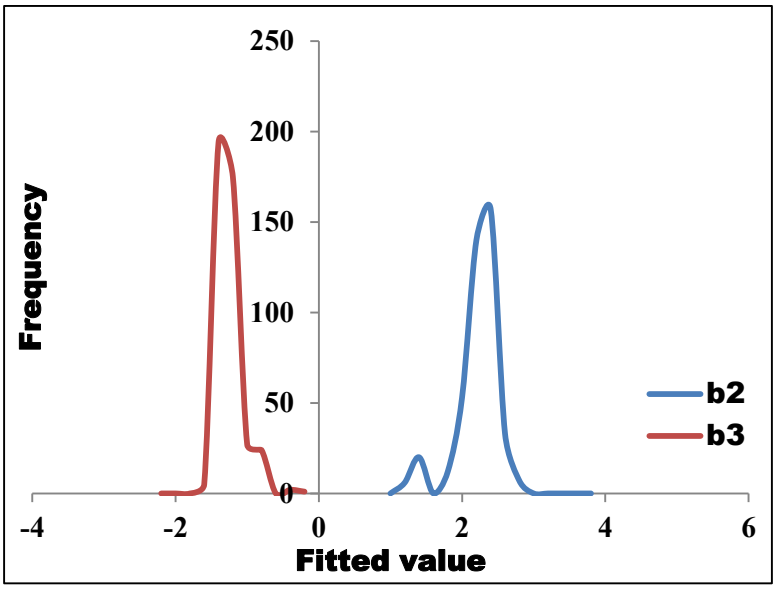

Figure 5-10. Distribution of the parameters b2 and b3 obtained by fitting various sets of generated random datasets

The four parameters a_2/c, a_1/c, d_L and d_M changed very little between trials, while the parameters b_2 and b_3 showed more variation. Table 5-9 shows the calculated mean value and estimated 95% confidence interval of the six parameters obtained from separate trials. The confidence intervals were calculated by estimating the standard deviation of the fitted parameters from each trial.

Surprisingly, few of the random datasets (~10%) generated tend to have another set of six parameters a_2/c, a_1/c, b_2, b_3, d_L and d_M that are very distinct from the set of parameters reported in Table 5-4 and produce a minimum square of error between the calculated and actual composition of trilaurin in liquid. This other solution might be just a mathematical solution and does not represent reality as it is far away from the solution produced by the original dataset. The occurances of this solution were removed in the calculation of confidence intervals of the set of parameters reported in Table 5-9.

Table 5-9. Parameters for the relationships between d-spacing and composition, and between area and mass fraction.

Parameter	Mean value	95% confidence interval
b_2	2.131	0.56
b_3	-1.354	0.35
d_L	3.102	0.02
d_M	3.879	0.05
a_2/c	0.07920	0.012
a_1/c	-0.56232	0.044

The mean values reported in Table 5-9 are very close to the set of estimates obtained from the original dataset shown in Table 5-4. Appreciable difference was observed in the value of d_M. Although the set of parameters that belong to the alternative solution were not included in the calculation of mean value reported in Table 5-9 there are still some discrepancies in the mean values probably due to the presence of another minor solution that is responsible for causing smaller humps in the frequency plot shown in Figure 5-10.

5.4 Calculation of capillary correction factor and the constant term in the equation

The actual phase fractions of both the solid phases were needed in order to calculate the amount and composition of the liquid phase at any point during crystallization. This could only be computed when the actual proportionality factor along with the constant term 'c' in equation (5-7) is known.

The phase fractions were calculated at the end of crystallization from the equation (5-16) and the proportionality factors were estimated using (5-17). These "mass balance proportionality factors" (ψ) of each phase were plotted against its d-spacing to estimate the constant term 'c' in equation (5-7).

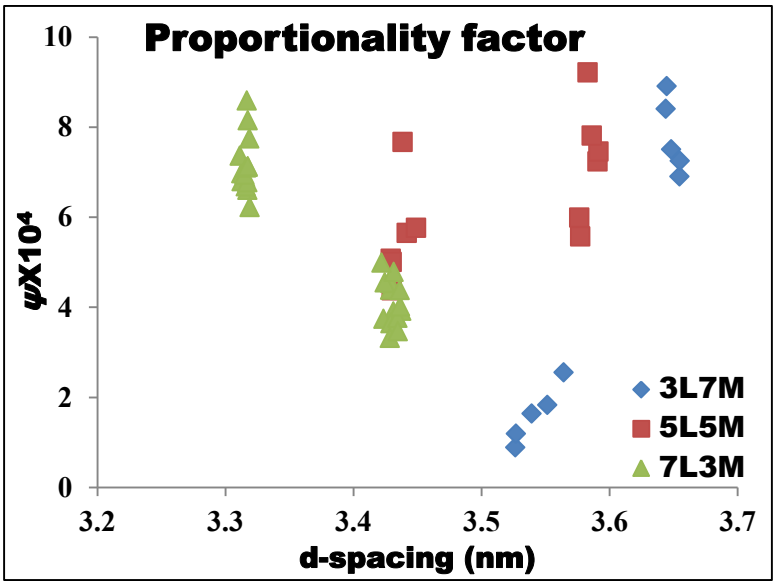

Figure 5-11. Plot of proportionality factors of phases estimated through mass balance after complete crystallization as a function of their corresponding d-spacings

These proportionality factors should follow the trend that is described by equation (5-18) as the only difference between the proportionality factor (ψ) and modified proportionality factor (ψ') is a scaling factor or the constant term 'c' in equation (5-7). The reason of the deviation from the correlation is mainly due to external factors like size of the sample capillary, position of the capillary in the capillary cell and glass thickness of a capillary.

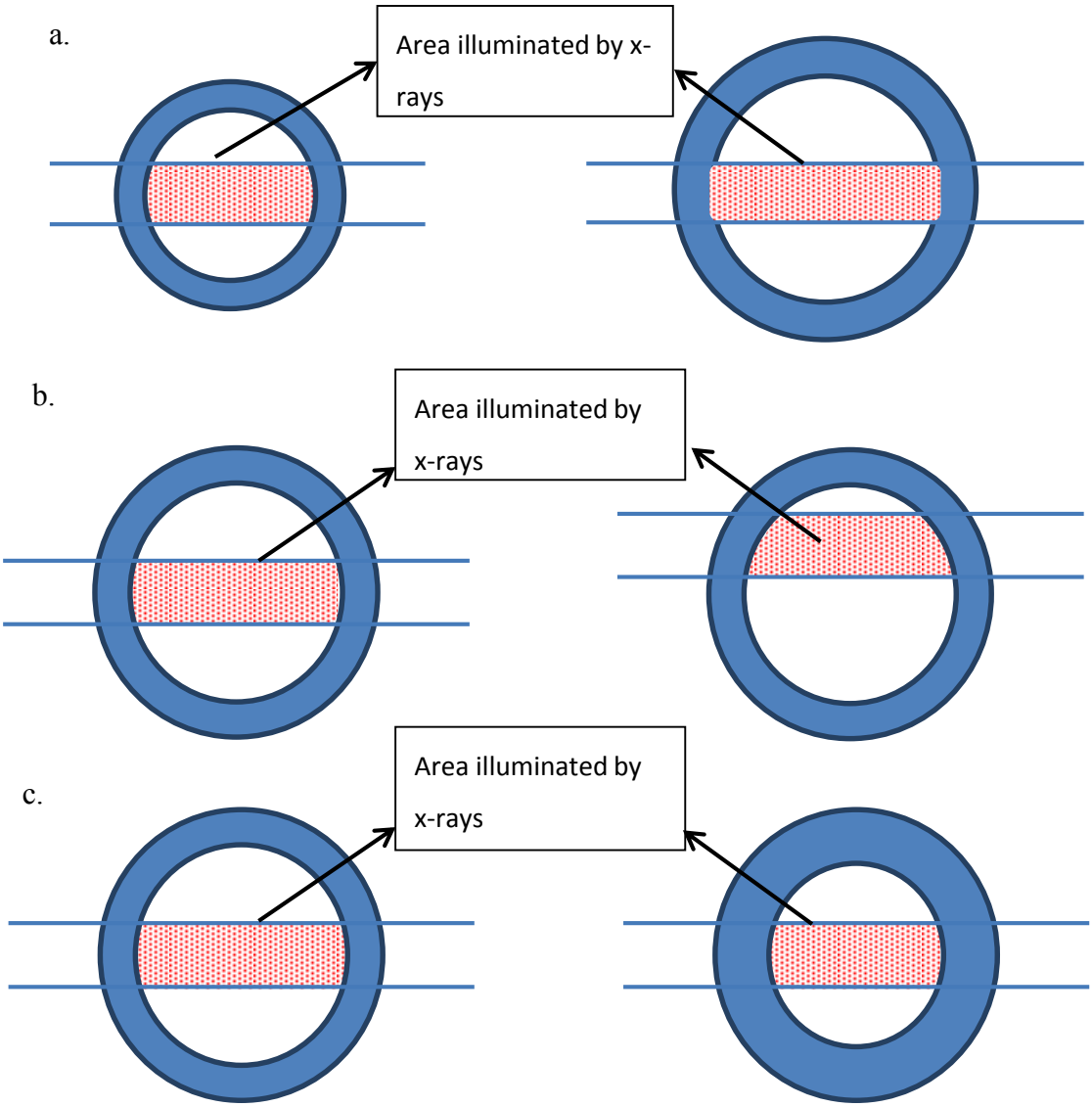

Figure 5-12. Differences in the area illuminated by x-rays due to the difference in (a.) Diameter of the sample capillary, (b.) Position of the capillary in x-ray beam's path and (c.) Wall thickness of the capillary.

A correction factor was estimated for each capillary to compensate for the external factors described in Figure 5-12. Initial values of theoretically estimated proportionality factors are calculated through equation (5-18) by using a value of '1' for the constant term 'c' in (5-7). The mass balance proportionality factors were calculated by using an initial capillary correction factor of 0.3 for 3L7M and 5L5M. The sample capillary 7L3M is considered as a reference and hence no correction is applied. Excel solver was set up using the GRG nonlinear method to minimize this sum of differences

calculated by changing the initial guess values for 'c' and capillary correction factors (Table 5-10).

Table 5-10. Scaling factor and correction factors estimated by the Excel solver method

Factor	Estimate
'c'	0.0156
Correction-3L7M	0.433
Correction-5L5M	0.337
Correction-7L3M	1

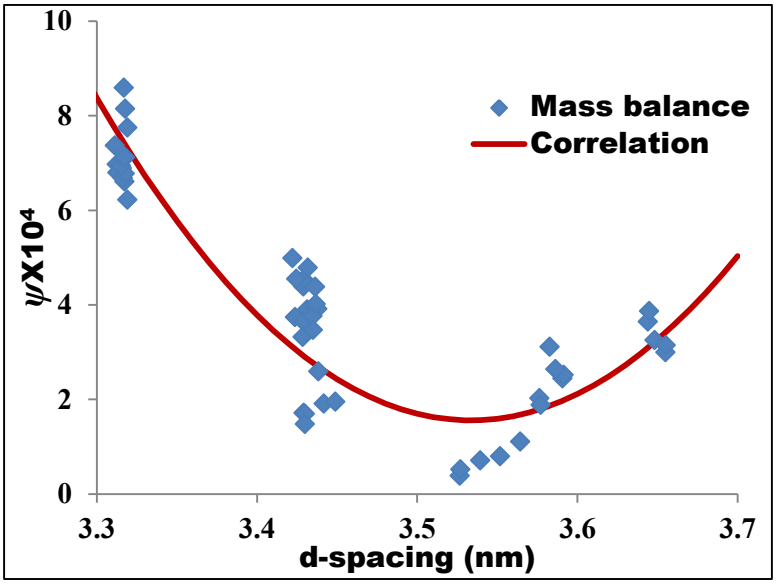

Figure 5-13. Proportionality factors estimated through mass balance and also through empirical correlation after the application of capillary correction factors.

Figure 5-13 shows that the theoretical proportionality factors and mass balance proportionality factors have some disagreement. A possible reason for disagreement is the formation of air pockets in the sample. As a result, a slight manual adjustment of the capillary correction factor was made during the calculations of phase fractions by comparing them to the corresponding phase fraction formed during a replicate experiment or an adjacent temperature.

Chapter 6 ESTIMATION OF THERMODYNAMIC AND KINETIC PARAMETERS FOR THE KINETIC PHASE DIAGRAMS

6.1 Calculation of compositions and the solid phase fractions

At each time during crystallization, the mole fraction of trilaurin in a crystalline phase was calculated using the correlation between d-spacing and composition developed in Chapter 5. The increase in the trilaurin composition in a phase with time was consistent with the stated hypothesis in Chapter 4. See Figure 6-1 and Figure 6-2. A possible reason for this trend is due to trilaurin molecules having a relativeley higher tendency to attach to a solid than trilaurin at any given temperature. Although the experiments were performed in replicates every 1°C, all of these experiments were not shown to make the plots less populated and for clear visualization of each trend.

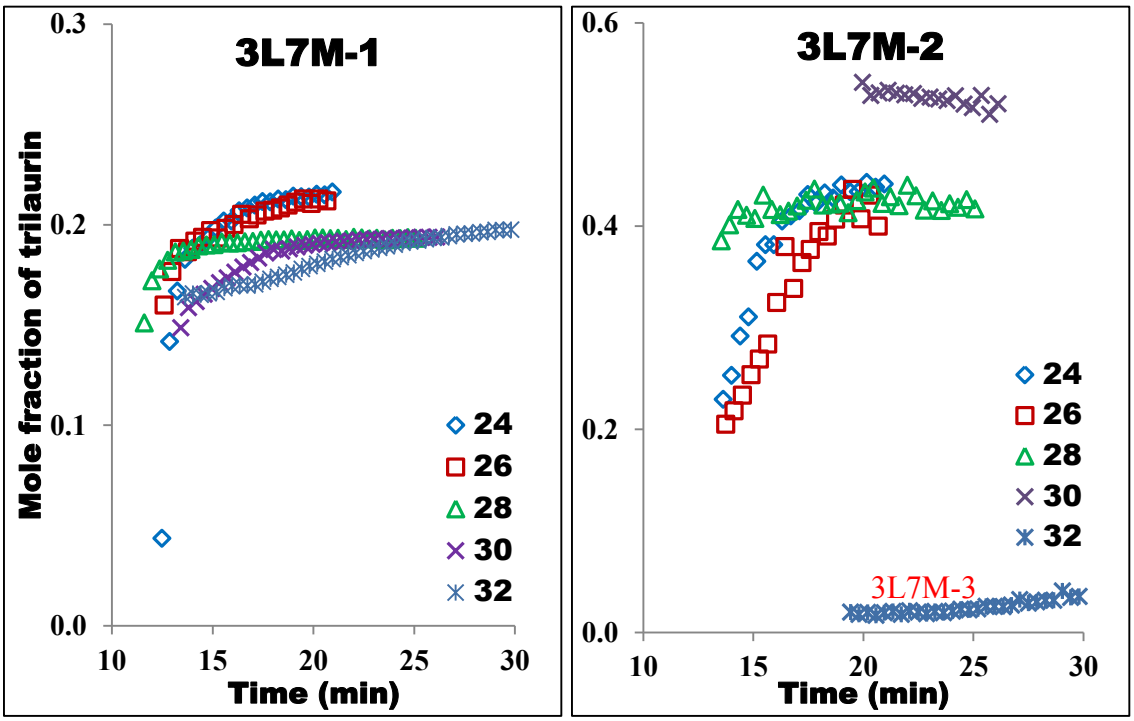

Figure 6-1. Mole fraction of trilaurin in both phases crystallized from 3L7M as a function of time. Legend shows the crystallization temperature in °C.

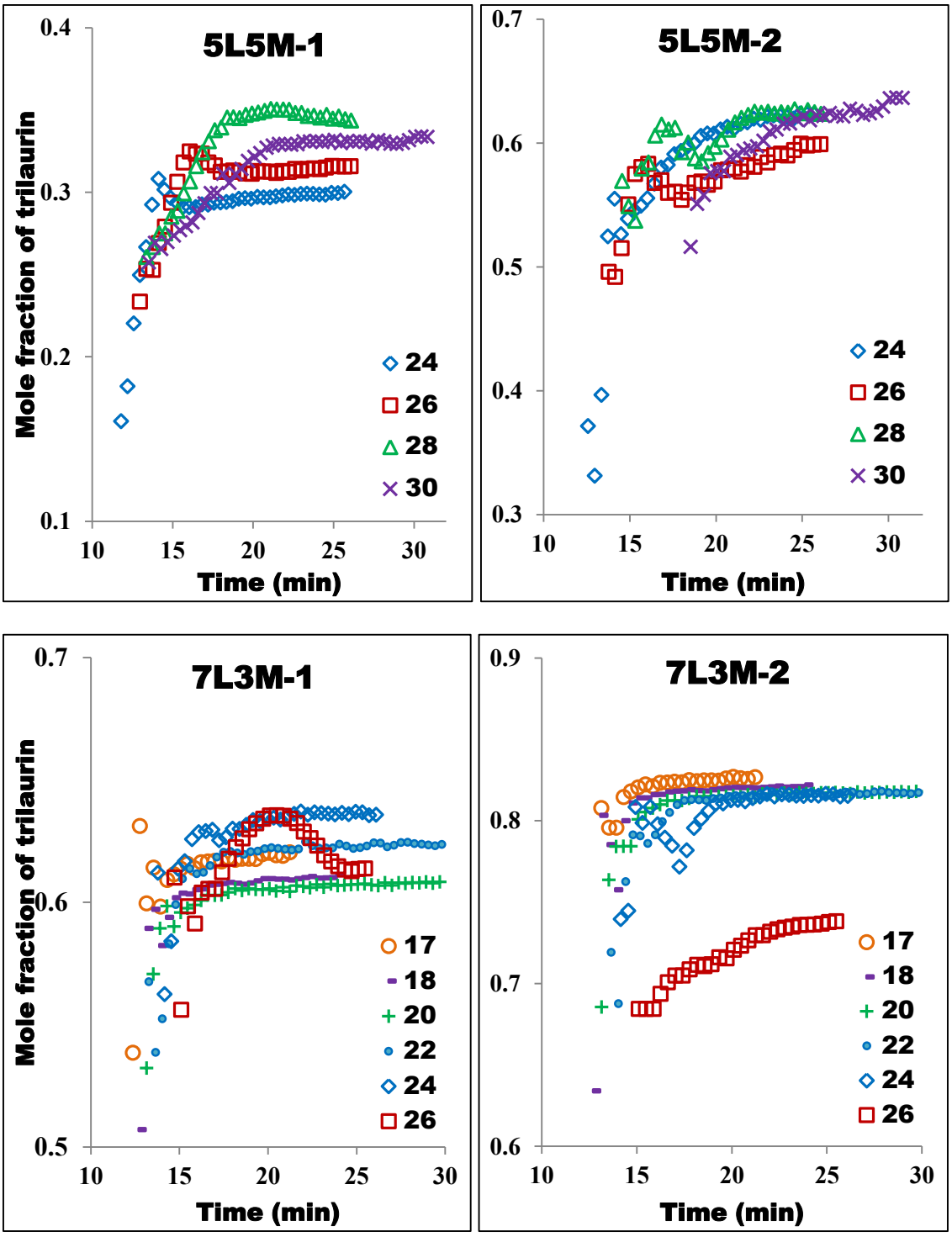

Figure 6-2. Mole fraction of trilaurin in the phases crystallized from 5L5M and 7L3M as a function of time. Legend shows the crystallization temperature in °C. Title indicates the sample name and phase number.

6.2 Calculation of solid fraction of a particular phase

The solid fraction(phase fraction) of a phase at any time during the crystallization process was estimated by multiplying its area by the proportionality factor (ψ) and the capillary correction factor as described in Section 5.4.

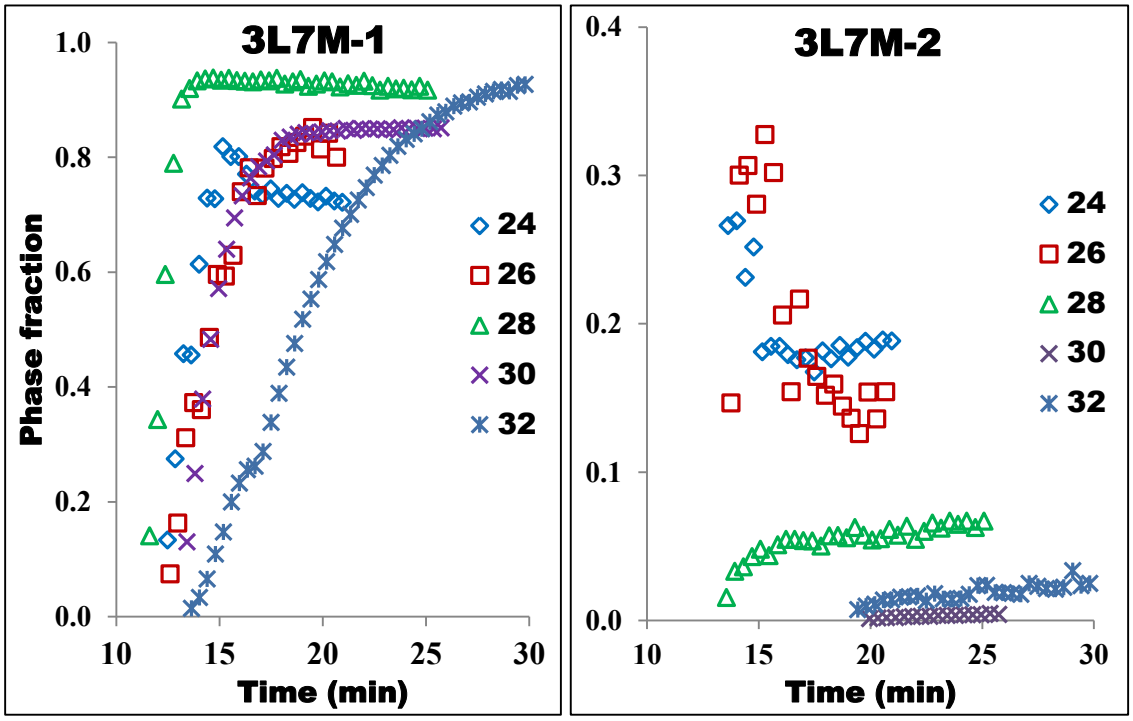

Figure 6-3. Phase fraction of the phases crystallized from 3L7M as a function of time. Legend shows the crystallization temperature in °C. Title indicates the sample name and phase number.

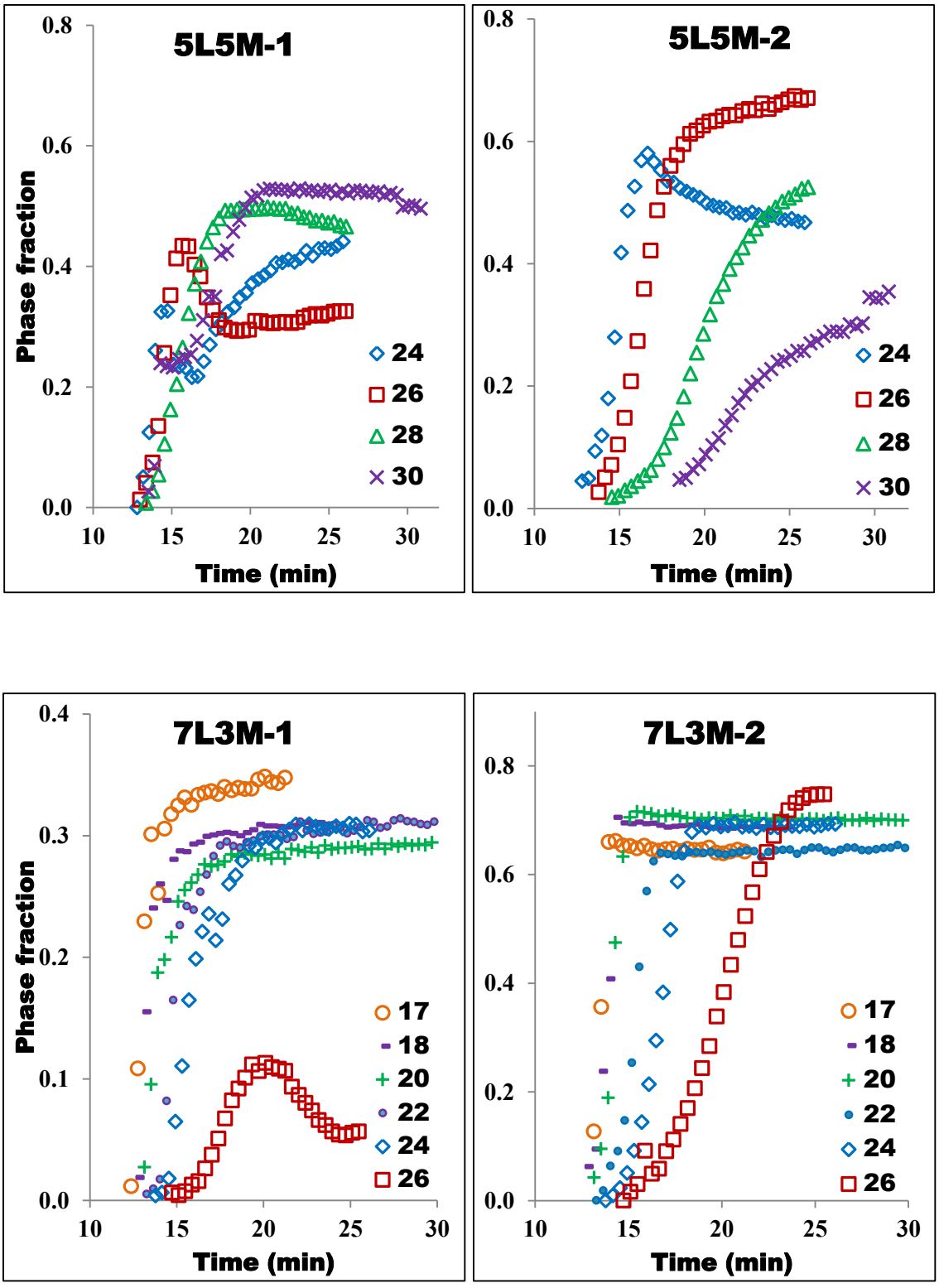

Figure 6-4. Phase fractions of both crystalline phases that were formed from 5L5M and 7L3M at different temperatures with time. The crystallization temperature in °C is shown in the legend. Title indicates the sample name and phase number.

The solid fraction of most crystalline phases increases with time. Interesting behavior was observed in the trend of the first crystalline phase obtained at 24°C and 26°C from 5L5M. An initial increase in the amount of this phase followed by a region of melting/dissolution was observed as seen in Figure 6-4 . The corresponding thickness of the crystalline nanoplatelets of these phases showed an increase in the average size of the crystallites with time during the melting/dissolution as showed in Figure 6-5. This might be due to the melting of smaller crystallites causing an overall increase in the thickness of the phase. After about 16 minutes during crystallization, slow increase in the mass of the first phase and decrease in its thickness is observed in the experiment performed at 24°C probably due to solid-solid transformation. This trend is an indication of the formation of smaller crystallites during this transformation. An opposite phenomenon in the second crystalline phase at the same time indicates the melting of smaller crystallites. This peculiar behavior of one phase melting and recrystallizing into another phase was also observed in 7L3M at 26°C. The second crystalline phase formed at lower temperatures in the case of sample 3L7M also showed this melting behavior.

As seen in Figure 6-5 and Figure 4-5, the second phase of 5L5M has a smaller thickness of crystalline nanoplatelets. Also, the observation that the second crystalline phase being the dominant phase at the end of crystallization is an indication that at lower temperatures, crystalline systems formed from the sample 5L5M have the smallest average thickness. Although the reason for this transformation is not completely understood, this phenomenon of a phase of higher crystallite size transforming into a phase of smaller crystallite size will prove to be very useful as smaller crystallites are primarily targetted in many commercial applications. A similar phase behaviour has been observed during the crystallization of cocao butter under shear (Mazzanti et al., 2007).

Although the growth of both crystalline phases takes place simultanoeusly, the onset of nucleation did not take place simultanoeusly in almost all of the experiments. The crystalline phase with higher d-spacing always nucleated prior to the nucleation of the crystalline phase with smaller d-spacing. This tendency points towards the possible inducing affect of the first crystalline phase on the formation of the second. A clear understanding of this behaviour is still unknown.

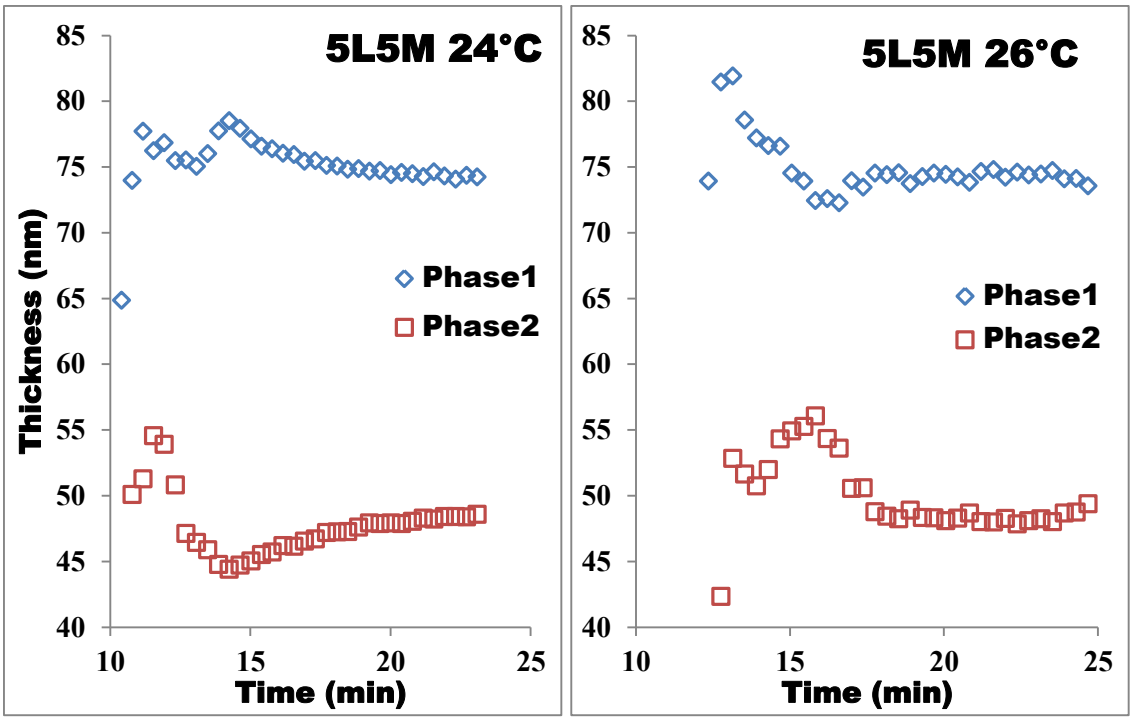

Figure 6-5. Average thickness of all the crystallites that belong to the crystalline phases obtained at 24°C and 25°C from 5L5M. This thickness is estimated from the FWHM of a peak obtained from peak fitting procedure and Scherrer's approximtion.

6.3 Calculation of liquid fraction and its composition

At all times, the sum of all the phase fractions should be equal to 1. Therefore the phase fraction of liquid phase at time t, $S_{liq,t}$, is:

$$S_{liq,t} = 1 - (S_{1,t} + S_{2,t}) \tag{6-1}$$

Here, $S_{1,t}$ and $S_{2,t}$ are the phase fractions of crystalline phases 1 and 2 at any time t

In a partially solid system with two growing solid crystalline phases the mass balance is:

$$z = x_{1,t} \cdot S_{1,t} + x_{2,t} \cdot S_{2,t} + y_t \cdot S_{liq,t} \tag{6-2}$$

Here,

z is the overall composition of trilaurin in the whole sample,

$x_{1,t}$ and $x_{2,t}$ are the compositions in crystalline phases 1 and 2 at time t,

y_t is the composition of the remaining liquid at time t.

The composition of the liquid (y_t) can then be calculated from (6-2) as:

$$y_t = \frac{z_L - \left(x_{1,t} \cdot S_{1,t} + x_{2,t} \cdot S_{2,t}\right)}{S_{liq,t}} \tag{6-3}$$

The liquid phase fractions and their compositions with time for all three binary mixtures are shown in Figure 6-6 and Figure 6-7.

Although Figure 6-7 shows that the composition of the liquid phase is different at any point of time as the crystallization temperature changes, the shape of these trends are not fairly different from each other. This is an indication that the change in composition is just a consequence of the rate of change of the amount of liquid phase as the system crystallizes. The initial rate of increase in the trilaurin mole fraction in the liquid phase is directly related to the rate of crystallization.

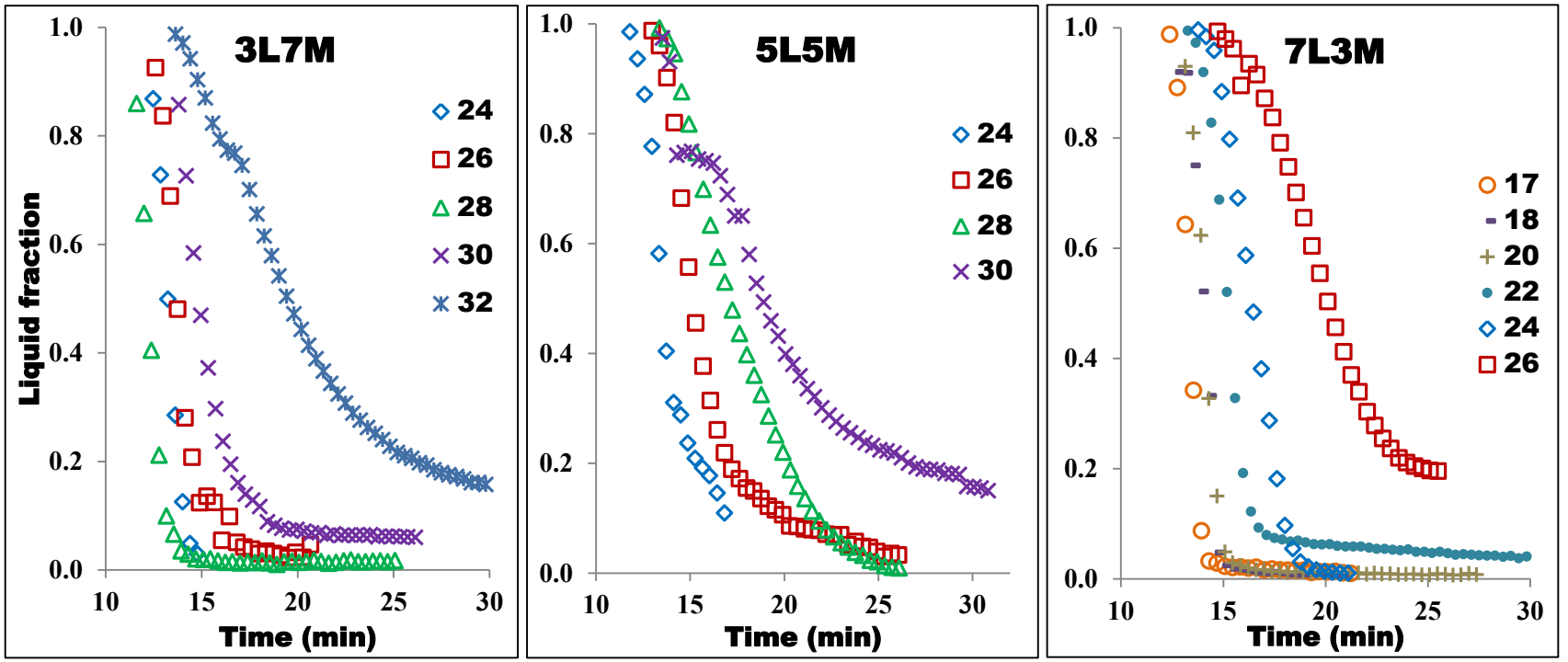

Figure 6-6. Liquid phase fraction as a function of time at different temperatures. The crystallization temperature is shown in the legend. Title indicates the sample name and phase number.

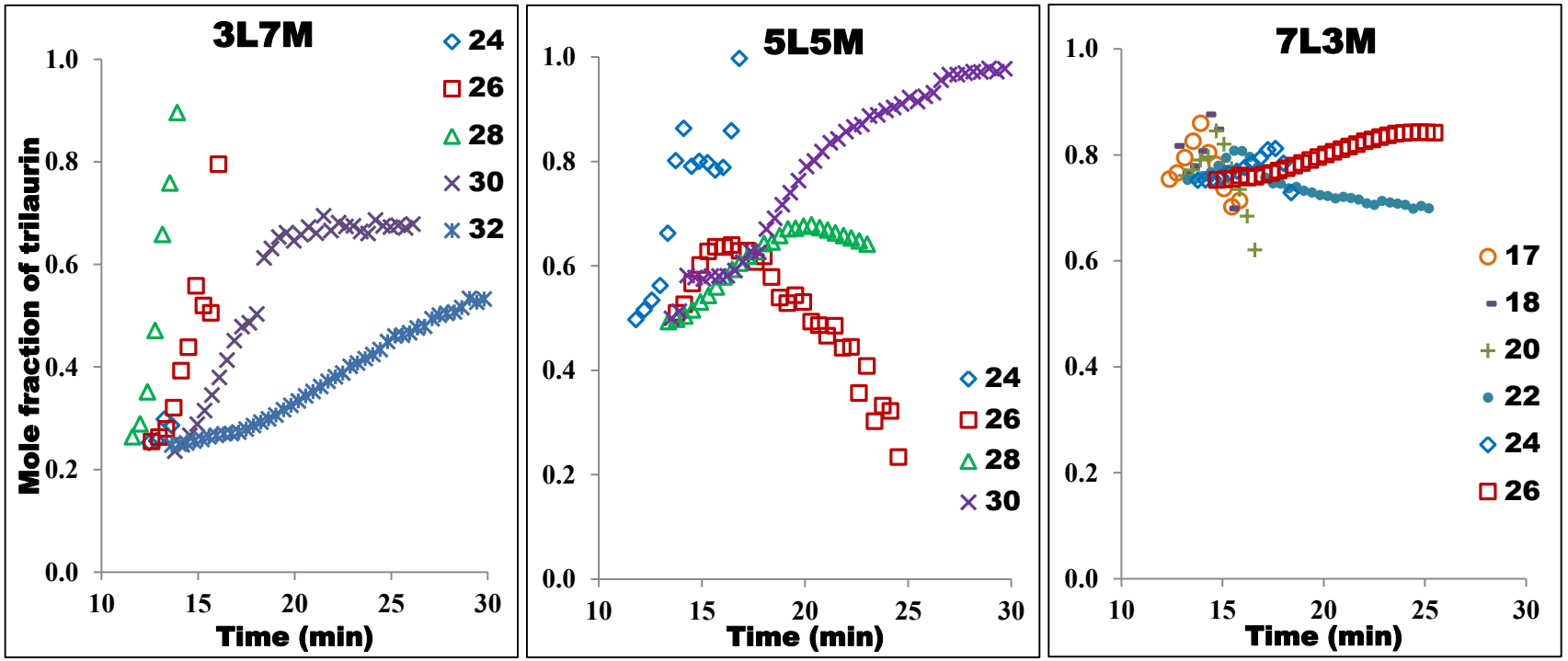

Figure 6-7. Mole fraction of trilaurin in liquid as a function of time. Legends show the temperatures in °C.

6.4 Instantaneous compositions of the material crystallizing from the liquid

The formation of crystalline solid(s) from a liquid mixture affects the composition of the remaining liquid. Therefore, the composition of the solid(s) crystallizing out of this changed liquid will have a different composition than the solid that had crystallized before.

TAG molecules have a small diffusivity in the liquid state, of the order of 10^{-11} m^2/s (MacLean, 2012), and an essentially negligible diffusivity in their solid state (Los & Flöter, 1999). Although not precisely quantified, the crystallization conditions for the mixtures studied correspond to a high degree of undercooling. Thus, it is likely that the rate of deposition of solid material from the liquid is much faster than diffusion in the liquid and therefore dominates crystallization.

A possible mechanism of growth of crystas from a binary liquid is as follows:
A crystallizing solid phase at any instant will have a different composition than the liquid from which it is crystallizing. As a result, the crystallization of solid phase from a liquid causes a change in the overall composition of that liquid. Thus, the solid material that crystallizes during a later time on top of an existing crystalline phase would not have the same composition as the existing crystalline phase. These consecutive layers of solid material in a crystalline phase will not equilibrate between them due to negligible diffusion in the solid phase.

The proposed mechanism is consistent with the change in composition of a crystalline phase as it grows, as can be seen in Figure 6-1. Figure 6-8 a. shows a rough sketch of the concentration gardient in a TAG crystallite, the darker region represents higher relative concentrations of trilaurin. The blue boundary represents the liquid-solid interface. and Figure 6-8 b. shows the growth of a crystallite's surface by adding newer layers. The blue arrow shows growth as time goes by. The growth of a phase can also happen in a parallel regime where newer crystallites were formed instead of forming a new layer on the existing crystallite. This second regime of crystallization is not shown here.

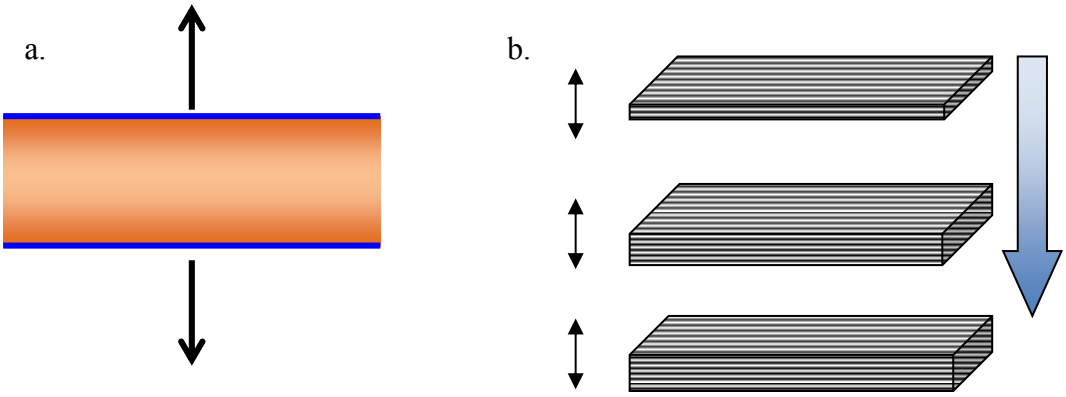

Figure 6-8. Crystal growth. (a.) concentration gradient along triglyceride crystallite, (b.) growth of a crystallite by the addition of a new layer of molecules on top of each other (Drawing by Dr. Gianfranco Mazzanti)

Thus, the composition of a crystalline phase that is calculated from the d-spacing at any time t, corresponds to the average composition of the whole phase rather than the composition of solid material that is being crystallized at any point of time at the interface (instantaneous composition). These instant compositions of solid phases with their respective composition of liquid phases are the experimental variables that are needed to estimate the interaction parameters and the kinetic parameters in the LKS model to construct predictive phase diagrams.

These instantaneous compositions of the solid phases were calculated using a conservation of mass approach.

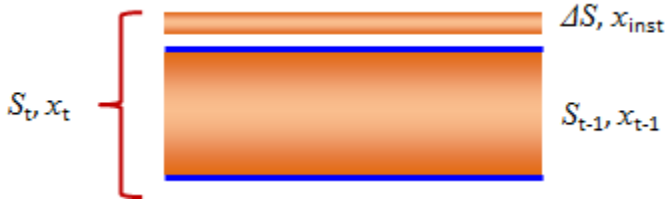

Figure 6-9. Addition of a new solid material on an existing crystallite

Here in Figure 6-9, S_{t-1}, x_{t-1} and S_t , x_t are the mass fractions and compositions of a crystalline phase at two consecutive times *t-1* and *t* calculated from the d-spacings and XRD integrated intensity of that phase. If ΔS and x_{inst} are the amount and composition of the solid phase that has crystallized during the time interval between *t-1* and *t,* mass balance in terms of trilaurin composition in the solid phase is:

$$S_t \cdot x_t = S_{t-1} \cdot x_{t-1} + \Delta S \cdot x_{inst} \tag{6-4}$$

S_{t-1} can be expressed as $S_t - \Delta S$, using this in (6-4) and after rearrangement:

$$S_t \cdot x_t - (S_t - \Delta S) \cdot x_{t-1} = \Delta S \cdot x_{inst} \tag{6-5}$$

Simplifying (6-5) yields,

$$x_{inst} = x_{t-1} + \frac{\Delta x}{\Delta S} \cdot S_t \tag{6-6}$$

If $\Delta x \rightarrow 0$ and $\Delta S \rightarrow 0$, $x_{t-1} \rightarrow x_t$, so, in general terms, equation (6-9) can be rearranged as:

$$x_{tj,inst} = \bar{x}_{jt} + \frac{\partial \bar{x}_{jt}}{\partial S_{jt}} S_{jt} \tag{6-7}$$

Here,

$x_{tj,inst}$ is the instantaneous composition of a crystalline phase *j* at time t

$\bar{x}_{jt}$ is the average or the overall composition of that crystalline phase at time t calculated from its corresponding d-spacing

S_{jt} is the phase fraction at time t

6.4.1 Smoothing procedure

Calculating a numerical derivative for a dataset that is not smooth as seen in Figure 6-1 and Figure 6-4 produces large unreal values due to the variability in the system caused by noise. After testing various smoothing algorithms available in 'Igorpro', the 'Savitzky–Golay' smoothing procedure with 13 points and a fourth order polynomial was found to produce better results than the other smoothing procedures tested. Therefore, this procedure used to smooth the trends in experimental compositions and phase fractions of both the crystalline phases with time for each experiment performed.

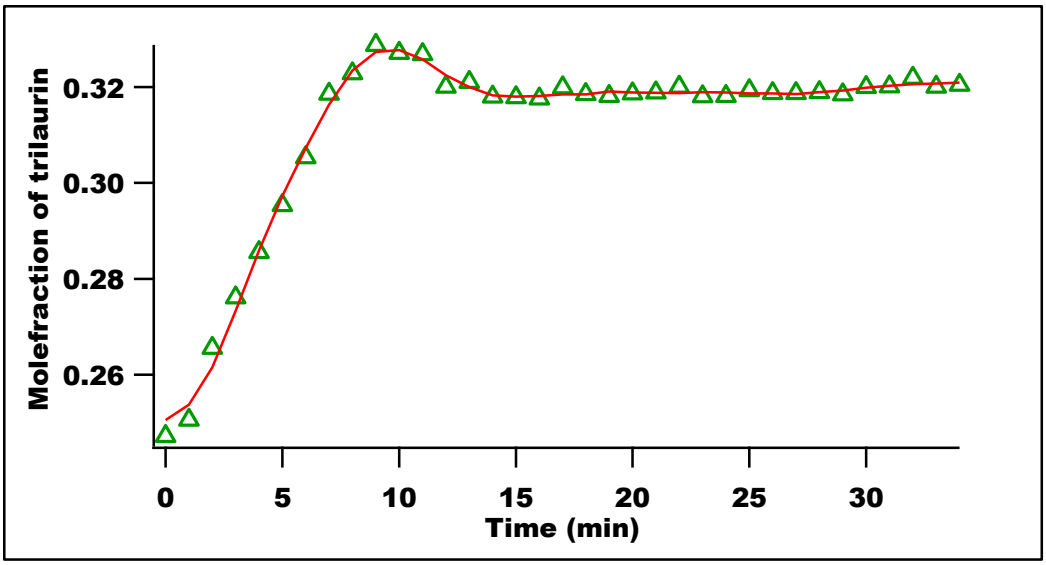

Figure 6-10. Experimental (green triangles) and smoothed (red line) mole fraction of trilaurin in the first crystalline phase as a function of time from 5L5M crystallized at 26°C.

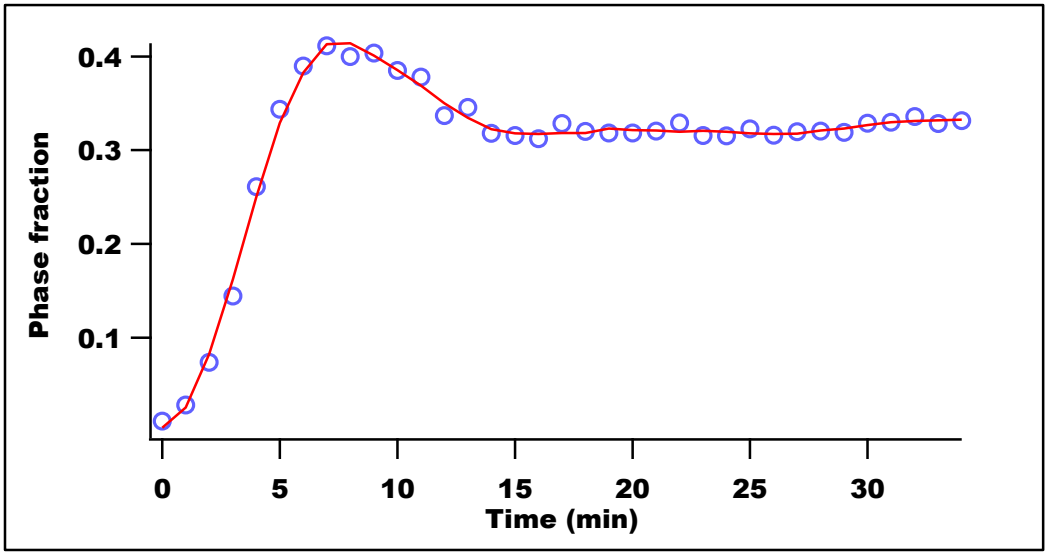

Figure 6-11. Experimental (blue circles) and smoothed (red line) phase fraction of the first solid crystalline phase as a function of time from 5L5M crystallized at 26°C.

6.4.2 The relative change in composition with respect to phase fraction

Numerical derivatives of smoothed composition (x) and phase fraction (S) with time were calculated using a central differences method for each solid crystalline phase

by ‘Igorpro’. The change in composition with respect to change in phase fraction is calculated from the individual change of composition and solid fraction with time:

$$\frac{\partial x_j}{\partial S_j} = \frac{\frac{\partial x_j}{\partial t}}{\frac{\partial S_j}{\partial t}} \tag{6-8}$$

Instantaneous compositions of both solid phases crystallizing from the liquid were calculated at three chosen temperatures for each of the three binary mixtures. Figure 6-12 show the change in the calculated instantaneous composition with time as crystallization proceeds. Figure 6-13 shows the calculated instantaneous composition of each crystalline phase along with the corresponding composition of liquid phase from which they have formed. This figure is of very high significance as a succesful model should predict the formation of crystalline phases of these instantaneous compositions from their corresponding liquid phase and crystallization temperature. The instantaneous compositions were not calculated all the way until the end of crystallization i.e., when the total solid fraction becomes equal to one, because as the crystallization process reaches completion, even small changes in either the composition or solid fraction due to noise in measurement causes huge changes in the instantaneous composition, producing unreal values which do not follow any trend. This also applies to the composition of the liquid phase illustrated in .

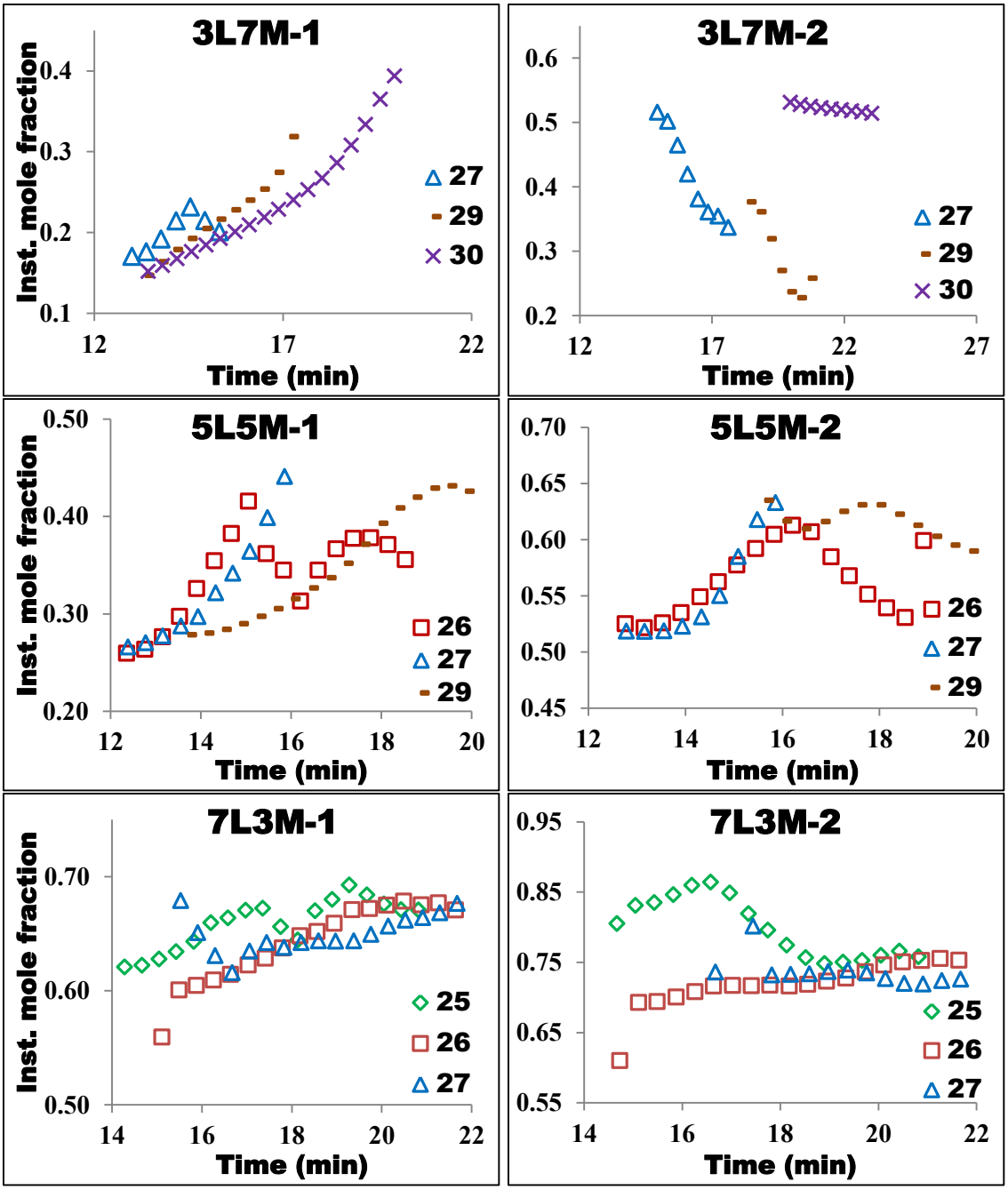

Figure 6-12. Instantaneous compositions of solid materials crystallizing from the liquid obtained from the three binary mixtures with time. Legend shows the temperature in °C.

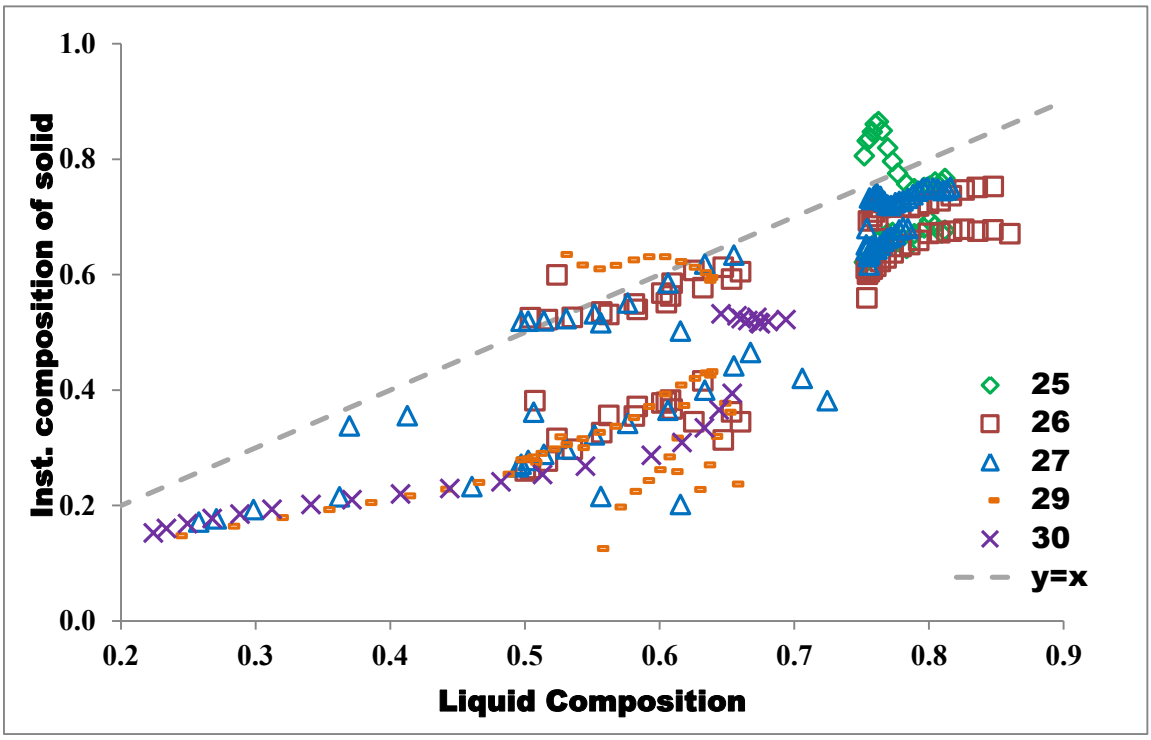

Figure 6-13. Calculated composition of liquid phase at any point in time plotted aagainst the corresponding instantaneous composition of both the crystalline phases growing simultaneously. Legend shows the crystallization temperature in °C.

Figure 6-13 shows a weak trend between the instantaneous compositions of all he crystalline phases with their corresponding liquid compositions from which they have appeared. Clearly, two very different trends/regions coexist in the plot shown. Looking back into experimental data, it is clear that the two trends correspond to the compositions of the two distinct crystalline phases that appear simultaneously. With any particular set of thermodynamic and kinetic parameters, the LKS model should mathematically describe the two trends/regions simultaneously.

6.5 Calculation of thermodynamic and kinetic parameters

The linear kinetic segregation (LKS) model proposed by (Los & Flöter, 1999) is a prominent theoretical model available to construct kinetic phase diagrams for two

component systems made up of materials like TAGs. (See '2.1.3.2.4' for details). These kinetic phase diagrams are intended to predict the composition of a crystalline phase(s) formed at any undercooled temperature 'T' from a liquid of known composition.

6.5.1 Method to calculate a set of interaction parameters and kinetic parameters

The LKS model for a system crystallizing into any number of crystalline phases at a temperature 'T' and at any time 't' during the crystallization process is summarized by:

$$\left(\frac{x_{j,t}}{1-x_{j,t}}\right)=\kappa_{LM,0}\cdot\left(\frac{\gamma_{M,j,t}}{\gamma_{L,j,t}}\right)^{\varepsilon}\frac{y_t-x_{j,t}\cdot\gamma_{L,j,t}\cdot K_L}{(1-y_t)-(1-x_{j,t})\cdot\gamma_{M,j,t}\cdot K_M} \tag{6-9}$$

Where, j is the phase number

$x_{j,t}$ is the concentration of trilaurin in the crystalline phase j at time 't'

y_t is the concentration of trilaurin in the liquid phase at time 't'

$\gamma_{L,j,t}$ and $\gamma_{M,j,t}$ are the activity coefficients of trilaurin and trimyristin in crystalline phase j at time t

K_L and K_M are the thermal factors of trilaurin and trimyristin at a crystallization temperature 'T'.

$\kappa_{LM,0}$, ε are the kinetic constants ratio and kinetic separations parameter

A three suffix Margules equation was used to describe the activity coefficient in a crystalline phase j,

$$\gamma_{i\_j}=\exp\left[\frac{\overline{T}}{T}x_k^2\left(\phi_{ik}+2\left(\phi_{ki}-\phi_{ik}\right)x_i\right)\right] \tag{6-10}$$

i,k represents the component number i.e., they can be either trilaurin or trimyristin

$\overline{T}$ is the average melting point of both components in the polymorphic form of interest (β')

T is the crystallization temperature

ϕ_{ik} and ϕ_{ki} are the interaction parameters of component i with a bulk of component k and vice-versa.

The thermal factors K_L and K_M are represented as

$$K_i = \exp\left[\frac{-\Delta H_i}{R}\left(\frac{1}{T}-\frac{1}{T_i}\right)\right] \qquad (6\text{-}11)$$

Where, ΔH_i is the enthalpy of crystallization of component *i* in its pure form

T_i is the melting point of component *i* in its pure form

Using equations (6-10) and (6-11) in equation (6-9), The left hand side (LHS) and right hand side (RHS) of equation (6-9) were calculated for each pair of liquid composition and its corresponding instantaneous composition of solid phase. These pairs of liquid composition and its corresponding instantaneous solid phase composition that were used in the calculation are shown in Figure 6-13. A square of difference between the calculated LHS and RHS of equation (6-9) was calculated. The mass fraction of the crystallizing phase was used as weighing factor for each squared difference. An Excel solver method was employed to reduce the sum of squares of difference between all calculated LHS and RHS of equation (6-9) produced by all instantaneous composition-liquid composition pairs by changing the set of interaction parameters ϕ_{LM} , ϕ_{ML} and the two kinetic parameters $\kappa_{LM,0}$, ε.

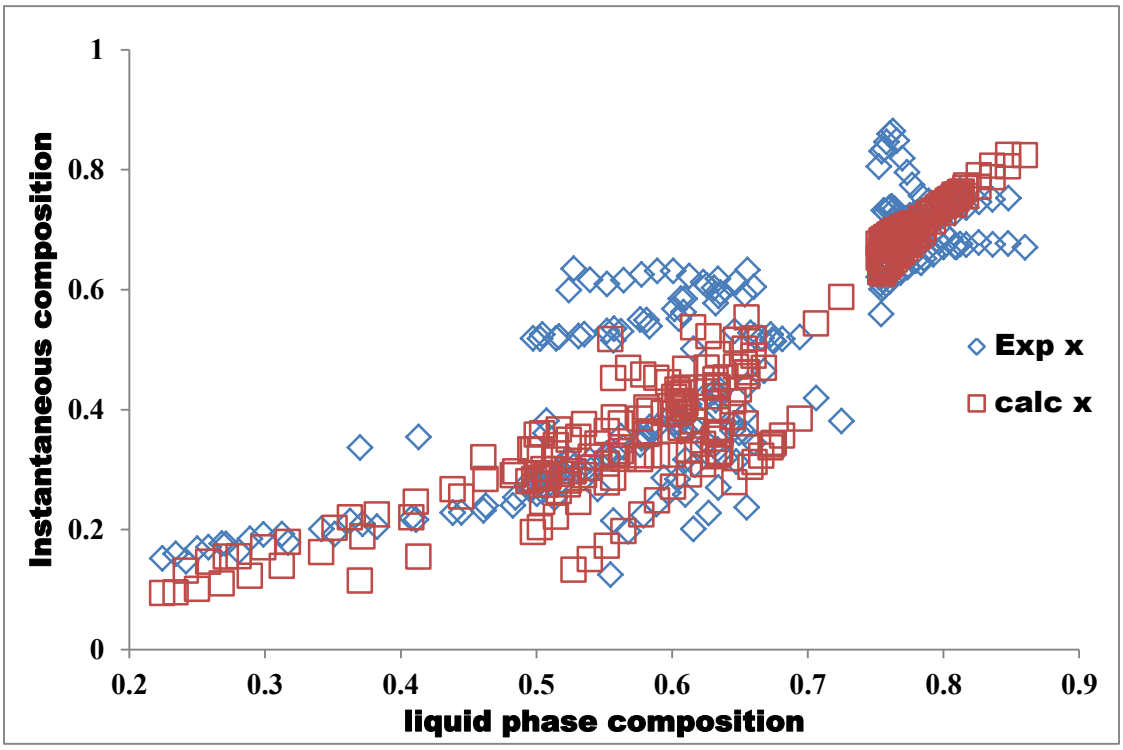

Figure 6-14. Experimental and calculated instantanoeus compositions of crystalline phases against their respective liquid phase composition.

Although not perfect, the experimental and calculated instantaneous compositions of the solid phases that are being evolved from a liquid phase overlap to a certain extent as seen in Figure 6-14. The set of interaction parameters and kinetic parameters obtained through Excel solver method are shown in Table 6-1.

Table 6-1. Set of interaction parameters and kinetic parameters obtained by reducing the sum of quare of difference between LHS and RHS of equation (6-9) using Excel solver

Parameter	Value
ϕ_{LM}	1.23
ϕ_{ML}	2.50
$\kappa_{LM,0}$	0.82
ε	0.00

As both the liquid composition and instantaneous solid phase composition are not separated on either side of equation (6-9), the calculated instantaneous composition of a particular crystalline phase utilizes the actual experimental composition of that particular crystalline phase along with the set of parameters described in Table 6-1. Thus, further testing as described in the latter part of this section was performed to verify if these set of parameters have the capability to produce two crystalline phases from the same liquid although Figure 6-14 shows a certain overalp between the calculated and actual instantaneous compositions of both the crystalline phases simultaneously from the same liquid.

An initial arbitrary liquid composition was chosen and a range of LHS values in equation (6-9) were estimated using a series of solid phase compositions at a constant increment. Corresponding RHS values of equation (6-9) were calculated for each corresponding solid phase composition in the considered series. The calculated LHS values and RHS values were plotted against the corresponding solid phase composition in the series considered. Each intersection point between these two series shows a mathematical solution or the predicted composition of the solid phase that would be formed from that particular arbitrary liquid composition. The presence of two intersection points shows that the set of interaction and kinetic parameters predict the formation of two crystalline phases from that particular liquid. These plots were shown in Figure 6-15.

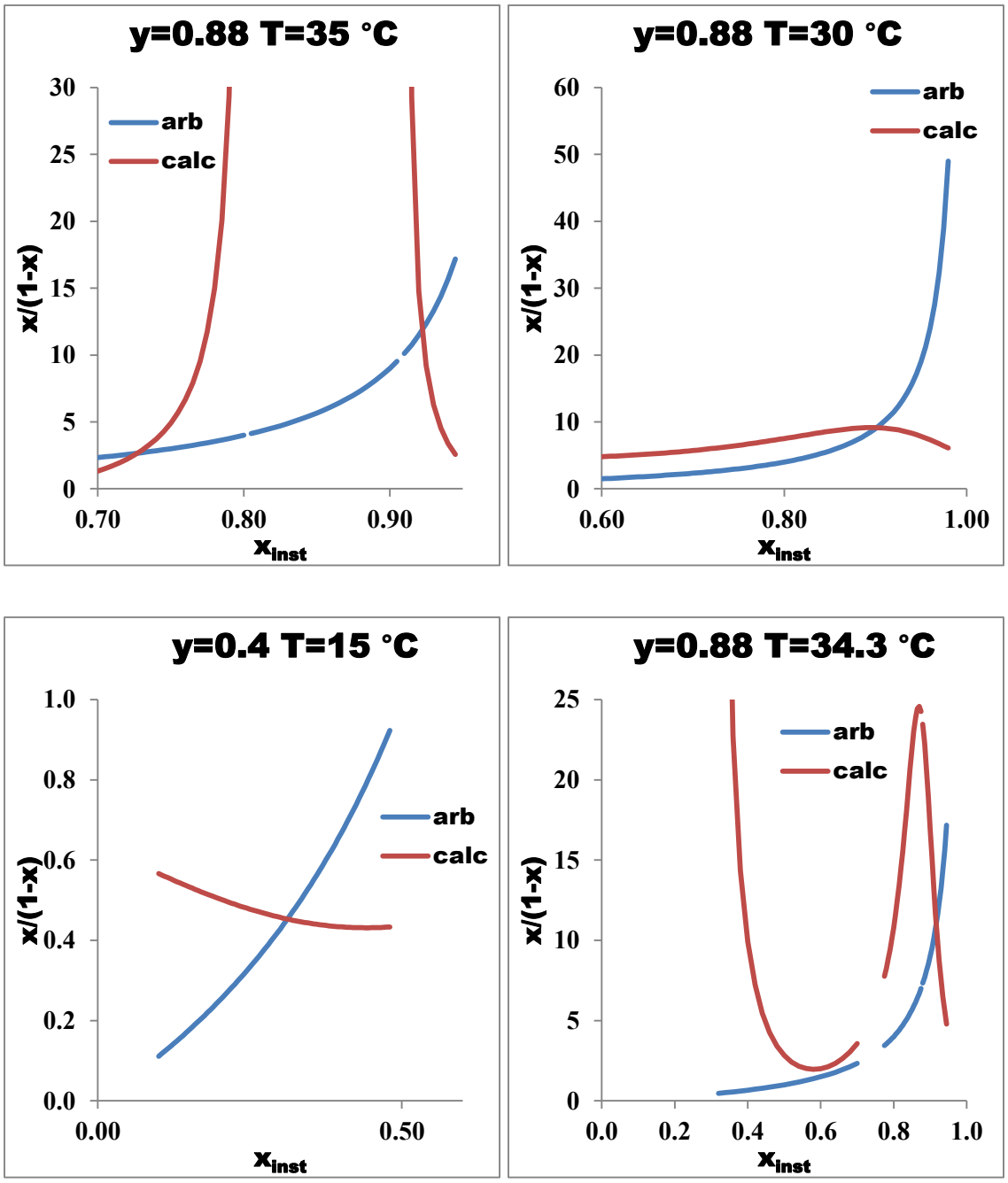

Figure 6-15. Sample plots of arbitrary and calculated solid phase compositions using LKS model shown in equation (6-9) and the set of parameters in table Table 6-1 to test the prediction of a system with two crystalline phases from the same liquid. The title of each plot shows the arbitrary liquid composition and temperature considered.

Figure 6-15 shows that there seem to be a limit for temperature and composition of liquid phase below which LKS model with the set of parameters shown in Table 6-1 cannot predict the formation of two crystalline phases simultaneously. The minimum

temperature 35 °C to show the presence of two crystalline phases is clearly higher than each and every crystallization temperature explored in the context of this study. The calculated curves of instantaneous compositions at different temperatures using the LKS model also did not show the presence of two crystalline phases as evident in Figure 6-16. The series with an ending 'c' correspond to the calculated instantaneous composition.

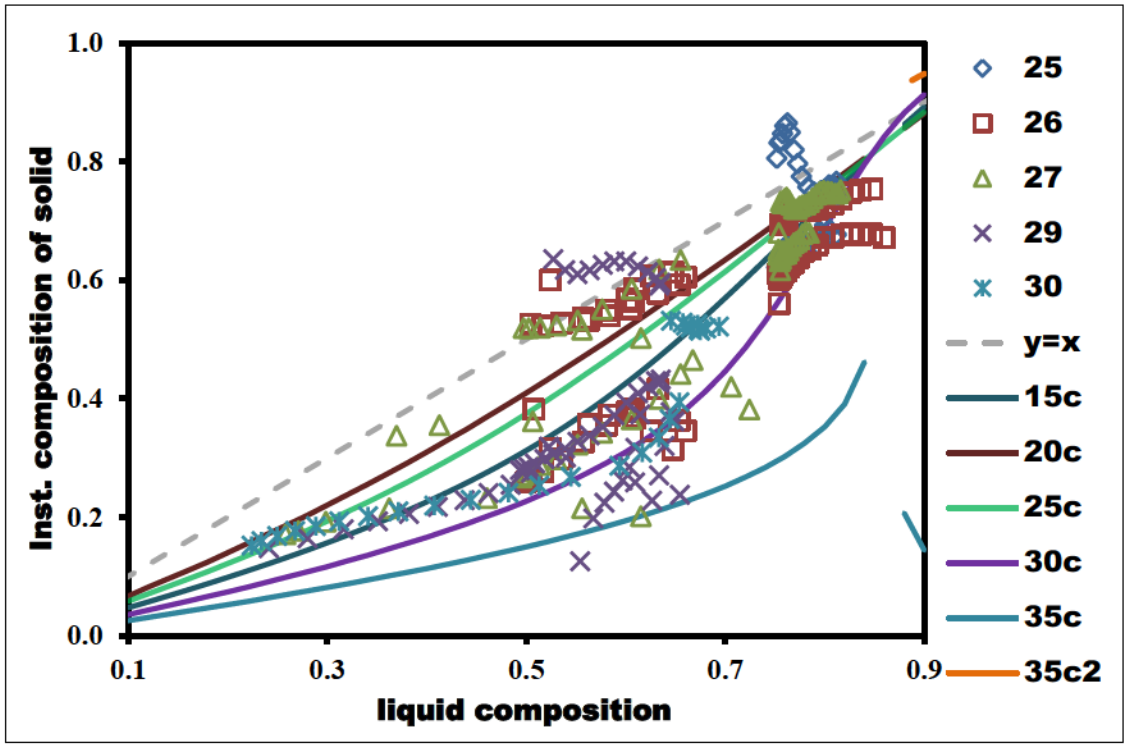

Figure 6-16. Experimental instantaneous solid phase compositions and calculated trends in solid phase compositions at different liquid compositions. The trend 35c2 corresponds to the predicted composition of the second crystalline phase using the LKS model

Although, the LKS model failed to describe the formation of two crystalline phases from a liquid simultaneously, with the set of parameters described in Table 6-1 it was able to describe the formation of one of the crystalline phases from the system as shown in Figure 6-17.

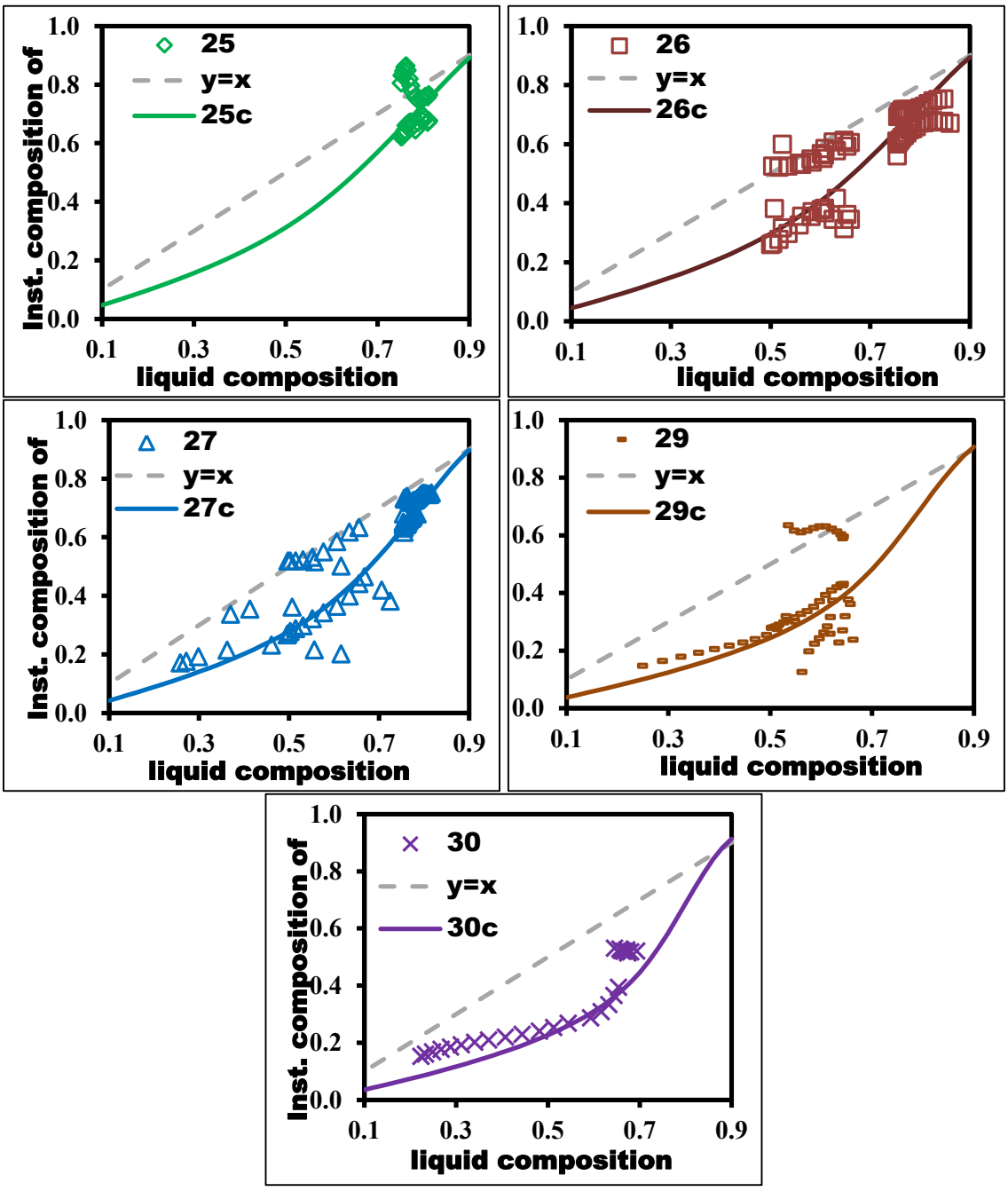

Figure 6-17. Calculated and experimental instantaneous composition of one of the crystalline phases at different temperatures tested.

6.5.2 Equilibrium phase diagram produced by the estimated set of interaction parameters

The basic philosophy of LKS model is to first understand the equilibrium condition between a liquid binary mixture and a solid phase that would be formed at

a particular temperature and distort this equilibrium to describe the phase formation at a non-equilibrium condition (See section 2.1.3.2.4). Thus, it is essential to verify if the set of interaction parameters have the capability to produce a plausible equilibrium phase diagram that predicts the formation of two crystalline phases simultaneously.

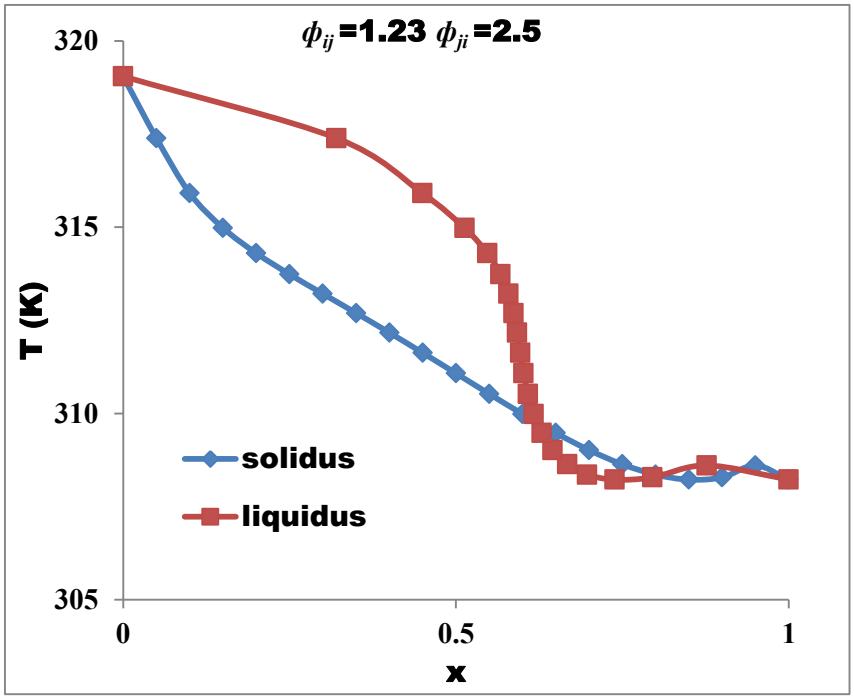

Figure 6-18. Equilibrium phase diagram between liquid and solid trilaurin-trimyristin binary mixtures at different temperatures using the set of estimated interaction parameters

The crossover in Figure 6-18 indicates that a phase with a particular composition can still exist in liquid state even at a temperature below the melting point of a solid phase of the same composition. This equilibrium behaviour is physically impossible.

The LKS model was able to describe the formation of one of the crystalline phases from a particular liquid composition with a set of interaction parameters that do not have the capability to produce a plausible equilibrium phase diagram. Perhaps when a system is too far away from equilibrium, a distortion is caused to a pseudo equilibrium condition as in Figure 6-18 to describe a kinetic process instead of the true equilibrium condition.

6.5.3 Possible reasons for the failure of the LKS model to describe the experimental data

a. The compositions of the crystalline phases tend to form sequential pairs evident from Figure 4-1, Figure 6-1 and Figure 6-2. A possible solution of interaction parameters and kinetic parameters should also satisfy this condition. A possiblity exists that the three suffix Margules model used to describe activity coefficients does not have enough flexibility to explain the formation of two phases simultaneously. Due to the very peculiar distribution of the instantaneous compositions with respect to the liquid phase composition from which they have formed (Figure 6-14), it is extremely hard to find a set of parameters that would satisfy this behaviour.

b. It is possible that the liquid phase is split into two separate phases. As a result, each solid phase observed might be at an equilibrium with a different liquid phase. Peak fitting of WAXD patterns obtained when a mixture is partially crystalline (both during crystallization and melting) showed the possible presence of two distinct broad liquid like peaks. This might be an indication of phase splitting in the liquid phase. More experiments should be performed to verify this phenomenon (See section 7.4).

c. Differences in the WAXD patterns were observed between the crystalline phases obtained from different samples (see section 7.1). In the case of phases obtained from the sample 3L7M, the position of one of WAXD peaks was clearly different from the respective peak position of the crystalline phases evolved from the samples 5L5M and 7L3M (see Figure 7-1). These differences in peak positions point to dissimilarities in the arrangement/sub-cell packing of the phases obtained from different samples. The LKS model might not be able to describe the collective formation of crystalline phases with such differences.

Chapter 7 RESULTS AND DISCUSSION FROM WIDE ANGLE X-RAY DIFFRACTION (WAXD) PATTERNS

WAXD patterns give information about the lateral stacking of hydrocarbon chains in a TAG crystalline system, as explained Chapter 1. Traditionally WAXD patterns were just used to identify the polymorphic form, but the analysis of WAXD patterns that were captured simultaneously with SAXD patterns indicated that much more information can be deduced. Also the time resolution of the captured WAXD patterns provided the opportunity to study the changes in the molecular arrangement as a crystalline system grows. This chapter offers an overview of the understanding obtained from the analysis of WAXD patterns and also suggests some possible applications from the analysis.

7.1 Identification of polymorphic form obtained

The identification of the polymorphic form is done through the comparison of d-spacings obtained from peak fitting of these WAXD patterns with a standard set of d-spacings reported in the literature for a particular polymorphic form (Lutton & Fehl, 1970; Takeuchi et al., 2003) (See Table 2-2). The polymorphic form of all the crystalline phases obtained was identified as β'.

Each peak in the WAXD pattern corresponds to the distance between planes of atoms in a particular direction. The d-spacings calculated from WAXD patterns are shown in Figure 7-1. Although the WAXD patterns obtained from all the samples of 3L7M, 5L5M and 7L3M do have the characteristic peaks allowing the identification of polymorphic form β', differences were observed in their positions and widths. These differences are mainly due to two factors affecting the arrangement of molecules; specifically,

- Crystallization temperature
- Composition of the solid solution affecting the sub polymorphic modification

7.1.1 Crystallization temperature

A slight increase in the d-spacing of a characteristic peak is observed with the increase of temperature (see Figure 7-1). These differences are due to the increase in the

internal energy of the TAG molecules in a crystal causing an increase in the average distance between two hydrocarbon chains. The increase in the d-spacing is more pronounced for some characteristic peaks (eg., peak with a d-spacing of about 0.42 nm) and are not very obvious for the other characteristic peaks (eg., peak with a d-spacing of about 0.38 nm). A possible reason for the difference in the effect of temperature produced on different characteristic peaks is the difference in the combination of attractive forces between the hydrocarbon chains in that particular direction. A study to quantify the differences in WAXD patterns caused by temperature on various polymorphic forms of pure and mixed TAG crystalline phases is being carried by a colleague of our research group.

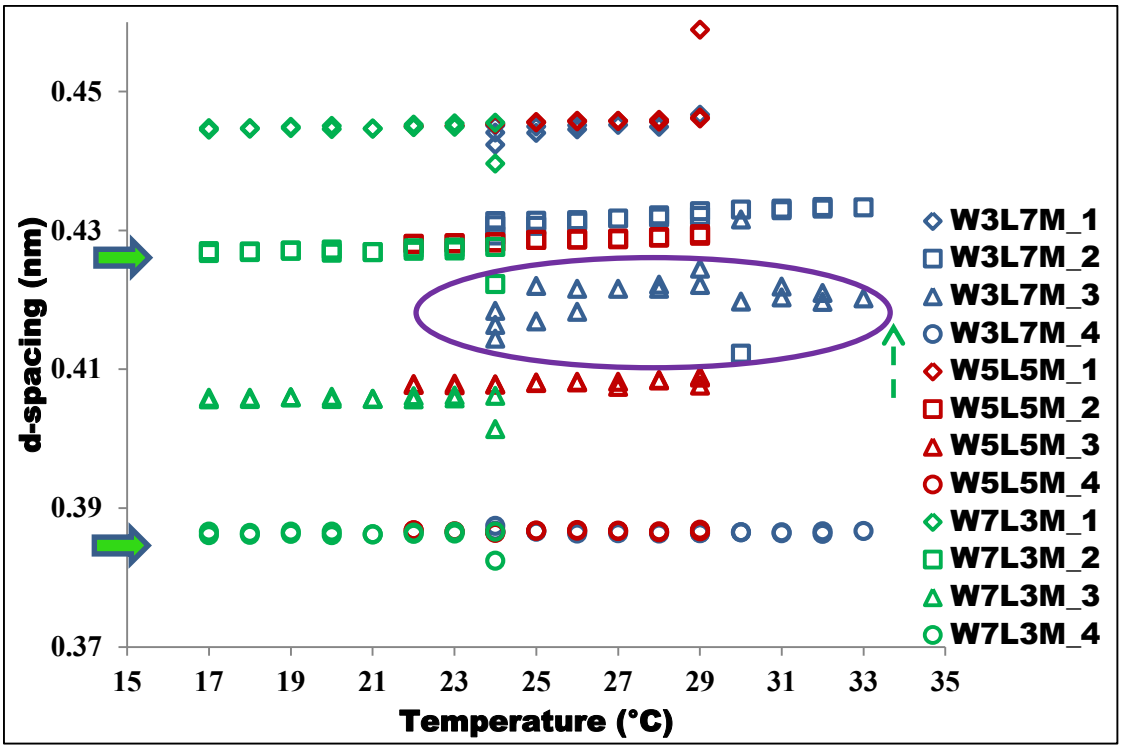

Figure 7-1. d-spacings from WAXD patterns obtained at the end of an experiment as a function of temperature. The set of d-spacings shown by the green arrows correspond to the characteristic d-spacings for the polymorphic form β'. The circled region highlights the shift in the peak position of one of the characteristic peaks in the crystalline phases rich in trimyristin.

7.1.2 Sub-polymorphic modifications

A clear difference in the shape of the WAXD patterns was observed between different samples. Although, upon fitting these patterns, the peak positions of the

characteristic peaks tend to be very close to one another (pointed out by green arrows in Figure 7-1), the difference in the shape of these peaks, and also the position of one of the peaks as seen in Figure 7-1 was a clear indication of differences in the arrangement of molecules with respect to one another. These crystalline systems with slight differences in the arrangement of molecules within a particular set of repetitive planes are referred to as sub-polymorphic modifications by Wesdorp (Wesdorp, 1990), Adopted from Marangoni & Wesdorp (2012).

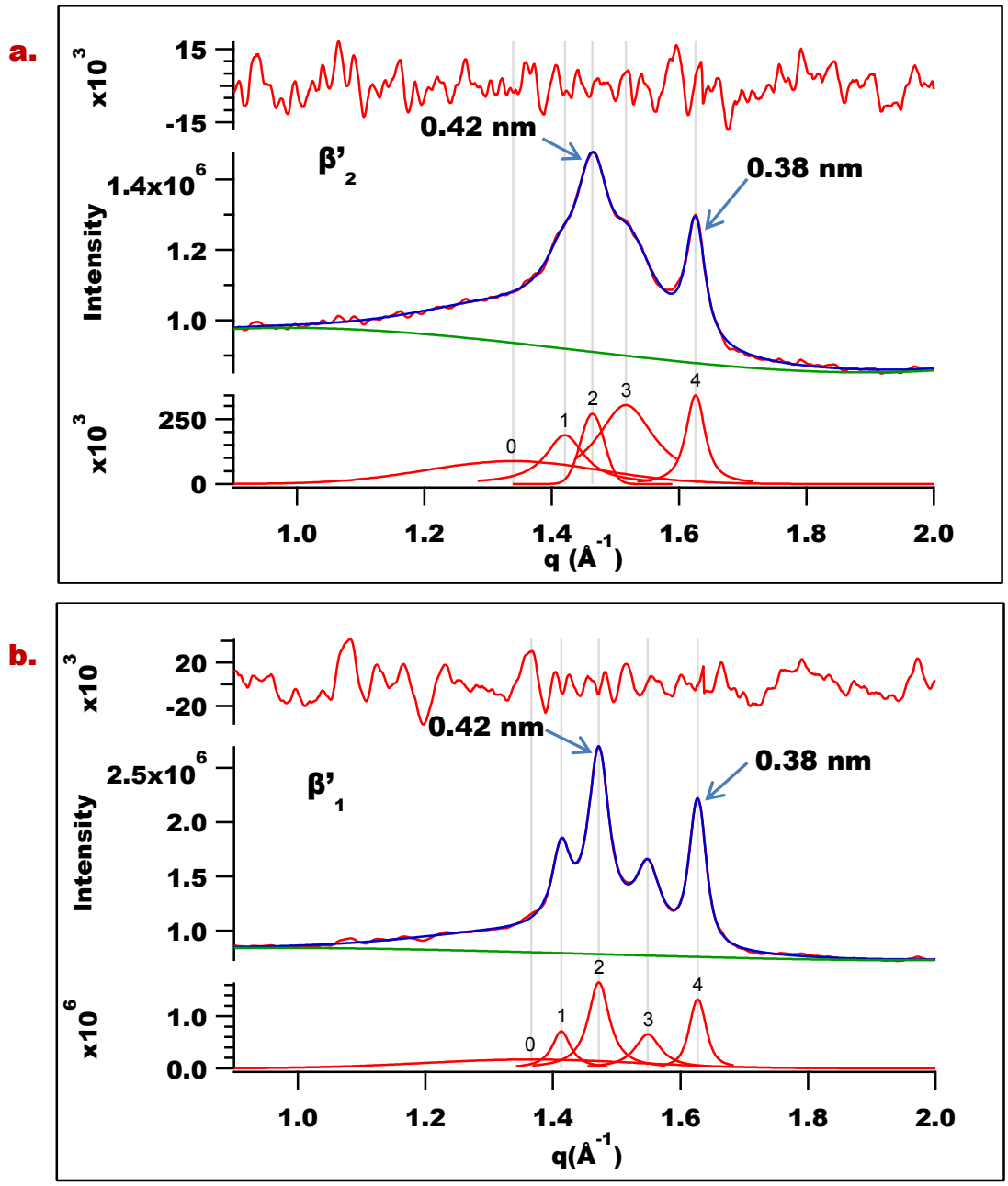

Figure 7-2. WAXD patterns of the same polymorphic form β' having different shape. a. A typical pattern obtained from a crystalline system rich in MMM, and b. Pattern obtained from a crystalline system rich in LLL. In each plot the top curve represents the residuals of peak fitting, the middle curve represents the overlap between the original diffraction pattern and the sum of the fitted functions and the bottom peaks show the individual peaks that are fitted into the experimental diffraction pattern.

In the context of this study, the TAG crystalline phases are divided into two sub polymorphic modifications based on their WAXD patterns. Crystalline phases with

diffraction patterns similar to Figure 7-2-b that have sharper and well resolved peaks will be referred to as β'_1 and phases that produce patterns similar to Figure 7-2-a that have less resolved peaks will be referred to as β'_2. A WAXD pattern is not produced by a single crystalline phase, but is a result of a combination of x-rays that diffract from all the crystalline phases that coexist in the system. As a result, a WAXD pattern is a weighted combination of diffraction patterns obtained from all the crystalline phases present in a system. For the sub-polymorphic form β'_1, the amplitude of the peaks in a WAXD pattern are in the order, 3<1<4<2 while, for the other form β'_2, the order of amplitudes are 1<2<3<4. Sharper and well resolved peaks suggest a better arrangement of molecules in terms of consistent spacing between consecutive layers. While, a broader peak corresponds, conversely, to a poorer arrangement or a lesser number of repetitive layers.

7.2 Correlation lengths of characteristic WAXD peaks

The correlation length corresponds to the average distance that is free of defects in the particular direction of a set of repeating planes producing a characteristic peak. These correlation lengths are calculated from the full width at half maximum (FWHM) of a diffraction peak using Scherrer's approximation (see section 2.2.2.2). Figure 7-3 shows the correlation lengths from WAXD peaks with their corresponding crystallization temperature. Although these correlation lengths are calculated the same way as the thickness of the crystals calculated in the context of SAXD patterns as described in section 4.4 these correlation lengths do not represent the thickness of the whole crystal. They correspond to rather an average distance in the particular direction of the crystalline phase that is defect free. These distances are not in the direction that is parallel to the lamellar planes that diffract x-rays at small angles, but closer to being orthogonal to those planes.

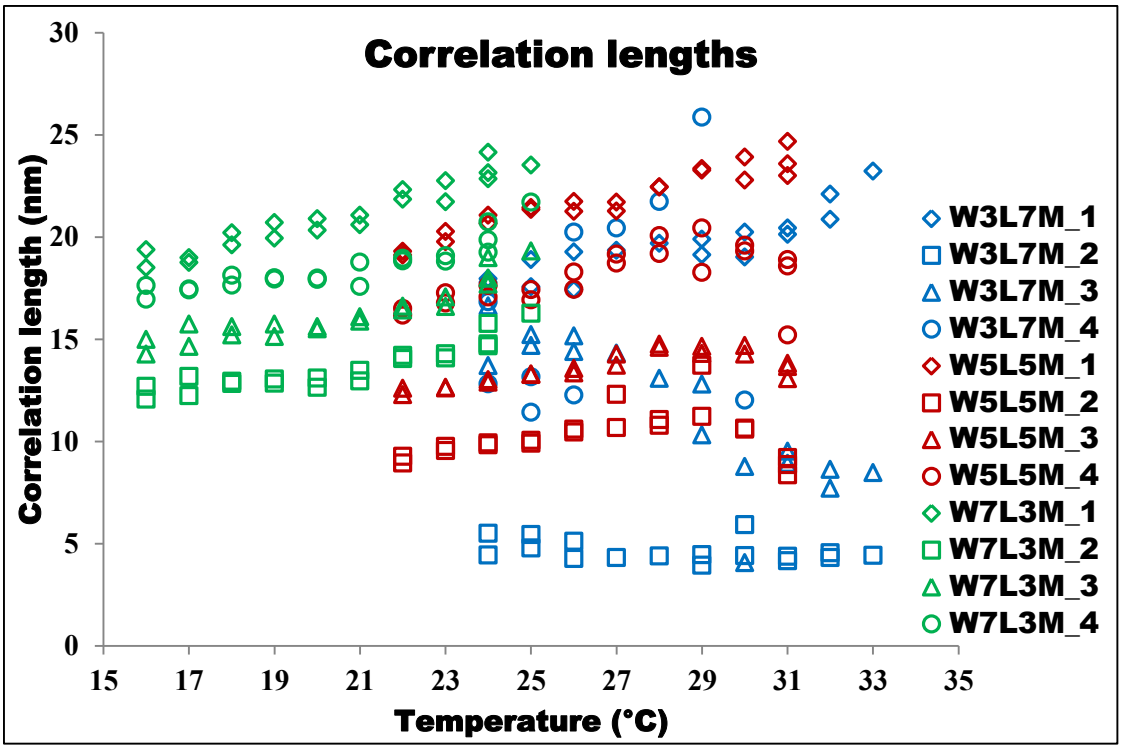

Figure 7-3. Correlation lengths of the characteristic peaks plotted against crystallization temperature.

It is very clear from Figure 7-3 that the correlation length of a particular peak increases with temperature and also with the relative amount of trilaurin in a particular phase. Slowly grown crystalline systems develop fewer defects than a system grown at a higher rate. This leads to another speculation on sub polymorphic modifications that the difference in the WAXD patterns could be due to differences in the perfection of arranged molecules in TAG mixed crystals.

7.3 Liquid scattering area

For a TAG system, the wide angle liquid scattering pattern falls in a region very close to the diffraction pattern produced by a crystalline material. This is a great advantage as both the liquid scatter and diffraction patterns can be captured simultaneously with a single 2D x-ray detector (See Figure 7-4).

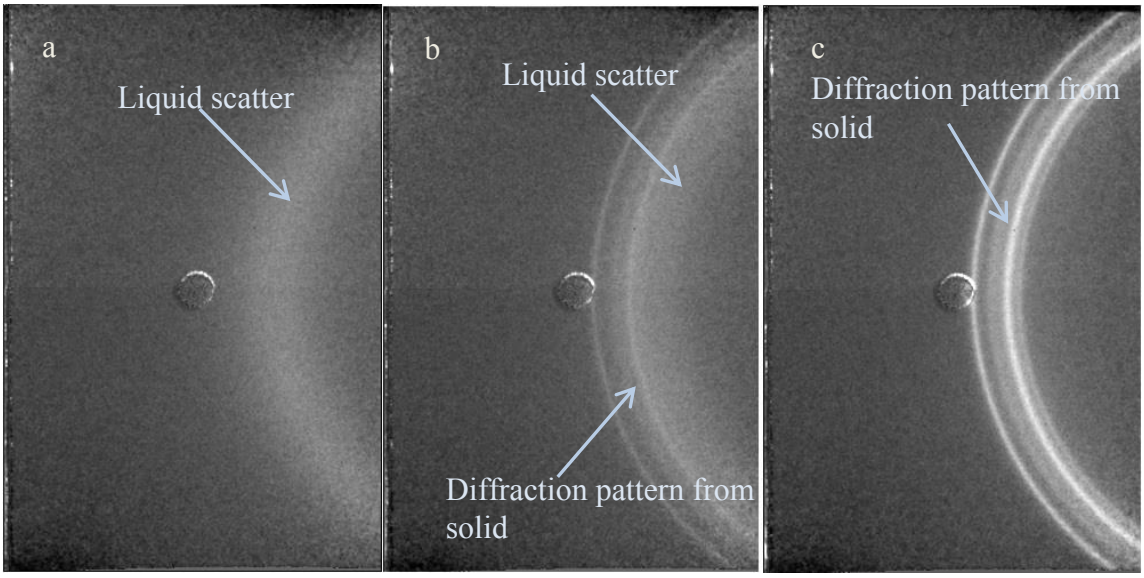

Figure 7-4. WAXS/WAXD patterns captured during the progress of a crystallization experiment. (a.) A scatter pattern from a TAG system that is completely liquid. (b.) A partially crystalline system showing both liquid scatter pattern and diffraction patterns from crystalline TAGs. (c.) A WAXD pattern from an almost completely crystalline system.

The area under the liquid scatter peak depends mainly on the degree of crystallinity of the system and to a lesser extent on the temperature and on the composition of the liquid. An increase in the solid fraction will cause a decrease in the liquid scatter area. With proper calibration, this liquid scatter area could be used to estimate the solid fraction of a crystallizing TAG system.

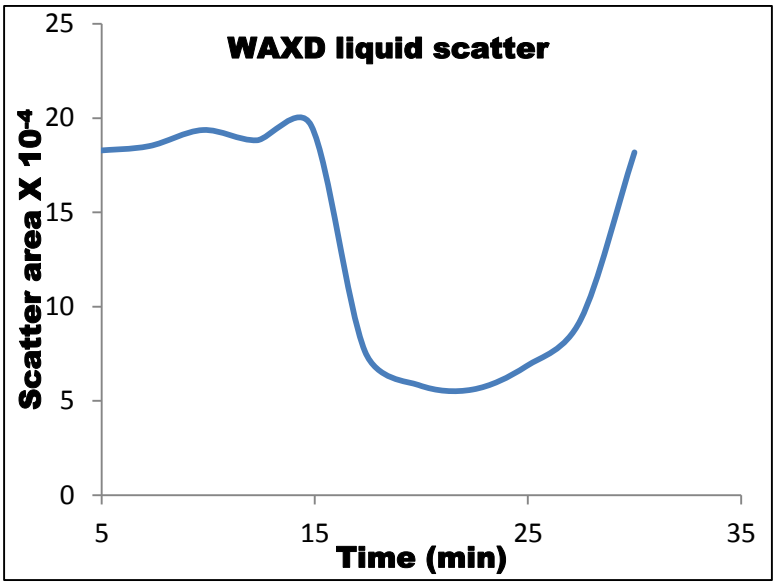

Figure 7-5. Change in the scatter area of a wide angle liquid peak with time during the experiment performed with the sample 5L5M crystallized at 26°C

7.4 Presence of two broad wide angle peaks in a partially crystalline system

A broader peak often corresponds to scattering rather than diffraction of x-rays. i.e., it represents a system where the molecules are not arranged in a layered fashion. Thus, in a TAG system, a broader peak corresponds to liquid while a sharper peak corresponds to a solid phase. Peak fittings of patterns obtained from a partially crystalline system like Figure 7-4-b sometimes showed the presence of two broad peaks. An example of patterns obtained at crystallization and melting containing two broad liquid peaks are shown in Figure 7-6 and Figure 7-7. However, the presence of two liquid peaks during crystallization is more pronounced than during melting in most of the experiments. This phenomenon is probably due to experimental limitations rather than the intrinsic behavior of the system (very long acquisition time of 2.5 minutes and due to very fast heating rate).

The presence of two liquid peaks during crystallization probably points towards two liquid phases (phase separation or interfacial liquid as discussed in Chapter 6).

TAG crystals are anisotropic in nature. This anisotropy is not confined to arrangement alone but also the resultant forces that are holding the crystal in each direction. Figure 7-1 and Figure 7-3 clearly point out that the affect of temperature on the

arrangement of molecules does not stay the same in all directions. This is a clear indication of different resultant force in each direction of a crystal. As a result, the broader peaks present in the WAXD pattern during the melting of a crystal might also be due to the less ordered arrangement in that particular direction where the molecules were held with a weaker force. Multiple experiments with high time reslution in WAXD should be performed to differentiate between the two possibilities for the cause of broad WAXD patterns. The change of peak positions of these broad WAXD patterns with time might provide a clue to confirm either of the two possibilities.

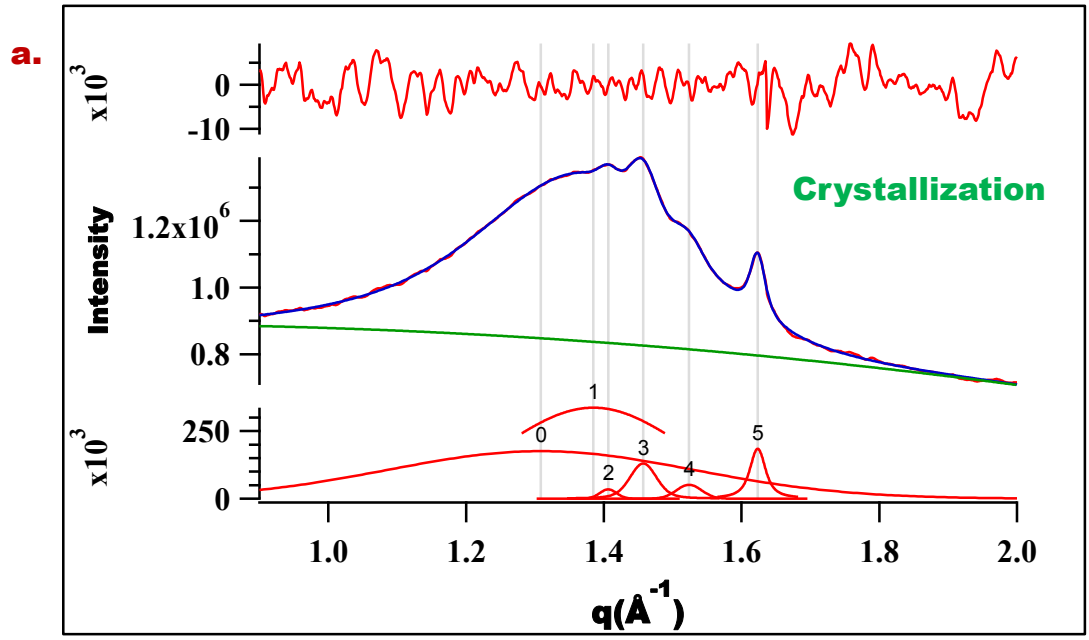

Figure 7-6. Presence of two broad liquid-like wide angle diffraction/scattering peaks at the beginning of crystallization of 5L5M at 30°C.

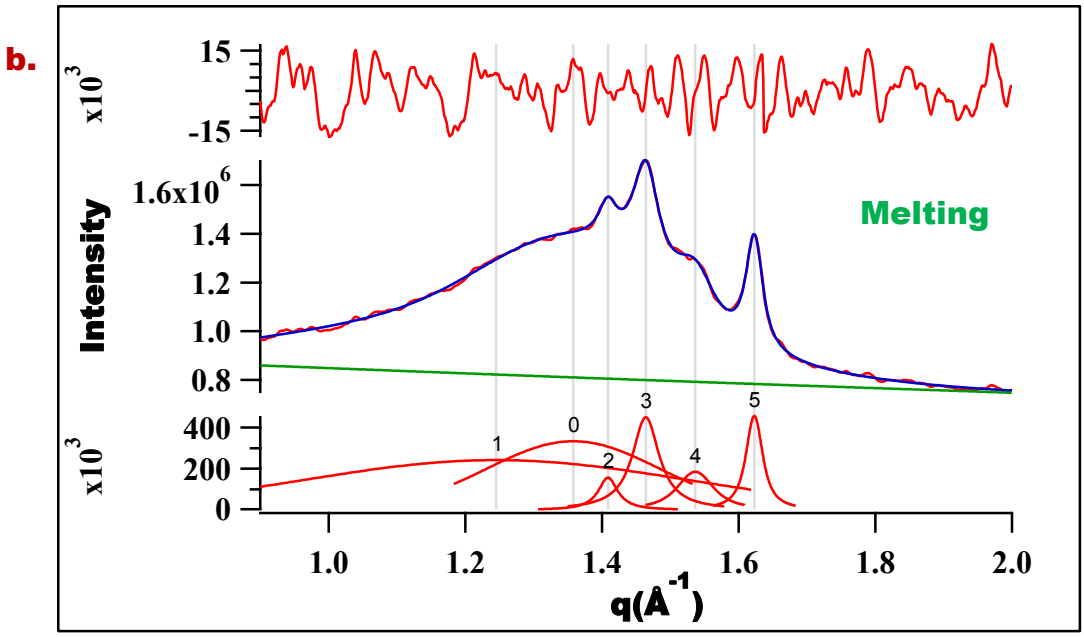

Figure 7-7. Presence of two broad liquid-like wide angle diffraction/scattering peaks during the melting of 5L5M at 26°C.

7.5 A proposed method to estimate lattice distortion using WAXD

A dissimilar molecule introduced into another pure crystal causes distortion of the crystal. (Marangoni & Wesdorp, 2012). (Kitaigorodsky, 1973; Kitaigorodsky, 1984) proposed a parameter called degree of isomorphism (ϵ) that can be used to estimate the activity in a mixed crystal based on the geometrical dissimilarities between molecules. The lattice distortion caused by the introduction of this dissimilar molecule is related to the excess Gibbs energy of mixing of these two components. The change in the correlation lengths in any direction of the crystalline phases due to changes in composition shown in Figure 7-3 at a particular temperature could be an indication of the lattice distortion caused due to an increase in the concentration of a particular component in the mixed phase and hence could be used as an alternative method to quantify excess Gibbs energy of mixing.

7.6 Correlation lengths and defects in a crystalline system

WAXD patterns give information about the distance between all the planes that are arranged in a repeating fashion in the lateral direction of a crystalline phase. In the case of our crystalline system, the four peaks (for example as seen in Figure 7-2) correspond to four distinct set of repating planes in the crystalline system. Although the average distance between these repetitive planes in a TAG crystal is known, the exact set of physical planes they correspond to is not known. An extensive study to identify different planes in a β crystal of tricaprin was performed by (Jensen & Mabis, 1966) but no such studies were performed to understand the structure of a β' modification.

As the aspect ratio of a crystallite stays constant (Acevedo & Marangoni, 2010), at any point during crystallization, using the thickness of a crystalline phase in SAXD direction, the corresponding average length and bredth (if thickness corresponds to the z-axis of a crystallite, length and breadth correspond to the x and y axis) can be calculated using the constant aspect ratio. If a better understanding of the spacings with respect to their corresponding direction can be obtained, the correlation lengths in each direction can be used to quantify the average number of defects on the crystal surface. As BCF theory states that the defects/dislocations on a crystal surface affect the growth rate of a crystal by providing sites of nucleation, with proper optimization, the correlation lengths could be used to predict the growth rate of a crystalline system.

Chapter 8 SUMMARY AND CONCLUSIONS

For the first time, the LKS model was evaluated against experimental data. Its ability to describe the formation of a crystalline phase(s) from a liquid of known composition at non-equilibrium conditions was tested using the instantaneous compositions of crystallizing phases and their corresponding liquid composition. Although the LKS model failed to provide a set of parameters that would explain the formation of two crystalline phases with instantaneous compositions from their corresponding liquid compositions, it was able to describe the formation of one of the crystalline phases. One of the possibility for the discrepancy could be due to limitations in the three suffix Margules equation to explain the activity of each component in each of the phases present in the system. The set of estimated interaction parameters also produced an equilibrium phase diagram that is physically impossible. Probably, the distortion to the equilibrium phase diagram when the system is undercooled converts it into a plausible kinetic phase diagram. Alternative models to describe the excess energies of mixing (thereby describing the activity of a component in a phase) like Van Laar, Wilson or UNIQUAC, may be tested to see if they can describe the system better.

The assumption that formation of both crystalline phases takes place from a single homogeneous liquid phase might be another cause for discrepancy. Due to very small diffusion coefficient in liquid TAGs (see section 6.4), there is a chance that at any point in time, a solid material being crystallized might be formed from the local concentration of liquid present in the vicinity of an existing solid material rather than from the bulk liquid composition. An increase in the distance between the local liquid from the bulk liquid (concentration gradient), should cause an increase in deviations in the LKS model if the homogeneity in the liquid phase is the only source of discrepancy. Crystallization under shear is known to produce smaller agglomerates due to continuous breaking of larger clusters (Mazzanti et al., 2003; Mazzanti et al., 2005). For two different crystalline systems with the same amount of total solid content, a system that is formed under the influence of shear will have smaller agglomerates and thus having a much homogenous distribution of components in the liquid phase when compared to a system being crystallized in the absence of shear. This distribution effectively decreases

the distance (or concentration gradient) between the local concentration of liquid in the vicinity of a growing crystalline phase and the bulk liquid concentration that is calculated using mass balance. If the LKS model produces a better fit when applied to a sheared system, it will act as supporting evidence of non-homogeneity in the liquid phase. A better method should be developed to quantify the change in the composition of the liquid at the vicinity of a growing crystalline phase. The amount of interfacial liquid also depends on the collective size of crystallites growing in a system. Measuring the amount and composition of this liquid is extremely difficult. Methods to estimate the size distribution of the crystallites and their clusters could help understanding the system better (Peyronel et al., 2013).

A reliable method to estimate the experimental composition of a crystalline phase is required to test any theoretical method that would predict the formation of crystalline phases either at equilibrium or non-equilibrium conditions. A correlation to estimate the composition of a crystalline phase made up of trilaurin and trimyristin from its d-spacing was initially developed by Anom (2009). In the presented study, the correlation was modified and improved to reliably estimate the composition of phases crystallized in the polymorphic form β' using a set of d-spacings and areas of crystalline phases obtained from various binary mixtures of trilaurin with trimyristin completely crystallized at different temperatures. This relationship is non-linear, likely due to slight changes in the sub-cell packing as the composition of a phase changes. The 95% confidence intervals of the parameters that describe this relationship, estimated using a Monte Carlo method, are rather narrow. The correlation between d-spacing and composition is complemented with another correlation that describes the relationship between the proportionality factor and d-spacing of a phase. For all the experiments, the composition and mass fraction of each crystalline phase were estimated using these relationships at any point in time.

Two crystalline phases were formed from each sample in most of the cases irrespective of crystallization temperature. These phases showed a greater dependence on the composition of the liquid from which they crystallized than on the crystallization temperature. In most cases, both crystalline phases formed had a higher d-spacing at the beginning and they gradually decreased as crystallization proceeded. Therefore, the concentration of trilaurin in the crystalline phase increases with time. The increase in the

mass of most crystalline phases is monotonic, while melt-mediated and interface mediated phase transformations seem to happen in other cases, such as in 5L5M. This study also reconfirmed that there is a limit to the maximum crystalline nanoplatelet thickness of TAG solids.

The change in d-spacing over time indicates non-homogeneity in TAG crystalline phases. Either the nanoplatelets have a continuous concentration gradient along their growth axes, or crystals of a 'family' grow sequentaially with different compositions. (See sections 6.4 and 2.1.5.3 for detailed explanation). The composition of the solid material that is deposited at any point of time (instantaneous composition) was calculated using a conservation of mass approach and the composition of the remaining liquid phase was calculated using a mass balance approach.

Even after the application of a correction factor for the discrepancies between capillaries due to size, position etc.,, differences in the total diffraction area of crystalline phases was observed within replicate experiments. These differences could be due to factors like formation of gaps in the crystallizing material. As the composition of liquid phase is calculated using mass balance, a chance exists that an error in the amount of a solid phase produces an error in the composition of the liquid phase. Availability of simultaneous SFC data at any point during crystallization would give a better confidence in the amounts of the solid crystalline phases calculated, thus making the balance to find the compositions more reliable.

Additionally, simultaneous WAXD patterns obtained during the crystallization process confirmed that all the crystalline phases formed at different temperatures belong to the polymorphic form β'. However, these patterns could be grouped into two categories based on their appearance. Patterns with sharp peaks were obtained from samples rich in trilaurin while samples rich in trimyristin produced much broader peaks. For the patterns obtained from a single sample, the broadness of these peaks also depended on the crystallization temperature. Phases obtained at higher temperatures (slow growth) had much sharper corresponding WAXD patterns. This observation gave rise to two possibilities, either the shape of peaks in WAXD patterns correspond to a sub-poymorphic form or the consistant spacing between consecutive layers in the crystalline phases.

BIBLIOGRAPHY

Acevedo, N. C., & Marangoni, A. G. (2010). Characterization of the nanoscale in triacylglycerol crystal networks. Crystal growth & design, 10(8), 3327-3333.

Anom, E. Y. (2009). Comparison of the theoretical and experimental composition of crystallizing lipid mixtures. (Master of Science Masters Thesis), Dalhousie University, Halifax.

Avrami, M. (1939). Kinetics of phase change. I General theory. The Journal of Chemical Physics, 7(12), 1103-1112.

Avrami, M. (1940). Kinetics of phase change. II transformation-time relations for random distribution of nuclei. The Journal of Chemical Physics, 8(2), 212-224.

Avrami, M. (1941). Granulation, phase change, and microstructure kinetics of phase change. III. The Journal of Chemical Physics, 9(2), 177-184.

Bailey, A. E. (1964). Bailey's Industrial Oil and Fat Products: John Wiley & Sons.

Bunker, G. (2010). Introduction to XAFS: a practical guide to X-ray absorption fine structure spectroscopy: Cambridge University Press.

Burton, W.-K., Cabrera, N., & Frank, F. (1951). The growth of crystals and the equilibrium structure of their surfaces. Philosophical Transactions of the Royal Society of London. Series A, Mathematical and Physical Sciences, 299-358.

Christie, W. W. (2010). Lipid Analysis, Isolation, Separation, Identification and Lipidomic Analysis (4th ed.). Bridgewater, U.K: Oily Press.

Cisneros, A., Mazzanti, G., Campos, R., & Marangoni, A. G. (2006). Polymorphic transformation in mixtures of high-and low-melting fractions of milk fat. Journal of agricultural and food chemistry, 54(16), 6030-6033.

Clarkson, C. E., & Malkin, T. (1934). 139. Alternation in long-chain compounds. Part II. An x-ray and thermal investigation of the triglycerides. Journal of the Chemical Society (Resumed), 666-671.

Cullity, B. D. (1957). Elements of X-ray Diffraction. American Journal of Physics, 25, 394-395.

Erofe'ev, B. (1946). Generalized equation of chemical kinetics and its application in reactions involving solids. Comptes rendus de l'Académie des sciences de l'URSS, 52, 511-514.

Foubert, I., Vanrolleghem, P. A., Vanhoutte, B., & Dewettinck, K. (2002). Dynamic mathematical model of the crystallization kinetics of fats. Food research international, 35(10), 945-956.

Garside, J. (1987). General principles of crystallization. Food structure and behaviour/edited by JMV Blanshard and P. Lillford.

Garti, N., & Sato, K. (1988). Crystallization and Polymorphism of Fats and Fatty acids (Vol. 31): M. Dekker.

Goto, M., Kodali, D., Small, D., Honda, K., Kozawa, K., & Uchida, T. (1992). Single crystal structure of a mixed-chain triacylglycerol: 1, 2-dipalmitoyl-3-acetyl-sn-glycerol. Proceedings of the National Academy of Sciences, 89(17), 8083-8086.

Hagemann, J., & Rothfus, J. (1983). Polymorphism and transformation energetics of saturated monoacid triglycerides from differential scanning calorimetry and theoretical modeling. Journal of the American Oil Chemists' Society, 60(6), 1123-1131.

Higami, M., Ueno, S., Segawa, T., Iwanami, K., & Sato, K. (2003). Simultaneous synchrotron radiation X-ray diffraction-DSC analysis of melting and crystallization behavior of trilauroylglycerol in nanoparticles of oil-in-water emulsion. Journal of the American Oil Chemists' Society, 80(8), 731-739.

Hilditch, T. P., & Williams, P. N. (1964). The chemical constitution of natural fats. The chemical constitution of natural fats.(4th edition).

Himawan, C., Starov, V., & Stapley, A. (2006). Thermodynamic and kinetic aspects of fat crystallization. Advances in colloid and interface science, 122(1), 3-33.

Hoerr, C. (1964). X-ray diffraction of fats. Journal of the American Oil Chemists' Society, 41(7), A4-A34.

Jensen, L., & Mabis, A. (1966). Refinement of the structure of-tricaprin. Acta crystallographica, 21(5), 770-781.

Johnson, W. A., & Mehl, R. F. (1939). Reaction kinetics in processes of nucleation and growth. Transactions of the Metallurgical Society of AIME, 135(8), 396-415.

Kellens, M., Meeussen, W., Hammersley, A., & Reynaers, H. (1991). Synchrotron radiation investigations of the polymorphic transitions in saturated monoacid triglycerides. Part 2: Polymorphism study of a 50: 50 mixture of tripalmitin and tristearin during crystallization and melting. Chemistry and physics of lipids, 58(1), 145-158.

Kellens, M., Meeussen, W., Riekel, C., & Reynaers, H. (1990). Time resolved X-ray diffraction studies of the polymorphic behaviour of tripalmitin using synchrotron radiation. Chemistry and physics of lipids, 52(2), 79-98.

Kellens, M., & Reynaers, H. (1992). Study of the polymorphism of saturated monoacid triglycerides II: polymorphic behaviour of a 50/50 mixture of tripalmitin and tristearin. European Journal of Lipid Science and Technology, 94(8), 286-293.

Kitaigorodsky, A. (1973). Molecular crystals and molecules. Academic Press INC, New York.

Kitaigorodsky, A. I. (1984). Mixed crystals: Springer.

Kloek, W., Walstra, P., & van Vliet, T. (2000). Crystallization kinetics of fully hydrogenated palm oil in sunflower oil mixtures. Journal of the American Oil Chemists' Society, 77(4), 389-398.

Kobayashi, M. (1988). Vibrational spectroscopic aspects of polymorphism and phase transition of fats and fatty acids. Crystallization and Polymorphism of Fats and Fatty Acids, 139-187.

Kolmogorov, A. N. (1937). On the statistical theory of the crystallization of metals. Bulletin of the Academy of Sciences of the USSR Division, Math. Ser, 1, 355-359.

Kurz, W., & Fisher, D. J. (1986). Fundamentals of solidification. Trans Tech Publications Ltd, Trans Tech House, 4711, Aedermannsdorf, Switzerland, 1986. 244.

Larsson, K. (1966). Classification of glyceride crystal forms. Acta Chemica Scandinavica, 20(8), 2255-2260.

Lopez, C., Lavigne, F., Lesieur, P., Bourgaux, C., & Ollivon, M. (2001). Thermal and structural behavior of milk fat. 1. Unstable species of anhydrous milk fat. Journal of dairy science, 84(4), 756-766.

Lopez, C., Lesieur, P., Keller, G., & Ollivon, M. (2000). Thermal and structural behavior of milk fat: 1. Unstable species of cream. Journal of colloid and interface science, 229(1), 62-71.

Los, J., & Flöter, E. (1999). Construction of kinetic phase diagrams. Physical Chemistry Chemical Physics, 1(18), 4251-4257.

Los, J. H., van Enckevort, W. J., Vlieg, E., & Flöter, E. (2002). Metastable States in Multicomponent Liquid-Solid Systems I: A Kinetic Crystallization Model. The Journal of Physical Chemistry B, 106(29), 7321-7330.

Lutton, E. (1945). The polymorphism of tristearin and some of its homologs. Journal of the American Chemical Society, 67(4), 524-527.

Lutton, E., & Fehl, A. (1970). The polymorphism of odd and even saturated single acid triglycerides, C8–C22. Lipids, 5(1), 90-99.

MacLean, D. A. (2012). An NMR study of diffusion in surfactant-free emulsions and molten triglyceride mixtures.

Marangoni, A., & Hartel, R. (1998). Visualization and structural analysis of fat crystal networks. Food technology (USA).

Marangoni, A. G., & Wesdorp, L. H. (2012). Structure and properties of fat crystal networks: CRC Press.

Margules, M. (1895). Über die Zusammensetzung der gesättigten Dämpfe von Mischungen. Sitzungsber. Akad. Wiss. Wien, math.-naturwiss. Klasse, 104, 1243-1278.

Martini, S., & Herrera, M. (2002). X-Ray diffraction and crystal size. Journal of the American Oil Chemists' Society, 79(3), 315-316.

Mazzanti, G. (2004). X-ray diffraction study on the crystallization of fats under shear. (Doctor of Philosophy Doctoral), The University of Guelph, Guelph.

Mazzanti, G., Guthrie, S. E., Marangoni, A. G., & Idziak, S. H. (2007). A conceptual model for shear-induced phase behavior in crystallizing cocoa butter. Crystal growth & design, 7(7), 1230-1241.

Mazzanti, G., Guthrie, S. E., Sirota, E. B., Marangoni, A. G., & Idziak, S. H. (2003). Orientation and phase transitions of fat crystals under shear. Crystal growth & design, 3(5), 721-725.

Mazzanti, G., Guthrie, S. E., Sirota, E. B., Marangoni, A. G., & Idziak, S. H. (2004a). Effect of minor components and temperature profiles on polymorphism in milk fat. Crystal growth & design, 4(6), 1303-1309.

Mazzanti, G., Guthrie, S. E., Sirota, E. B., Marangoni, A. G., & Idziak, S. H. (2004b). Novel shear-induced phases in cocoa butter. Crystal growth & design, 4(3), 409-411.

Mazzanti, G., Marangoni, A., Guthrie, S., Idziak, S., Sirota, E., & Dutcher, J. (2005). Crystallization of bulk fats under shear. Soft materials: structure and dynamics, 279-297.

Mazzanti, G., Marangoni, A., & Idziak, S. (2008). Modeling of a two-regime crystallization in a multicomponent lipid system under shear flow. The European Physical Journal E, 27(2), 135-144.

Mazzanti, G., & Mudge, E. M. (2009). Development of a rheo-NMR system to study the crystallisation of bulk lipids under shear flow. Magnetic Resonance in Food Science: Challenges in a Changing World, Reykjavik, Iceland, 2008.

Minato, A., Ueno, S., Yano, J., Wang, Z., Seto, H., Amemiya, Y., & Sato, K. (1996). Synchrotron radiation X-ray diffraction study on phase behavior of PPP-POP binary mixtures. Journal of the American Oil Chemists' Society, 73(11), 1567-1572.

Mullin, J. W. (2001). Crystallization: Butterworth-Heinemann.

Narine, S. S., & Marangoni, A. G. (1999). Relating structure of fat crystal networks to mechanical properties: a review. Food research international, 32(4), 227-248.

PadIey, F. B. (1997). Chocolate and confectionery fats. Lipid technologies and applications, 391.

Peyronel, F., Ilavsky, J., Mazzanti, G., Marangoni, A. G., & Pink, D. A. (2013). Edible oil structures at low and intermediate concentrations. II. Ultra-small angle X-ray scattering of in situ tristearin solids in triolein. Journal of Applied Physics, 114(23), 234902.

Rasband, W. S. (1997-2014). ImageJ, U. S from http://imagej.nih.gov/ij/

Rousset, P., & Rappaz, M. (1997). α-Melt-mediated crystallization of 1-palmitoyl-2-oleoyl-3-stearoyl-sn-glycerol. Journal of the American Oil Chemists' Society, 74(6), 693-697.

Rousset, P., Rappaz, M., & Minner, E. (1998). Polymorphism and solidification kinetics of the binary system POS-SOS. Journal of the American Oil Chemists' Society, 75(7), 857-864.

Sato, K. (1993). Polymorphic transformations in crystal growth. Journal of Physics D: Applied Physics, 26(8B), B77.

Sato, K. (1999). Solidification and phase transformation behaviour of food fats—a review. European Journal of Lipid Science and Technology, 101(12), 467-474.

Sato, K., & Kuroda, T. (1987). Kinetics of melt crystallization and transformation of tripalmitin polymorphs. Journal of the American Oil Chemists' Society, 64(1), 124-127.

Schenk, H., & Peschar, R. (2004). Understanding the structure of chocolate. Radiation physics and chemistry, 71(3), 829-835.

Sonoda, T., Takata, Y., Ueno, S., & Sato, K. (2004). DSC and synchrotron-radiation X-ray diffraction studies on crystallization and polymorphic behavior of palm stearin in bulk and oil-in-water emulsion states. Journal of the American Oil Chemists' Society, 81(4), 365-373.

Takeuchi, M., Ueno, S., & Sato, K. (2003). Synchrotron radiation SAXS/WAXS study of polymorph-dependent phase behavior of binary mixtures of saturated monoacid triacylglycerols. Crystal growth & design, 3(3), 369-374.

Tolman, R. C. (1925). The principle of microscopic reversibility. Proceedings of the National Academy of Sciences of the United States of America, 11(7), 436.

Ueno, S., Minato, A., Seto, H., Amemiya, Y., & Sato, K. (1997). Synchrotron radiation X-ray diffraction study of liquid crystal formation and polymorphic crystallization of SOS (sn-1, 3-distearoyl-2-oleoyl glycerol). The Journal of Physical Chemistry B, 101(35), 6847-6854.

van Malssen, K., van Langevelde, A., Peschar, R., & Schenk, H. (1999). Phase behavior and extended phase scheme of static cocoa butter investigated with real-time X-ray powder diffraction. Journal of the American Oil Chemists' Society, 76(6), 669-676.

Wentzell, P. D. (2014). Measurement errors in multivariate chemical data. Journal of the Brazilian Chemical Society, 25(2), 183-196.

Wesdorp, L. H. (1990). Liquid - multiple solid phase equilibria in fats: Theory and experiments : Evenwichten tussen een vloeibare en verscheidene vaste fasen in spijsvetten: Theorie en experimenten. (Doctoral thesis Doctoral), TU Delft, Delft University of Technology.

Widlak, N., Hartel, R. W., & Narine, S. (2001). Crystallization and solidification properties of lipids: The American Oil Chemists Society.

Zhang, L., Ueno, S., Miura, S., & Sato, K. (2007). Binary phase behavior of 1, 3-dipalmitoyl-2-oleoyl-sn-glycerol and 1, 2-dioleoyl-3-palmitoyl-rac-glycerol. Journal of the American Oil Chemists' Society, 84(3), 219-227.

Appendix - A Acid catalyzed transesterification for the conversion of TAGs into their respective fatty acid methyl esters(FAME)

Preparation of Hildich reagent: About 1.5 mL of sulfuric acid was added to 100 mL of methanol that was dried using excess anhydrous sodium sulfate (Hilditch & Williams, 1964).

10 µL of each sample is measured using 'wiretrol' and added into a test tube. 3mL of Hilditch reagent and 1.5 mL of dichloromethane containing 0.01% BHT were added to the test tube. The test tube was flushed with nitrogen, tightly capped and then set on a heating block for 1 hour for the transesterification reaction to happen. The reaction products were allowed to cool down before adding 1.0 mL of distilled water and 3.0 mL of hexane. The test tube was capped, vortexed and then centrifuged at 1640 rpm for 2 minutes. The hexane layer was separated to another 10 mL test tube and again the extraction procedure was repeated twice by adding 1.0 mL of distilled water and 3.0 mL of hexane, followed by vortexing and centrifuging. The amount of FAME formed was measured by evaporating the pooled hexane in a water bath at 34 °C under a steady flow of nitrogen.

GC procedure:

Dried FAME samples were diluted to a concentration of 0.05mg/ml in hexane. 1.0 µl of this sample was injected into a Bruker Scion 436-GC instrument equipped with a FID detector, CP-8400 Autosampler and DB-23 high polarity column that is 30 m in length and has a diameter of 0.250 mm. This column is coated with a 0.25 µm film comprised of 50% cyanopropyl polysiloxane. The injected FAME sample was held at 250 °C before entering the gas phase. The sample was then carried into the column by a helium gas stream at a flow rate of 100 ml/min. The temperature profile inside the column is divided into three stages. In the initial stage, the temperature was held constant at 153 °C for 2 minutes. The temperature was increased to 174 °C at a heating ramp from 2.3 °C/min and held for 0.20 minutes in the second stage. In the third stage, the

temperature was again increased at a rate of 2.5 °C/min to a final temperature of 205 °C and was held for 11 minutes. The detector was held at 270 °C (Budge et al., 2006).

Analysis of GC results:

The identification of the methyl ester of a fatty acid was done by comparing the peak positions of different FAMEs obtained from Menhaden fish oil standard that was analyzed at the same conditions as the test sample. As the area under the peak of a chromatogram is related to the mass of its respective FAME, the amount of trilaurin and trimyristin present in a sample were simply their corresponding area fractions.

Appendix - B Synchrotron facility

A synchrotron facility for the production of x-rays has mainly 4 sections:

a. LINAC and booster rings: LINAC is an acronym for linear accelerator which brings electrons from rest to motion. These accelerated electrons enter smaller diameter rings called booster rings in which electrons are further accelerated closer to speed of light and are then transferred to storage rings. The acceleration is achieved generally by a combination of varying magnetic and electric fields with space and time and this variation depends on the type of synchrotron.
b. Storage rings: Storage rings are generally higher diameter rings in which the speeding electrons coming from booster rings are stabilized and maintained.
c. Bending magnets / Insertion devices: Bending magnets and insertion devices are sections in the storage rings which are activated after the energy of the electrons in the storage ring is stable. These bending magnets/ Insertion devices change the direction of the fast moving electrons. In this process of changing direction these electrons lose energy. This energy is then emitted in the form of x-rays. Insertion devices are a series of bending magnets used to increase the intensity of x-rays being produced.
d. Beamlines: The x-rays which are produced at these bending magnets/ Insertion devices are led through waveguides and pass through monochromators before being used at beamlines.

Appendix - C Processing acquired data

a. Unwarping

The 'Bruker' 2D detector set up to capture SAXD patterns in the beamline hutch at the synchrotron detects an x-ray photon through a photochemical interaction. This detector has a phosphor plate installed on its surface. Light is produced when an x-ray falls on this plate of phosphor. This camera consists of a bundle of fiber optic cables through which a photon corresponding to a particular position is transmitted to a CCD chip which saves the image. The transmission of light corresponding to different coordinates through a tapered bundle causes distortion in the image. A process called 'unwarping' has to be performed on these distorted images to correct the position and intensity corresponding to the misplaced pixels. This process of unwarping is done through a dedicated routine available in Bruker's 'SMART' software.

b. Filtering:

The surface of the 2D detector is not perfect. Some of the pixels malfunction over time. These bad pixels tend to record erroneous values for intensity. By looking at different diffraction patterns produced over time, bad pixels were identified manually. The process of fixing these bad pixels is termed as filtering. A program was written to take an average intensity of 8 pixels around these defective pixels and substitute this value for the value recorded by the defective pixel.

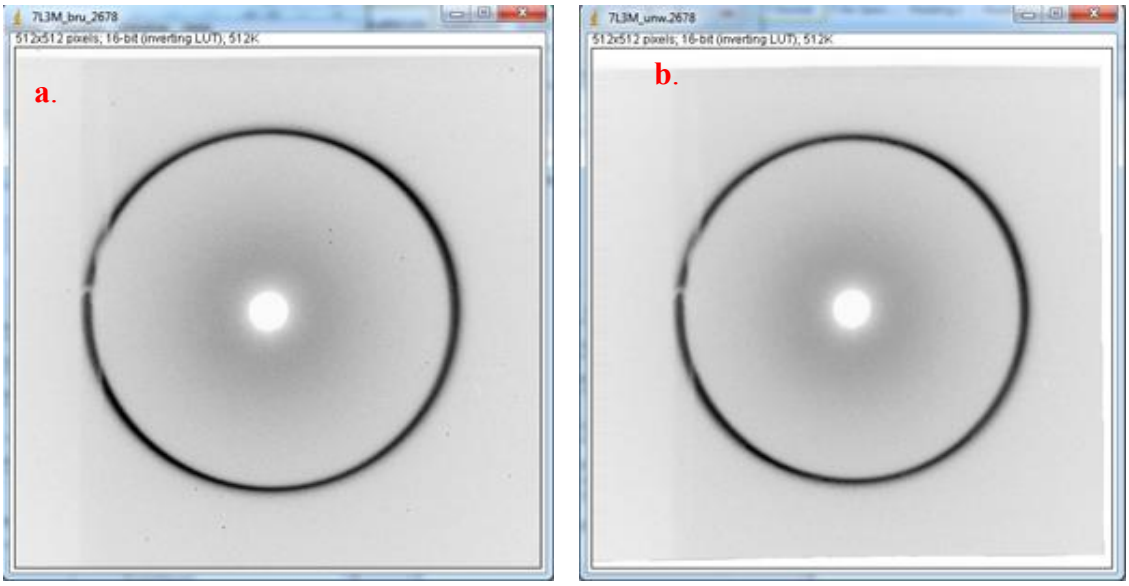

Figure A-C-0-1. (a.) raw diffraction pattern obtained, (b.) diffraction pattern after the process of unwarping and filtering

c. ImageJ plug-in for analyzing XRD patterns

ImageJ is a public domain, open source Java based image processing software (Rasband, 1997-2014). This program has many routines written to perform various actions required for image analysis and processing. It also allows users to write custom macros and plugins for image analysis using these existing routines. A custom plugin called XR2D was developed by Dr. Gianfranco Mazzanti with the assistance of Maochen Hannah Wang and Kisun Park from University of Waterloo in 2003. This plugin is used to perform multiple operations like filtering, centering, creation of radial plots, azimuthal plots etc., on the images captured at BNL.

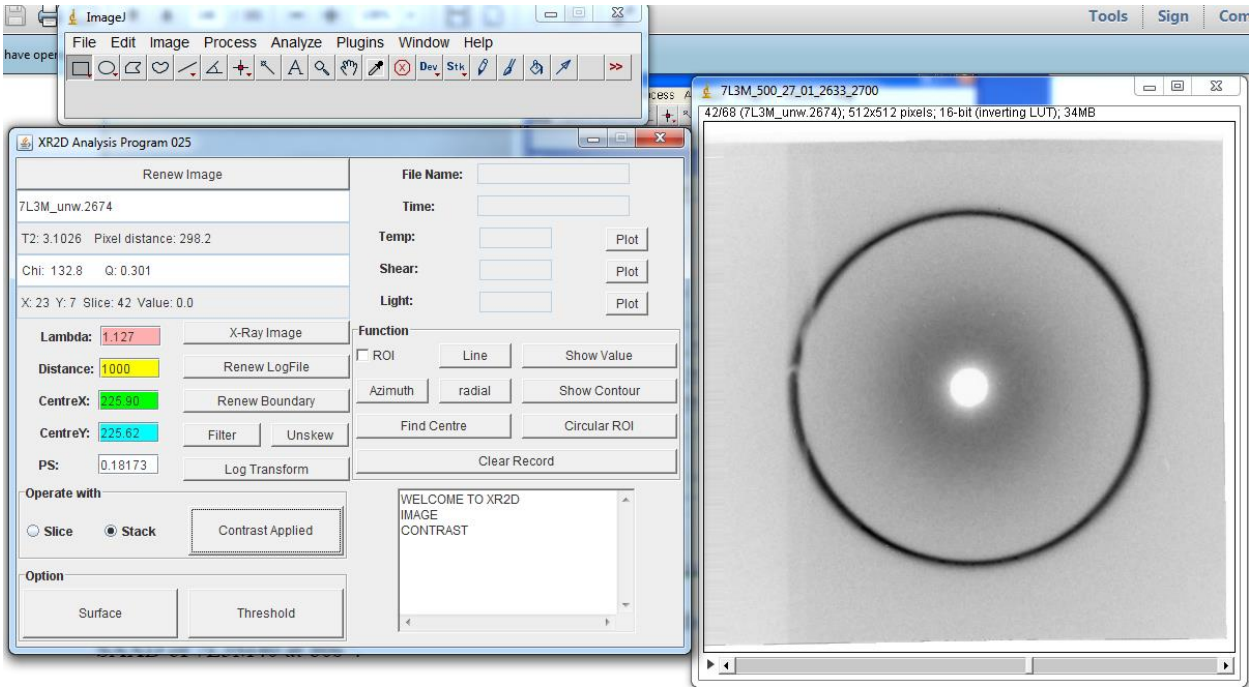

Figure A-C-0-2. ImageJ along with XR2D interface, an example diffraction pattern captured at BNL opened using this XR2D plugin

d. Opening of diffraction patterns

A plugin called XR2D (Shown in Figure A-C-0-2) is developed to process the acquired XRD patterns. A sub program called 'X-ray Image' is written and is incorporated in the XR2D main applet window. This program has the capability of reading different image formats in which different commercially available detectors save diffraction images like 'BS-IMAGE', 'APS-IMAGE' etc. The images saved by the Wide angle Laue camera are in 16-bit unsigned grey scale format and they can be opened directly by using the File → Open option available in the main ImageJ window.

e. Selecting the region of interest for analysis

XR2D plugin also provides a provision to select the region of interest for the analysis of a diffraction pattern. Sometimes, due to the limitations in the experimental set up, there might be a part or region in the diffraction pattern that could be rendered damaged. In such cases, XR2D panel has a program called 'ROIClass.java' which could

be called using the button ‘Renew Boundary’. This allows the user to select the region of interest and perform image analysis on this region alone.

f. Centering the diffraction patterns

After the region of interest is identified, centering of the image can be performed. Centering of a diffraction pattern is an extremely important operation to be performed as it effects greatly the interpretation of the d-spacing of the physical phases forming a diffraction pattern. This centering is performed by a sub program which can be called by the button ‘Find Center’. This program takes a range of q-values as inputs and then calculates the point with the brightest intensity within this range of q-values at every angle of a circle starting from 0 radians and completing a whole turn of 2π radians. The program then fits a circle into the array of these bright spots found. The center of the diffraction pattern is identified as the center of this fitted circle.

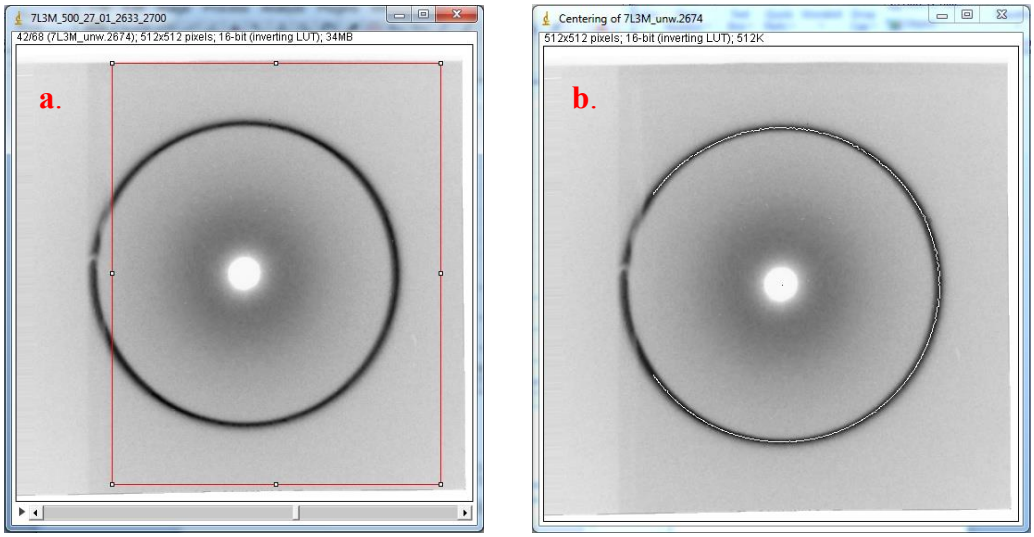

Figure A-C -0-3. (a.) a SAXD pattern opened using XR2D plugin and with a defined region of interest. (b.) A pattern after the centering program has been run. The white dots are the points identified to be the brightest within the specified q-range at every angle 'θ'. The black dot at the center is the center of all the bright spots found out.

g. Creating Radial plots

Radial plots are 2-dimensional plots representing the average change of x-ray intensity with a change in scattering vector q. Radial plots are created by taking a radial average of intensity at increasing value of q on a diffraction pattern. After the region of

interest has been identified and the centering of a diffraction pattern is performed, radial plots are created using the button called 'radial' on the XR2D Main panel. The pressing of this button calls a program called 'RadialAnalysisClass.java'. This program accepts an image with a valid region of interest, range of q-values and the starting and ending angle between which a radial plot is to be made. The program starts with the initial q-value specified, calculates the intensity along the perimeter of the circle with radius q, saves this value and then moves to the next q-value with a constant increment and continues this process until it reaches the final q-value specified. Finally, the program then returns a radial plot which is a compilation of these values. This program also has the capability of creating radial plots for specified ranges for a whole stack of images of interest.

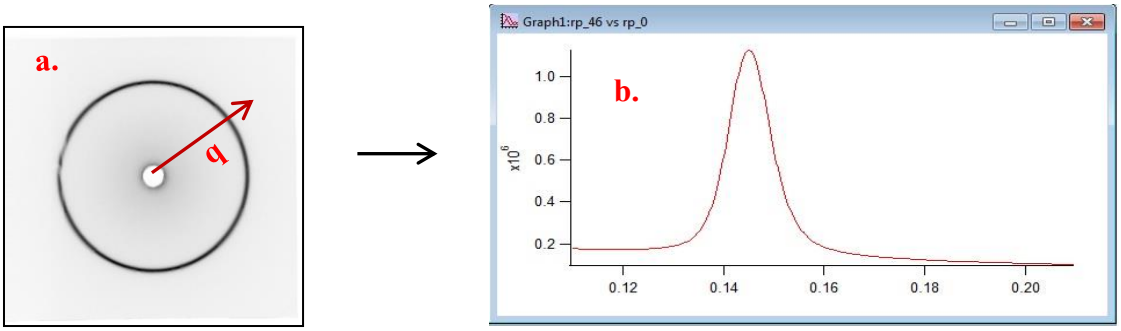

Figure A-C -0-4. Creation of radial plots from a Debye ring. (a.) A Debye ring showing the direction of scattering vector q, (b.) A radial plot created from this Debye ring showing the change of intensity along with the scattering vector q

e. Normalizing radial plots

The intensity/count of the x-rays produced from the synchrotron ring is not constant with time. The intensity of x-ray beam depends on the amount of electrons in the storage ring. The count of electrons in the ring tends to go down with time. The storage ring is refilled with electrons twice every day. As a result, the intensity of the x-rays produced is at its maximum during refill and decreases with time. This decrease in the intensity of x-rays being produced effects the diffraction patterns causing a reduction in their maximum amplitude and diffraction area making comparing two different diffraction patterns highly difficult. As a result, a normalization procedure is performed on the patterns captured at different times to bring their total diffraction area to a nominal value to facilitate comparison and quantification of diffraction patterns.

A normalization procedure is followed for each individual experiment. A Log file containing the time, temperature and the monitor value of x-rays(count of photons) of all the patterns in this experiment is created. A macro has been developed in imageJ to normalize radial plots that have been created earlier. This macro takes a log file and the corresponding set of radial plots of all the diffraction patterns in an experiment. It then picks the monitor value corresponding to a particular radial plot and then brings the value of each point in the radial plot to a set nominal value.

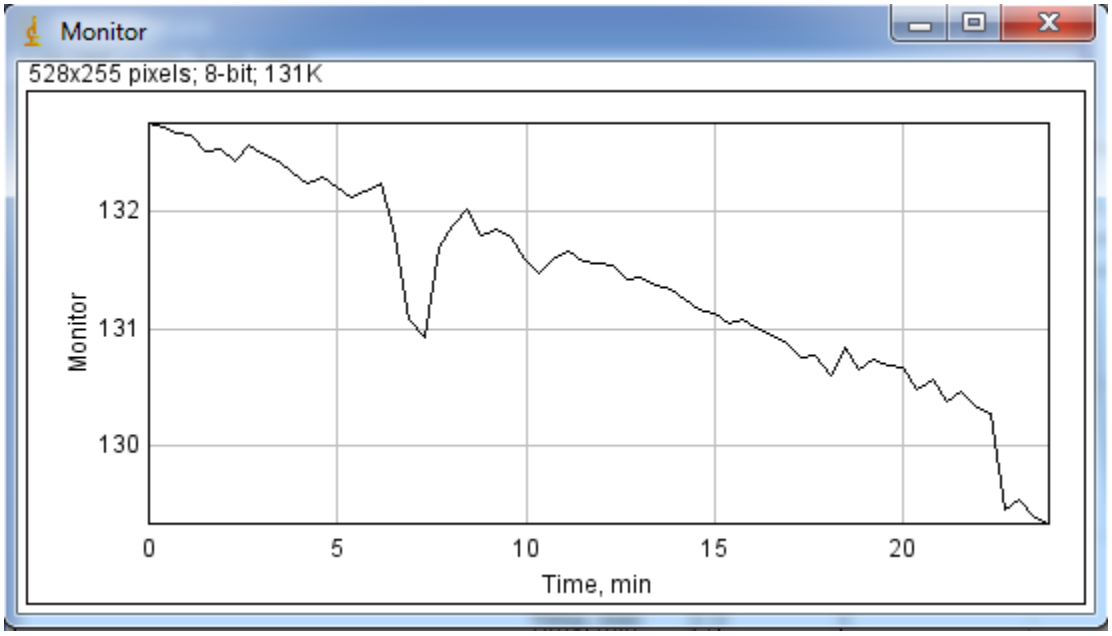

Figure A-C -0-5. A simple plot depicting the decrease in the number of x-rays hitting the sample with time

Appendix - D Igorpro Macro for the generation of random data set to perform Mone Carlo simulation

```
#pragma rtGlobals=3             // Use modern global access method and strict wave access.
#include <Global Fit 2>
Function RandomDataset(areas,stdevarea)
Wave areas, stdevarea
variable std, z
variable len = numpnts(areas)
for(z=0;z<=len;z+=1)
String Dataset_name
Dataset_name = "MCSet_d2_calc_" +num2str(z)
print Dataset_name
std = stdevarea[0]
Make/O/N=1000 Randomset1
Randomset1 = areas[z] + gnoise(std)
String testprint = "       "+num2str(z)+"      "+num2str(areas[z])+"       "+num2str(std)
print testprint
AppendToTable Randomset1
rename Randomset1 $Dataset_name
endfor
end
```

Appendix - E Excel VBA Macro to solve for a set of parameters that describes the relationship between d-spacing and composition using each correlated dataset

```
Sub Montecarlo_d2_sigma_calc_correlated()
      i = 0
      j = 0
      For i = 1 To 1000
         For j = 4 To 91
         k = j - 3
         Sheets("d-spacing-comp").Cells(j, 7).Value = Sheets("d2_calc").Cells(k, i).Value
         Sheets("d-spacing-comp").Cells(j, 16).Value =
Sheets("sigma_calc").Cells(k,i).Value
         Next j
         Worksheets("d-spacing-comp").Activate
         For l = 4 To 10
         m = l - 3
         Sheets("d-spacing-comp").Cells(l, 28).Value = Sheets("Initial_values").Cells(m,
1).Value
         Next l
         'Use Solver to find the solution
         SolverOk SetCell:="$AB$2", MaxMinVal:=2, ValueOf:=0,
ByChange:="$AB$4:$AB$9", _
      Engine:=1, EngineDesc:="GRG Nonlinear"
         SolverSolve UserFinish:=True 'Runs Solver without asking for user input
         SSE = Worksheets("d-spacing-comp").Range("AB2").Value
         ab2 = Worksheets("d-spacing-comp").Range("AB4").Value
         ab3 = Worksheets("d-spacing-comp").Range("AB5").Value
         psi_2 = Worksheets("d-spacing-comp").Range("AB6").Value
         psi_1 = Worksheets("d-spacing-comp").Range("AB7").Value
         dl = Worksheets("d-spacing-comp").Range("AB8").Value
         dm = Worksheets("d-spacing-comp").Range("AB9").Value

         Worksheets("Montecarlo_parameters").Range("C4").Offset(i, 0).Value = SSE
         Worksheets("Montecarlo_parameters").Range("D4").Offset(i, 0).Value = ab2
         Worksheets("Montecarlo_parameters").Range("E4").Offset(i, 0).Value = ab3
         Worksheets("Montecarlo_parameters").Range("F4").Offset(i, 0).Value = psi_2
         Worksheets("Montecarlo_parameters").Range("G4").Offset(i, 0).Value = psi_1
         Worksheets("Montecarlo_parameters").Range("H4").Offset(i, 0).Value = dl
         Worksheets("Montecarlo_parameters").Range("I4").Offset(i, 0).Value = dm
      Next i
End Sub
```

Appendix - F Permissions for copyrighted material used

License Details

Thank you very much for your order.

This is a License Agreement between Dalhousie university ("You") and Elsevier ("Elsevier"). The license consists of your order details, the terms and conditions provided by Elsevier, and the payment terms and conditions.

Get the printable license.

License Number	3437690346339
License date	Jul 28, 2014
Order Content Publisher	Elsevier
Order Content Publication	Advances in Colloid and Interface Science
Order Content Title	Thermodynamic and kinetic aspects of fat crystallization
Order Content Author	Victor M. Starov,Reinhard Miller,C. Himawan,V.M. Starov,A.G.F. Stapley
Order Content Date	25 September 2006
Licensed content volume number	122
Licensed content issue number	1-3
Number of pages	31
Type of Use	reuse in a thesis/dissertation
Portion	figures/tables/illustrations
Number of figures/tables/illustrations	1
Format	both print and electronic
Are you the author of this Elsevier article?	No
Will you be translating?	No
Title of your thesis/dissertation	ESTIMATING AND MODELLING THE COMPOSITIONS OF CRYSTALLIZING TRIGLYCERIDE BINARY MIXTURES USING X-RAY DIFFRACTION
Expected completion date	Aug 2014
Estimated size (number of pages)	145
Elsevier VAT number	GB 494 6272 12
Price	0.00 USD
VAT/Local Sales Tax	0.00 USD / 0.00 GBP
Total	**0.00 USD**

Back

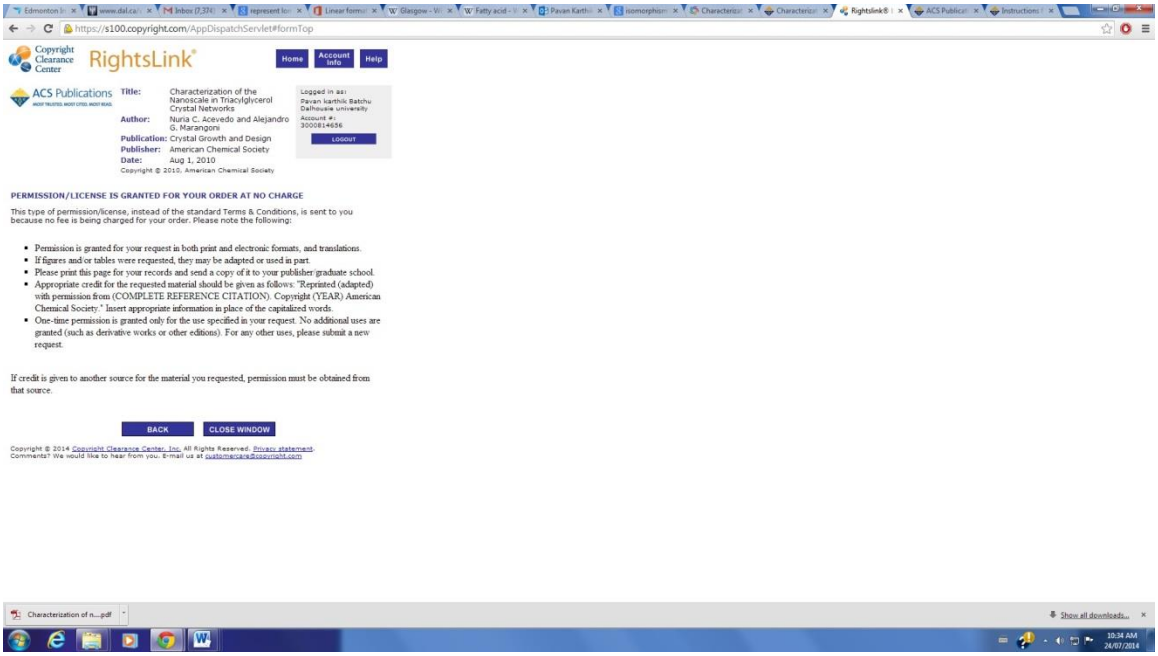

License Details

This is a License Agreement between Dalhousie university ("You") and John Wiley and Sons ("John Wiley and Sons"). The license consists of your order details, the terms and conditions provided by John Wiley and Sons, and the payment terms and conditions.

Get the printable license.

License Number	3437040836016
License date	Jul 27, 2014
Order Content Publisher	John Wiley and Sons
Order Content Publication	Wiley Books
Order Content Title	Bailey's Industrial Oil and Fat Products, Volume 1, Edible Oil and Fat Products: Chemistry, Properties, and Health Effects, 6th Edition
Book title	Bailey's Industrial Oil and Fat Products, Volume 1, Edible Oil and Fat Products: Chemistry, Properties, and Health Effects, 6th Edition
Licensed copyright line	Copyright © 2005, John Wiley and Sons
Order Content Author	Fereidoon Shahidi (Editor)
Order Content Date	Apr 1, 2005
Type of use	Dissertation/Thesis
Requestor type	University/Academic
Format	Print and electronic
Portion	Figure/table
Number of figures/tables	1
Original Wiley figure/table number(s)	Figure 3. Typical subcell structures of TAG polymorphs. The a, b0, and b forms have hexagonal (H), orthorhombic perpendicular ðO?Þ, and triclinic parallel(T//), respectively.
Will you be translating?	No
Title of your thesis / dissertation	ESTIMATING AND MODELLING THE COMPOSITIONS OF CRYSTALLIZING TRIGLYCERIDE BINARY MIXTURES USING X-RAY DIFFRACTION
Expected completion date	Aug 2014
Expected size (number of pages)	145
Total	**0.00 USD**

◂ Back

License Details

Thank you very much for your order.

This is a License Agreement between Dalhousie university ("You") and Elsevier ("Elsevier"). The license consists of your order details, the terms and conditions provided by Elsevier, and the payment terms and conditions.

Get the printable license.

License Number	3435061044996
License date	Jul 23, 2014
Order Content Publisher	Elsevier
Order Content Publication	Advances in Colloid and Interface Science
Order Content Title	Thermodynamic and kinetic aspects of fat crystallization
Order Content Author	C. Himawan,V.M. Starov,A.G.F. Stapley
Order Content Date	25 September 2006
Licensed content volume number	122
Licensed content issue number	1–3
Number of pages	31
Type of Use	reuse in a thesis/dissertation
Portion	figures/tables/illustrations
Number of figures/tables/illustrations	1
Format	both print and electronic
Are you the author of this Elsevier article?	No
Will you be translating?	No
Title of your thesis/dissertation	ESTIMATING AND MODELLING THE COMPOSITIONS OF CRYSTALLIZING TRIGLYCERIDE BINARY MIXTURES USING X-RAY DIFFRACTION
Expected completion date	Aug 2014
Estimated size (number of pages)	145
Elsevier VAT number	GB 494 6272 12
Price	0.00 USD
VAT/Local Sales Tax	0.00 USD / 0.00 GBP
Total	**0.00 USD**

◂ Back

License Details

This is a License Agreement between Dalhousie university ("You") and The Royal Society ("The Royal Society"). The license consists of your order details, the terms and conditions provided by The Royal Society, and the payment terms and conditions.

Get the printable license.

License Number	3435691327694
License date	Jul 24, 2014
Order Content Publisher	The Royal Society
Order Content Publication	Philosophical Transactions A
Order Content Title	The Growth of Crystals and the Equilibrium Structure of their Surfaces
Licensed copyright line	Copyright © 1951, The Royal Society
Order Content Author	W. K. Burton, N. Cabrera, F. C. Frank
Order Content Date	1951
Volume number	243
Issue number	866
Type of Use	Thesis/Dissertation
Requestor type	academic/educational
Format	print and electronic
Portion	figures/tables/images
Quantity	1
Will you be translating?	no
Circulation	10
Order reference number	None
Title of your thesis / dissertation	ESTIMATING AND MODELLING THE COMPOSITIONS OF CRYSTALLIZING TRIGLYCERIDE BINARY MIXTURES USING X-RAY DIFFRACTION
Expected completion date	Aug 2014
Estimated size (number of pages)	145
Billing Type	Credit Card
Credit card info	Master Card ending in 8234
Credit card expiration	12/2015
VAT (0.0%)	0.00 USD
Total	**4.20 USD**

Back